

©2019

YASIR DEMIRYUREK

ALL RIGHTS RESERVED

EFFECTS OF ELECTRIC FIELD ON CELLS AND
TISSUE: ELECTRODEFORMATION-RELAXATION AND
ELECTROPORATION MEDIATED DELIVERY

By

YASIR DEMIRYUREK

A dissertation submitted to the

School of Graduate Studies

Rutgers, The State University of New Jersey

In partial fulfillment of the requirements

For the degree of

Doctor of Philosophy

Graduate Program in Mechanical and Aerospace Engineering

Written under the direction of

Hao Lin

And approved by

New Brunswick, New Jersey

October, 2019

ABSTRACT OF THE DISSERTATION

Effects of Electric Field on Cells and Tissue: Electrodeformation-Relaxation and Electroporation-Mediated Delivery

By YASIR DEMIRYUREK

Dissertation Director:

Hao Lin

The main theme of this dissertation is to investigate the effects of electric field on biological cells and tissue. This highly multidisciplinary research involves the fields of electrohydrodynamics, cell mechanics, drug delivery, high-throughput signal/image processing, and design and development of medical devices. In the first part of this study, electrodeformation-relaxation is utilized to bring forth new insights to mechanical properties of biological cells. Electrodeformation is a contact-free and label-free method, and has high-throughput capability to simultaneously characterize a large cell population in a relatively short time. It is found that mechanical properties of cells display different characteristics depending on the pulse duration. Two distinctive regimes were discovered: in the first relaxation durations are proportional to pulsing duration, which corresponds to soft glass rheology

(SGR); in the second, they are independent, which is consistent with the worm-like-chain (WLC) regime. A quantification of the “naïve” cell mechanical properties is only possible in the latter. In the second and third parts of this dissertation, electroporation, a technique popular in the fields of drug/gene delivery, is studied both on the cellular and tissue levels. In Part 2, we conducted a series of two-pulse electroporation experiments at the cellular level, focusing on the delivery efficiency of two different-sized molecules using different pulsing parameters. We further systematically studied the effect of delay times between pulses on the delivery efficiency. Using an alternating-current (AC) first pulse to porate the membrane, and a direct-current (DC) second pulse for transport, we were able to probe resealing dynamics over timescales ranging from milliseconds to minutes. We found for these cells and pulsing parameters electroporation-mediated delivery scaled with the logarithm of the delay time regardless of the molecule size, and 50% of resealing happened in the first 100 ms after pulsation. However, complete resealing took hundreds of seconds. This result may unify the inconsistent membrane resealing times reported in the literature for different experiments. In Part 3, at the tissue level, we have developed an electroporation device to improve targeted transdermal gene transfection. The feasibility and mass production capability of electroporation chips have been demonstrated by upgrading and revising the design and assembly approach. These micro-electrode-based devices have been extensively tested on animals (rats) to demonstrate efficacies on gene expression.

Acknowledgements

I would like to begin thanking my advisor, Prof. Hao Lin. I am sincerely grateful that he continually and convincingly conveyed a spirit of adventure in regard to my Ph.D. journey. I would also like to express my deepest appreciation to my co-advisors and committee members, Dr. Jerry W. Shan, Dr. Liping Liu, Dr. David Shreiber, and Dr. Jeffrey Zahn for supporting and motivating my dissertation work. I would not be able to navigate in this research field without their guiding light and various perspectives.

I owe a debt of gratitude to all of those with whom I have had the pleasure to collaborate in both Mechanical and Biomedical Engineering departments at Rutgers University during this Ph.D. journey. My sincere thanks also goes to Dr. Miao Yu for being a great mentor of my research and, more importantly, being such a good friend. Lastly and undoubtedly, I specially thank Apcaoglu, Arturo Villegas Vaquero, Cevat & Burcu Akin, Muhammed Cosgun, and Semih & Eylul Cetindag for being excellent friends to me.

I am also grateful for conducting research in the field of cell mechanics. My connection to this field was upgraded to another level when I read the five main forces of the cell's functionality that was written in 1914 (Signs of Miraculousness). My deepest appreciation goes to the writer of that book.

Finally, I thank my family for being so supportive, encoring and always making me aware of their priceless love. I owe my deepest gratitude to my parents, Alaaddin and Nahide Demiryurek and my sister Arife, my brother-in-law Mehmet, and my beloved nephews Mete and Oguz Erturun.

Dedication

To my beloved nephews Mete and Oguz Erturun

Table of Contents

Abstract.....	ii
Acknowledgements	iv
Dedication	v
Table of Contents.....	vi
List of Tables	x
List of Figures	xi
Chapter 1	1
1.1. Preliminary formulation.....	1
1.2. Transmembrane potential w.r.t. electric field frequency.....	3
1.3. The scope of this dissertation	4
1.4. References.....	7
Chapter 2	8
2.1. Introduction.....	8
2.1.1. Background of Cell Mechanics.....	8
2.1.2. Electrodeformation (ED) and Relaxation Approach.....	14
2.1.3. Maxwell Stress Tensor	16
2.1.4. Electrodeformation in the literature	18
2.1.5. Statement of Objectives	23
2.2. Materials and Methods.....	25

2.2.1. Cell Culturing	25
2.2.2. Electrodeformation & Relaxation Experiment Setup.....	25
2.2.3. Cell Trapping and Stretching Protocol.....	26
2.2.4. Image Processing and Data Analysis	27
2.3. Results	30
2.3.1. Electric Field Strength Effect on Electrodeformation	30
2.3.2. Extracting Relaxation Timescales	31
2.3.3. Relaxation Timescales with Respect to Pulse Duration.....	33
2.4. Discussion.....	36
2.4.1. Electric Field Strength Effect on Electrodeformation	36
2.4.2. Relaxation Timescales	38
2.4.3. Two Distinctive Regimes	39
2.5. Conclusion	42
2.6. References.....	43
Chapter 3	47
3.1. Introduction.....	47
3.1.1. Mechanisms of Electroporation Mediated Molecular Delivery	48
3.1.2. Two-pulse Electroporation protocol.....	51
3.1.3. Statement of Objectives	53
3.2. Materials and Methods.....	55

3.2.1.	Cell Culture	55
3.2.2.	Electroporation Setup.....	56
3.2.3.	Electroporation Procedure	56
3.2.4.	Fluorescence Imaging Microscopy	58
3.2.5.	Image Processing and Data Analyzing.....	59
3.2.6.	Confirming and Calibration of the Fluorescence Imaging Method	60
3.3.	Results	63
3.3.1.	Single AC Pulse Application.....	63
3.3.2.	Single DC Pulse Application	64
3.3.3.	Two-Pulse Application with No Delay	65
3.3.4.	Two-Pulse Application with Variable Delay	68
3.4.	Discussion.....	72
3.5.	Conclusion	78
3.6.	References.....	80
Chapter 4	84
4.1.	Introduction.....	84
4.1.1.	Background of tissue electroporation.....	84
4.1.2.	Literature survey	86
4.1.3.	Statement of objectives.....	90
4.2.	Materials and Methods.....	91

4.2.1. Design of the 1 st and 2 nd Generation Chips.....	91
4.2.2. Mechanical characterization for insertion.....	97
4.2.3. Electrical characterization for pulse application	97
4.2.4. EP assays.....	99
4.3. Results	103
4.3.1. Mechanical characterization.....	103
4.3.2. Electrical characterization	103
4.3.3. EP results.....	105
4.4. Discussion.....	112
4.5. Conclusion.....	116
4.6. References.....	117
Chapter 5	121

List of Tables

Table 2-1 The ED experiment setup provides sufficient forcing to deform cells with high electric field strength while avoiding electrolysis and membrane breakdown with high-frequency pulses. Pulsing parameters are listed here.	28
Table 2-2. Listed the medians of the long and short relaxation timescales for the MDA-MB-231 cells before the transition point in which timescales were no longer proportional with pulsing duration (tp).....	34
Table 2-3. Listed transition times (tc) for long and short relaxation timescales (tc, long and tc, short). Transition points for the short relaxation timescales fluctuate due to the scatteredness of the data, whereas the transition points for the long relaxation timescales are around ~50 ms.	35
Table 3-1 Applied pulse parameters for the first and second pulse	58
Table 4-1 The list of commercially available EP devices that utilize penetrating electrodes for either transdermal or intramuscular application. Most of the devices are in the clinical trials. Electrode designs in terms of size, number, the gap between them, pulse designs in terms of amplitude, duration, intervals, and numbers, and delivery vector are listed under the device design section along with a representative picture. Exemplary results and brief conclusions are listed in the result section along with the selected figures.....	87
Table 4-2 Comparison between 1 st and 2 nd gen. EP chip designs.....	96

List of Figures

Figure 1.1 (a) A schematic representation of a cell under an electric field with interior (<i>i</i>) and exterior (<i>e</i>) fluids, <i>m</i> denotes the membrane. (b) An RC circuit analogy for electrical current transport.	2
Figure 1.2 The RMS transmembrane potential, V_m , is plotted versus frequency ω . The parameters used for the curve is given in the inset. At high frequencies, V_m is very low. At low frequencies, the V_m approaches that from a DC field application. The “sweet spot” (explained in Section 1.3) is to separate clearly the effects of electro-permeabilization and delivery. Electroporation typically occurs when V_m is above 0.5 V.	4
Figure 2.1 Standard viscoelastic models commonly used to represent soft tissues (a) Maxwell (b) Kelvin-Voigt (or Voigt) (c) Zener standard linear solid (or Kelvin) ²²	9
Figure 2.2 Schematic representation of the major techniques used for identifying mechanical properties of cells, (a)-(c) and (g) are subcellular probing methods, (d)-(f) and (i) are single-cell level mechanical characterization, and (h) is used to infer the cytoadherence, deformation and mobility characteristics of populations of cells ^{1,23}	11
Figure 2.3 (a) A schematic presentation of electrodeformation (ED) in the presence of a DC electric field E_0 ; the dashed circle is the original shape, the solid line is the elongated shape, and, depending on the dielectric properties, it deforms into a prolate or oblate shape ⁵¹ . A silicon oil drop, exposed to an external DC electric field, shows the ED and flow pattern both inside and outside of the drop (Taylor’s classic study was published in 1966 ⁵⁰).	15
Figure 2.4 (a) Schematic of ED-relaxation (ED-R) experiment setup. High frequency and amplitude electric pulses were applied to the cell suspension. Cell deformation and relaxation were recorded with a synchronized high-speed camera. (b) A photograph of actual ED-R chip.	

(c) An exemplary image of a trapped cell on the ED-R chip the horizontal black line is the edge of the ITO electrodes and the red and green lines around the cell are the edge detection points of the cell and the ellipsoidal fitting, respectively.....26

Figure 2.5 Nearly 2,000 frames for each case were analyzed using a custom-made code in MATLAB. (a) shows the intermediate steps of cell membrane detection a hollow region of interest (in the left image colored in blue) is defined to speed-up the processing then, the cell membrane is spotted using a gradient-based edge-detection method (the red points in the middle image) finally, an ellipse shape is best-fitted (dashed green line in the right image). The shape factor (ϵ) is defined as the ratio of the long and short axes. In (b), an exemplary image sequence demonstrates the electrodeformation-relaxation process, and the shape factor change is plotted with respect to time. It is noted that the movement of the cell on the electrode does not affect the image processing29

Figure 2.6 (a) Shape factor changes of four different MDA-MB cells under consecutively increasing pulsing; each pulse was 0.5 s long at 7 MHz, and the relaxation recorded was almost 1 s long, but only the first 0.5 s of the relaxation potted. (b) The maximum deformation achieved at the end of the pulse is plotted against the square of the applied voltage.....31

Figure 2.7 An exemplary plot that shows the procedure of extracting relaxation timescales from the data. (a) The shape factor changes in a semilog-y plot. (b) Single and double exponential best-fitting curves for the data points, double exponential fitting more accurately captures the decay.32

Figure 2.8 The relaxation timescales for the MDA-MB-231 cells with respect to pulsing duration are plotted. Each point is presented with a box and whisker plot, in which the box is within the 25th and 75th percentile, and the median value is marked with a circle.34

Figure 2.9 The relaxation timescales for the MCF-7, MCF-10A, and GBM cells with respect to pulsing duration are plotted. Each point is presented with a box and whisker plot, in which the box is within the 25 th and 75 th percentiles, and the median value is marked with a circle.	35
Figure 3.1 Schematic of (a) the experimental setup and (b) AC first (FP) and DC second (SP) pulses applied to the cells with a specified delay.	56
Figure 3.2 A schematic of working principle of fluorescence imaging. A high-intensity UV light which is provided by a mercury lamp, is filtered by triple band pass (DAPI - FITC - TRITC) filter and images are acquired by a high-sensitivity camera.	59
Figure 3.3 Examples of (a) cell images taken for image processing (the contrast of these images has been adjusted for display purposes only), and (b) scatter plot showing FD and 7-AAD intensities per volume in a representative set of analyzed images.....	60
Figure 3.4 Calibration experiment, (a) the schematic of placing different-diluted FD solutions. The gap between cover slips is fixed by using double-sided adhesive tape. (b) The fluorescence intensity versus concentration for FD 10k and FD 70k conjugates.	62
Figure 3.5 Intracellular 10 kDa concentrations and viability for different-frequency AC fields (1 ms, 0.9 kV/cm) compared to a DC field of the same strength.	64
Figure 3.6 Delivered intracellular concentration for a single 30-ms-long DC pulse of different field strengths.....	65
Figure 3.7 Delivered intra-cellular FD concentrations and viability for different AC FP strengths and molecule sizes: (a) 10 kDa FD and (b) 70 kDa FD.	66
Figure 3.8 Delivered intra-cellular FD concentrations with different delay times ranging from 1 ms to 300 s for different AC FP strengths and molecule sizes: (a) 10 kDa FD and (b) 70 kDa FD.....	71

Figure 4.1 A schematic of the skin layers. The SC layer is not shown for simplicity. The epidermis layer has a higher cell density than the dermis layer.	85
Figure 4.2 1 st generation EP chip PCB design. It has 10x10 needle holders and 4 units 25-pin connector location. (a) 3D model designed in SolidWorks. (b) The PCB layout design with traces built with PCBArtist software. (c) A picture of 1 st gen. EP chip fabricated by Advanced Circuits, Aurora, CO.....	92
Figure 4.3 Printed circuit board (PCB) layer structure. Two-conductive-layer PCB was designed for the 1 st generation EP chip (Top Copper and Bottom Copper). The PCB board was drilled with through-holes with 300 μ m diameter for needle housing, and the through-holes were plated with copper to provide an electrical connection. The center-to-center distance between holes was designed to be 1.3 mm.	92
Figure 4.4 2 nd generation EP chip PCB design. It has 4x4 needle holders (200 μ m diameter) spaced 0.75 mm apart and 1-unit 4-pin connector (HRS, DF58-4P, 5x5 mm in size) location. (a) The 3D model designed in SolidWorks. (b) The PCB layout design with traces built with PCBArtist software. It has 4 conductive layers and 3 via holes that connect the bottom layers to the top layer of the connector. (c) A picture of 2 nd gen. EP chip fabricated by Advanced Circuits, Aurora, CO.....	93
Figure 4.5 Stainless steel acupuncture needles were used for the EP chip. (top) In the 1 st gen., 300 μ m diameter acupuncture needle tapers to a fine point over a 1.5 mm tip length at a 5.7° taper angle, (bottom) in the 2 nd gen. 160 μ m diameter acupuncture needle tapers to a fine point over a 745 μ m tip length at a 6.129° taper angle were attached to the EP chip.	93
Figure 4.6 Needle assembly procedure of the 1 st gen. EP chip. Electrode holders are filled with solder and, while the solder is still warm and fluid, the needles get inserted. After the	

solder solidifies, the back of the needle is clipped and more solder is added for a greater electrical connection and mechanical strength.....	94
Figure 4.7 1 st gen. EP Chip with needles attached by soldering. Initially, 3x3 needle array is used. The sharpness of the needles is low due to the assembly procedure, and a small amount of solder has flowed towards the application's skin-facing side.....	95
Figure 4.8 2 nd gen. EP chip assembly procedure. The pre-cut needles are attached to the PCB by using a light-curable polymer. The tips of the needles are covered entirely. Then, the chip is dipped into the solder bath for a few seconds.	96
Figure 4.9 (left) 2 nd gen. EP chip pictures with the needles attached. (right) The space between the needles and their protruding length are shown schematically.....	96
Figure 4.10 The implementation of the 1st gen. chip to mechanically determine the needle insertion to porcine skin. a) A side view of a skin sample that shows the needle traces. b) The skin samples were sectioned by using a cryotome in 50 μm thickness.	97
Figure 4.11 Schematic of the experiment's setup, including a function generator, amplifier, potentiostat, and an EP chip.	98
Figure 4.12 The electric field distribution was probed by using a potentiostat. (a) An exemplary picture of electrical characterization with conductive fluid. Arrays of six needles in line, equally distanced by 1.3 mm, were used. The insertion depth was between 0.5 and 2 mm. (b) The probing and running electrodes configuration is shown in a diagram. Typically, the running electrodes (blue dots) that deliver the pulse were on the outer edge, and the probing electrodes were in the middle rows, as indicated above with green dots.....	98
Figure 4.13 A schematic of the fresh porcine skin EP procedure. The skin tissue is depilated first, followed by injection and pulsation. The skin samples are kept in the incubator for some time, then sectioned and imaged under an epifluorescent microscope.....	100

Figure 4.14 (a) A picture of a MicronJet600 microneedle, the insert is the magnified view of the injector blade made of pure silicon crystal. (b) An exemplary picture of a test-rat, four sites were injected and marked. The rat was kept anesthetized by isoflurane inhalation through the nose cap and rested on a warm blanket. 101

Figure 4.15 A side view of a skin sample that shows the needle traces. (a) 1st gen. chip with 2 mm needle length was implemented, with the average penetration around 1 mm. (2) 2nd gen. chip with 1mm needle length was implemented, the average penetration was approximately 0.7 mm. 104

Figure 4.16 The voltage drop across the running electrodes was mapped in a standard salt solution (conductivity of 84 $\mu\text{S}/\text{cm}$) with (a) 1x6 electrode array, (b) 3x3 electrode array. The black line represents a COMSOL simulation result that was prepared by Yu, the blue lines are the measurements. (c) Electrical characterization was performed with porcine skin, the penetration depth was around 1 mm, and a 1x5 needle array was used. 105

Figure 4.17 An exemplary side view of merged (both in bright field and in TRITC channel) image of the sliced skin section with PI delivery. 15 Vpp, 10 kHz, 1 ms long AC pulse applied between needle 2 and 3. The image was taken 20 mins post-pulsation. The needle length is 1 mm. The blue dash lines show the needle insertion site, the penetration depth is approximately 0.7 mm long. The red color represents the PI delivery. 107

Figure 4.18 The PI delivery distribution in the skin tissue over time is presented with a box plot for each layer of the skin. The side view images of the skin section were analyzed with a custom MATLAB code. The PI signal intensity averaged over the area of each layer. Ignoring the outmost SC layer, the epidermis, dermis, and hypodermis layers were identified with a bright-field image. All samples were injected with 0.1 ml of 40 $\mu\text{g}/\text{ml}$ Propidium Iodide with MicronJet 600 microinjector, approximately 0.3 to 0.7 mm deep into the tissue. In the control

samples, needles were inserted but not pulsed, in the pulsed samples 15 V_{pp}, 10 kHz, 1 ms long AC pulse applied..... 108

Figure 4.19 The percentage of the skin impedance changes (real part only) are shown. The potentiostat (GAMRY Reference 600+) and 1x4 arrayed EP chips were employed, and impedance was measured at 3 kHz sensing frequency by using a 4-point probe method. The measurement points were randomly selected, and successive measurements were performed for the same point. Between the measurements 3 and 4, a 1 ms EP pulse was applied (the solid black line) with different field strengths. 109

Figure 4.20 GFP expression in the rat skin is presented. 25 µg pEGFP vector in 50 µl PBS solution was injected, 15 V, 100 µs long 4 pulses at 1 Hz were applied. The tissue was imaged using (a) FITC, (b) TRITC and (c) DAPI filters to assess the autofluorescence which can be seen due to the hair follicles. A merged image is presented in (d). The GFP expression is localized around the needle insertion sites at the corners of the square in (a) corresponding to the needle placement consistent with the EP chip dimensions (1 mm long, 750 µm apart). 111

Figure 4.21 GFP expression in the rat skin concerning different pulsing conditions. All images presented merged channels of FITC (green), TRITC (red), and DAPI (blue). 25 µg pEGFP vector in 50 µl PBS solution is injected with MicronJet 600 microinjector, and (a) control sample, (b) 15 V, 100 µs long 4 pulses at 1 Hz, (c) 30 V, 100 µs long 4 pulses at 1 Hz were applied. In the control case, the needles were inserted but not pulsed. 111

Chapter 1

Introduction

Electrohydrodynamics (EHD) is a multi-physical flow phenomenon that studies the dynamics of fluid interactions with electric fields¹. In modern developments, it frequently involves very small scales ranging from μm to nm . Systems based on EHD principles often offer many advantages for flow control and actuation that would be difficult with other mechanisms, such as “slip flow” by utilizing electroosmosis². EHD also finds relevance in the interaction of biological cells with electric fields, as such interactions often involve both the mechanical and transport aspects of this general class of phenomenon. It is the focus of this dissertation to study such aspects, within the applied contexts of cell mechanics and electric-field-mediated molecular delivery. Two main problems are tackled. In the first, we examine how an electric field can be used to deform cells and hence offer a means to analyze the mechanical properties. In the second, we use electric fields to transport molecules, small and large (such as DNA) inclusive, on both single-cell and tissue levels. In what follows, we first review some basic equations and formulations pertinent to our study. We then outline the scope of this dissertation.

1.1. Preliminary formulation

All biological cells have membranes that encapsulate the interior fluid and organelles. The membrane is formed by a lipid bilayer with a thickness of around 5 nm and plays a crucial role in cell function. Figure 1.1a shows a schematic of a biological cell under an applied electric field, in which the interior organelles are ignored. The membrane is an infinitesimally thin layer separating fluids with different physical and electrical properties, e.g. conductivity and

permittivity $(\sigma_i, \sigma_e, \varepsilon_i, \varepsilon_e)$. Assuming bulk electroneutrality, the electric potential, Φ , in the bulk fluids is governed by the Laplace equation

$$\nabla^2 \Phi = 0, \quad \mathbf{E} = -\nabla \Phi. \quad (1.1)$$

The transmembrane potential, V_m , can be defined as

$$\Phi_i - \Phi_e = V_m. \quad (1.2)$$

Hence, the conservation of the current at the membrane can be written, as

$$\underbrace{\vec{n} \cdot (\sigma_i \nabla \Phi_i)}_{\text{Ohmic Current}} + \underbrace{\vec{n} \cdot (\varepsilon_i \frac{\partial \nabla \Phi_i}{\partial t})}_{\text{Displacement Current}} = \underbrace{\vec{n} \cdot (\sigma_m \nabla \Phi_m + C_m \frac{\partial V_m}{\partial t})}_{\substack{\text{When membrane not} \\ \text{permeabilized}}} = \underbrace{\vec{n} \cdot (\sigma_e \nabla \Phi_e + \varepsilon_e \frac{\partial \nabla \Phi_e}{\partial t})}_{\text{Displacement Current}}. \quad (1.3)$$

fast relaxation $\sigma_m \approx 0$

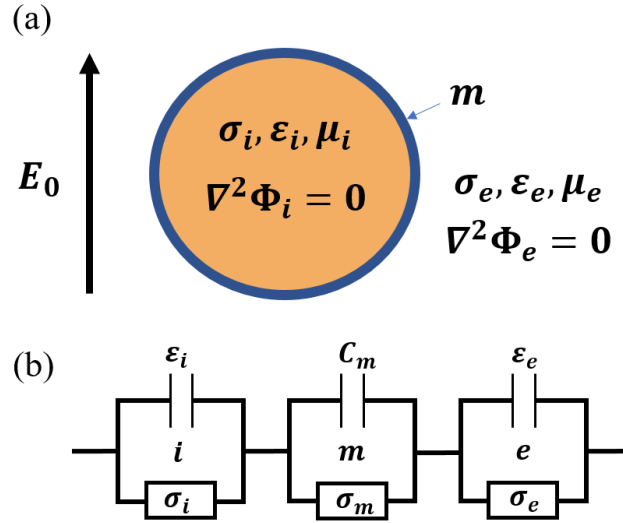


Figure 1.1 (a) A schematic representation of a cell under an electric field with interior (*i*) and exterior (*e*) fluids, *m* denotes the membrane. (b) An RC circuit analogy for electrical current transport.

An RC circuit analogy (Figure 1.1b) can be employed to represent charging dynamics.

The resistors accommodate the ohmic current and the capacitors, displacement current. The timescale for the relaxation of the displaced free ions is

$$t_{relax,k} = \frac{\varepsilon_k}{\sigma_k}, \quad k = i, e. \quad (1.4)$$

In this case, the charge relaxation time scale is on the order of a few nanoseconds or less, $t_{relax,k} \approx O(ns)$, thus the displacement current in the bulk can be in general omitted for simplicity. Further, the membrane has very low conductivity if it is not permeabilized, so that Ohmic current can be removed for the membrane in Eq 1.3, which, after simplification, becomes

$$\vec{n} \cdot \sigma_i \nabla \Phi_i = \vec{n} \cdot C_m \frac{\partial V_m}{\partial t} = \vec{n} \cdot \sigma_e \nabla \Phi_e. \quad (1.5)$$

1.2. Transmembrane potential w.r.t. electric field frequency

Applying appropriate boundary conditions and seeking a solution with separation of variables yields

$$V_m = \frac{3}{2} E_0 R \left(1 - e^{-t/\tau_r} \right) \cos \theta \quad (1.6)$$

where E_0 is applied DC electric field, R is the cell radius, typically $\sim 10 - 15 \mu m$, and the capacitive charging time scale, τ_r , is

$$\tau_r = RC_m \left(\frac{1}{\sigma_i} + \frac{1}{2\sigma_e} \right). \quad (1.7)$$

In the case of the AC field application, $E = E_0 e^{j\omega t}$ where ω is the frequency and $j = \sqrt{-1}$, then the transmembrane potential is in a solution form

$$V_m = \frac{3}{2} E_0 R \frac{1}{1+j\omega\tau_r} \left(e^{j\omega t} - e^{-t/\tau_r} \right) \cos \theta. \quad (1.8)$$

A plot of the RMS transmembrane potential with respect to applied field frequency is shown in Figure 1.2. It can be clearly seen that the V_m decays drastically in the high frequencies. The

threshold for an electrical breakdown of the membrane is estimated to be around 0.5 V or higher⁴. Therefore, by adjusting the applied electric field parameters, electro-permeabilization of the cells can be controlled.

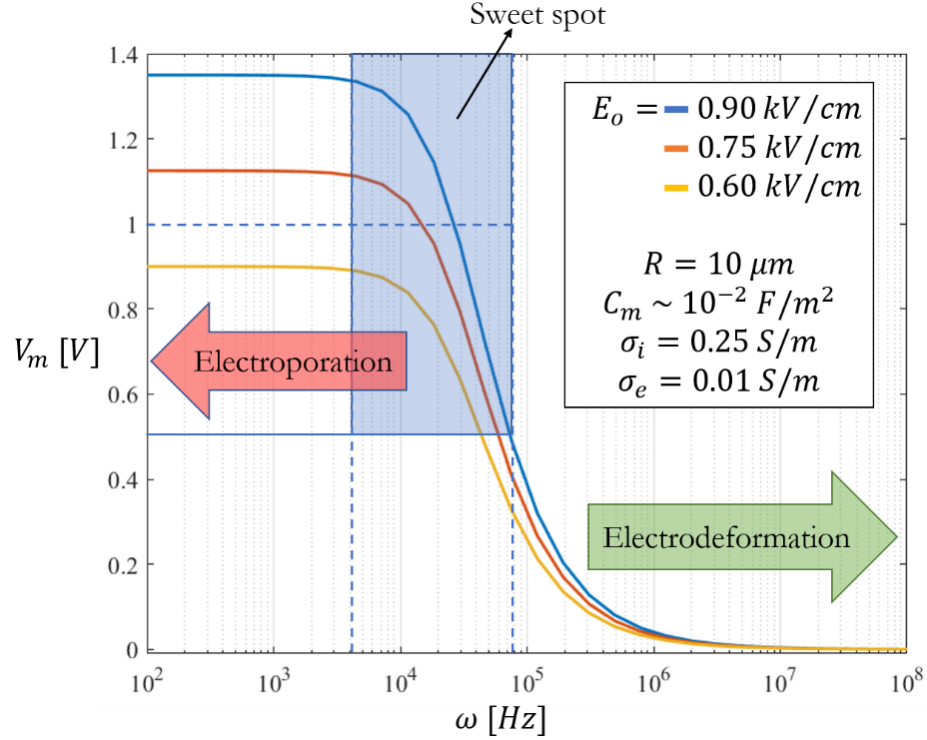


Figure 1.2 The RMS transmembrane potential, V_m , is plotted versus frequency ω . The parameters used for the curve is given in the inset. At high frequencies, V_m is very low. At low frequencies, the V_m approaches that from a DC field application. The “sweet spot” (explained in Section 1.3) is to separate clearly the effects of electro-permeabilization and delivery. Electroporation typically occurs when V_m is above 0.5 V.

1.3. The scope of this dissertation

In Figure 1.2, three regions can be identified: (1) the high-frequency region ($\omega \geq 10^6$ Hz) where the V_m is nearly zero, (2) the “sweet spot” (explained in Section 1.3) where the V_m is higher than 0.5 V and $\omega > 10^3$ Hz, and (3) the electroporation region where V_m is higher than 0.5 V. In this thesis we examine the different physical phenomena occurring in these three regions.

In the first, we utilized the electric field as a tool to deform the cells. Similar to the fundamental concept of stress-strain relation, we attempt to quantify the response of the cells to external forcing. It is well-known that cells react or generate mechanical forces to sustain their functionalities by adjusting their biological, chemical and physical properties⁵⁻⁷, and that their mechanical properties can be used as pathological indicators. Due to its importance, a variety of techniques have been developed in the past two decades to extract these properties⁸, including atomic force microscopy (AFM)^{9,10}, micropipette aspiration¹¹, optical and magnetic tweezers^{12,13}, micropipette aspiration¹¹, among many others. Despite that significant developments have been achieved, there are certain limitations depending on the method and overly-simplified models to interpret the outcome. To overcome the limitations, this study is aimed to design and develop a platform that extracts mechanical properties of cells in a feasible and robust way. As seen in Figure 1.2, V_m can be maintained below the electroporation threshold at high frequencies, hence the external electric field can be leveraged to deform to the cell depending on the strength of the field in the absence of electroporation (that compromises membrane integrity). In Ch. 2, detailed theoretical and experimental explanations are provided.

In the second, we aimed to better-understand two main mechanisms of the electroporation-mediated delivery, which are electro-permeabilization and electro-transport of the exogenous molecules. Our group previously used a two-pulse scheme with a high-voltage (HV) first pulse and followed by a low-voltage (LV) second pulse, where the first HV permeabilizes the cells and the second LV provides electrophoretic drag to uptake the molecules¹⁴. However, the first HV DC pulse itself may cause significant delivery. In addition, the effect of the (controlled) delay between the pulses was not studied systematically. To clearly separate these mechanisms an AC first pulse is employed and the delay between the pulses is

varied in a wide range. The electrical parameters of the first pulse are chosen from the “sweet spot” region where V_m is above 0.5 V and the frequency is above 3 kHz. The sufficient V_m ensures the electro-permeabilization, whereas the oscillating field in general cancels the electrophoretic transport effects due to the rapid reversal of electric field polarity. Hence this region is called a “sweet spot” that provides permeabilization with minimal delivery. In theory, once the cell membrane is permeabilized, re-poration threshold would be lower than the intact cell. Thus, we hypothesized that knowing the lifetime of the electro-pores and the second voltage threshold for re-poration can further increase the transfection efficiency. As a result, we have quantified the lower voltage requirement for the re-poration pulse and found an inversely linear correlation between transfection efficiency and logarithm of delay time between pulses. Our results and findings are presented in Ch. 3 and published in archived journal paper¹⁵.

In the third and based on the fundamental knowledge we gained on the single-cell studies above, we engineered a miniaturized device to achieve the goal of transdermal delivery with high efficiency and viability. A printed circuit board (PCB) based, minimal invasive transdermal gene transfection device is designed and prototyped. Since electroporation is desired, pulsing parameters were chosen low-frequency region. It is also noted that Figure 1.2 is plotted for single cells. At the tissue level, V_m is quite different and not uniform. Therefore, a computational study was performed by Dr. Miao Yu, and results were used to help to choose proper pulsing parameters. The development of the electroporation chip and preliminary testing results are presented in Ch. 4.

Overall, the first and second are fundamental studies in nature, the third embodies a translational effort toward building a clinically useful vehicle for efficient drug or gene delivery.

1.4. References

1. Saville, D. A. ELECTROHYDRODYNAMICS: The Taylor-Melcher Leaky Dielectric Model. *Annual Review of Fluid Mechanics* **29**, 27–64 (1997).
2. Dutta, P. & Beskok, A. Analytical Solution of Time Periodic Electroosmotic Flows: Analogies to Stokes' Second Problem. *Anal. Chem.* **73**, 5097–5102 (2001).
3. Li, J. & Lin, H. The current-voltage relation for electropores with conductivity gradients. *Biomechanics* **4**, (2010).
4. Krassowska, W. & Filev, P. D. Modeling Electroporation in a Single Cell. *Biophysical Journal* **92**, 404–417 (2007).
5. Unal, M. *et al.* Micro and Nano-Scale Technologies for Cell Mechanics, Micro and Nano-Scale Technologies for Cell Mechanics. *Nanobiomedicine* **1**, 5 (2014).
6. Gurkan, U. A. & Akkus, O. The mechanical environment of bone marrow: a review. *Ann Biomed Eng* **36**, 1978–1991 (2008).
7. Sun, Y. *et al.* Mechanics Regulates Fate Decisions of Human Embryonic Stem Cells. *PLOS ONE* **7**, e37178 (2012).
8. Suresh, S. Biomechanics and biophysics of cancer cells. *Acta Materialia* **55**, 3989–4014 (2007).
9. Hessler, J. A. *et al.* Atomic Force Microscopy Study of Early Morphological Changes during Apoptosis. *Langmuir* **21**, 9280–9286 (2005).
10. Li, Q. S., Lee, G. Y. H., Ong, C. N. & Lim, C. T. AFM indentation study of breast cancer cells. *Biochemical and Biophysical Research Communications* **374**, 609–613 (2008).
11. Hochmuth, R. M. Micropipette aspiration of living cells. *Journal of Biomechanics* **33**, 15–22 (2000).
12. Dao, M., Lim, C. T. & Suresh, S. Mechanics of the human red blood cell deformed by optical tweezers [Journal of the Mechanics and Physics of Solids, 51 (2003) 2259–2280]. *Journal of Mechanics Physics of Solids* **53**, 493–494 (2005).
13. Fabry, B. *et al.* Selected Contribution: Time course and heterogeneity of contractile responses in cultured human airway smooth muscle cells. *Journal of Applied Physiology* **91**, 986–994 (2001).
14. Sadik, M. M. *et al.* Scaling relationship and optimization of double-pulse electroporation. *Biophys J* **106**, 801–812 (2014).
15. Demiryurek, Y. *et al.* Transport, resealing, and re-poration dynamics of two-pulse electroporation-mediated molecular delivery. *Biochimica et Biophysica Acta (BBA) - Biomembranes* **1848**, 1706–1714 (2015).

Chapter 2

SINGLE CELL MECHANICS VIA ELECTRODEFORMATION AND RELAXATION

2.1. Introduction

2.1.1. Background of Cell Mechanics

Cells react or generate mechanical forces by adjusting their biological, chemical or physical properties¹⁻³. Depending on the mechanical properties of the cells, these forces change the shape of the cell or generate fluidic motion within the cell. Studies highlighted the role of the cell's mechanical properties on cell adhesion, migration, polarization, and differentiation, as well as organelle organization and trafficking inside the cytoplasm⁴. In particular, the variation of mechanical properties between normal and abnormal cells indicates the pathological status of the cell. For instance, deformability, a key mechanical property, defines the softness or stiffness of the cell. Any alteration in deformability might be a cause or result of a disease such as asthma, malaria, or cancer, among many others⁶⁻⁸. Another example occurs at the tissue level; when smooth muscle cells lose their deformability, the compliance of blood vessels is altered, which can cause hypertension or other cardiovascular diseases⁹. Cell mechanics have increasingly become a vital factor of the diagnostic field which researchers have continued to extensively explore using diverse experimental techniques and theoretical models.

It is widely viewed that cells are considered “soft matter” that exhibit elastic and viscous properties (attributed as “viscoelastic”). Viscoelastic materials can store and dissipate mechanical energy over time depending on their mechanical properties. For example, when a

soft rubber ball and a stiff rubber ball are squeezed to deform same amount and then relaxed to recover, the stiff ball recovers its shape faster than the soft ball, hence, the duration of recovery is a function of mechanical properties of the rubber balls. The most well-known viscoelastic material models are the Maxwell and Kelvin-Voigt models, which are composed of either series- or parallel-connected springs and dampers, as shown in Figure 2.1. Particularly, in polymer science, these models are in good agreement with experimental studies that aims to analyze the mechanical properties of polymers.

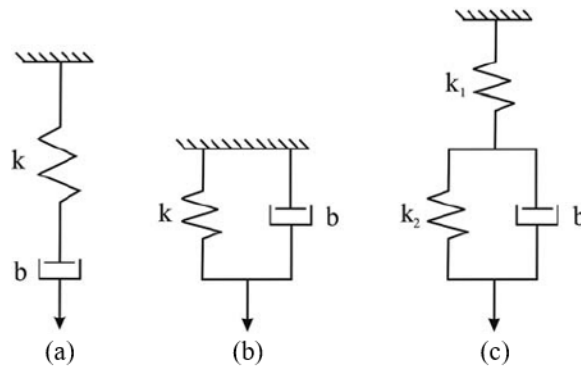


Figure 2.1 Standard viscoelastic models commonly used to represent soft tissues (a) Maxwell (b) Kelvin-Voigt (or Voigt) (c) Zener standard linear solid (or Kelvin)²².

However, unsurprisingly, in the case of cell mechanics, these models fail because of the complexity of the cellular structures. This complexity arises from many sources. For example, the cytoskeleton, which is composed of various filaments, such as microfilaments, microtubules, and intermediate filaments¹⁶, which have different structure and thereby different mechanical properties. In addition, the cytoskeleton is not a fixed structure, it constantly remodels its structure by polymerizing or depolymerizing its filament network^{10,18–20}. Therefore, identifying the mechanical properties of the cells is not easy task. Consequently,

the reported mechanical properties are scattered even in the same cell type varying from each other up to 1,000-fold^{4,21}.

Typically, researchers investigate cell mechanics using comparative characterization. For example, studies on cancer and healthy cells using the same approach found that cancer cells are softer than healthy cells by up to 70%^{13–15}. Up to date, a variety of techniques have been developed (shown in Figure 2.2) to measure cell deformability²³, including atomic force microscopy (AFM)^{24,25}, micropipette aspiration²⁶, and optical and magnetic tweezers^{27,28}, among many others. In the following section, the most common techniques, as well as their capabilities and limitations are summarized.

Atomic force microscopy (AFM) is a high-resolution surface characterization technique used at the subcellular level. Owing to its high-resolution and sensitivity capability, it has become the most common technique in cell mechanics in the last two decades^{5,29–31}. In the AFM technique, a functionalized probe (usually a sharp tip) that is attached to the free end of a cantilever physically makes contacts with the surface of the cell and then travels onto an adherent cell or tissue surface at a defined speed. A 3D piezo scanner then identifies the displacement of the cantilever. Since the material properties of the cantilever beam are known, the forces arising from any deformation are calibrated with mechanical properties of the cell. AFM is capable of measuring subnanometer displacement and pico-newton forces¹⁰. Although AFM is a well-established measurement technique and commercial systems are readily available, the resulting measurements might differ more than ten-fold from one report to other, depending on the probed region of the cell or the measurement parameters⁴.

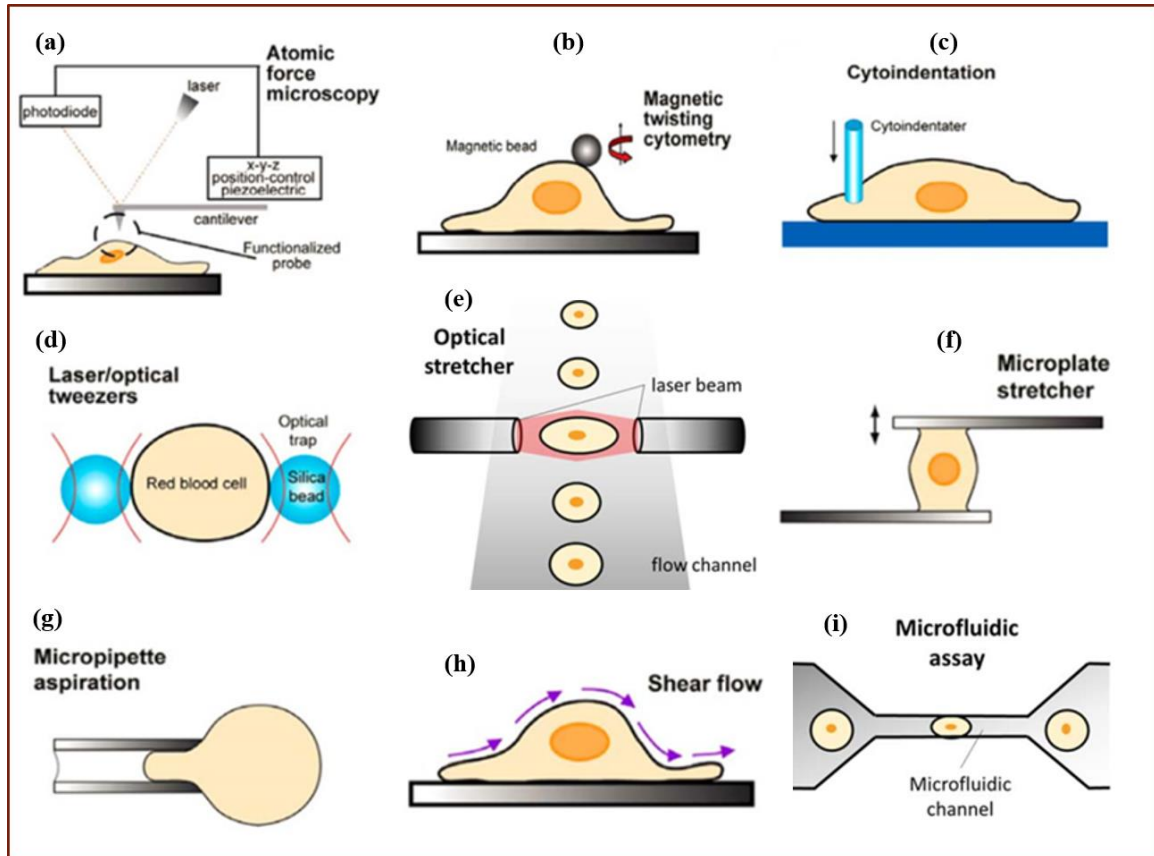


Figure 2.2 Schematic representation of the major techniques used for identifying mechanical properties of cells, (a)-(c) and (g) are subcellular probing methods, (d)-(f) and (i) are single-cell level mechanical characterization, and (h) is used to infer the cytoadherence, deformation and mobility characteristics of populations of cells^{1,23}.

Magnetic twisting cytometry (MTC) is also a subcellular mechanical characterization technique that applies local stresses to cells with magnetic beads. Magnetic beads that are controlled by magnetic field generate deformation on the cell surface. Shape change of the cells is recorded optically³². MTC is capable of employing a wide range of forcing frequency (0-1,000 Hz) and probing more than 100 cells simultaneously^{32,33}, however, the maximum stress application of MTC is limited to up to 140 Pa^{21,34}. Additionally, it requires pre-labeling of the cell membrane with some type of antibody that establishes the attachment of the magnetic beads on the cell membrane.

The laser/optical tweezer (LOT) technique has been used at the cellular and tissue level^{35–37}. LOT utilizes highly focused laser beams to generate an attractive or repulsive force on the order of pico-newton. Either scattering (caused by photons striking along the propagation direction) or gradient (generated by the gradient of the field intensity) forces are held or driven like “tweezer”³⁸. Similar to MTC, this is not a label-free method. The beads are coated with certain antibodies, extracellular matrix proteins, and lectins, to help beads attach to the cell membrane. Once the beads are linked to the cell membrane, the cells are then deformed by the manipulation of the beads^{39,40}, however, reaching an equilibrium position in which the optical force is zero is a tedious-task in the experiment conditions³⁵. Additionally, there is evidence that localized heating occurs due to the highly intensive laser light⁴¹. Lastly, the frequency modulation of the force application is not possible in that it does not allow for the investigation of mechanical properties in short timescales⁴².

The micropipette aspiration is also measurement technique at the single-cell level. As indicated by its name, a portion of the cell membrane is aspired using a micropipette tip with a controlled suction pressure⁴³. The deformation of the cell membrane with respect to suction force is correlated with the elasticity of the membrane. It is used in various application listed in Rodriguez *et al.*⁴⁴ and even in mouse embryos⁴⁵. It is a low-cost technique, whereas its accuracy depends on the optical imaging limitations²⁶. A novel technique called microelastography, reported in Grasland-Mongrain *et al.*⁴⁶, employs a micropipette to keep the cell stationary and applies high-frequency (15 kHz) shear elastic waves. It also analyzes the shear elastic modulus using seismology methods. Micropipette aspiration method suffers from low throughput and requires skilled operators. Thus, new developments that combine micropipette aspiration with microfluidic devices could improve the speed of data collection, and, thus, statistically meaningful data could be obtained⁴³. On the other hand, cells are

subjected to a suction pressure of up to 70 Pa for a long duration of ~ 10 s until they reach stable point, which does not allow for probing mechanical properties in short timescales⁴⁵.

Microfluidic assays, or MEMS and BioMEMS have been rapidly emerging in the cell mechanics field due to their low cost, easy adaptation, and high-throughput capabilities¹. A diverse microfluidic assay application can be found in literature^{23,44}. In general, this assay aims to mimic human body conditions in which cells are exposed to either a continuous or pulsatile flow. Furthermore, various fluid flow profiles could be applied to cell population to identify cell stiffness, deformability, and topology¹. By coating the channel walls with different adhesion proteins and arranging the width of the channel cell adhesiveness and contractility can be investigated as well⁴⁷. Overall, microfluidic systems are promising in terms of identifying mechanical properties of the cell and may be employed in combination with other techniques; for example in this study, the electrodeformation and relaxation method was combined with microfluidics technology.

Although significant improvements have been achieved in the cell mechanics field and the cell mechanics have been explored from various perspectives, there are certain limitations such as:

- incapability to differentiate between the structural root causes of deformability alterations,
- overlooking the dilatational changes in the multiphase materials of the cytoplasm^{48,49},
- insufficient temporal resolution of the measurements,
- oversimplified models, and

- a wide range of scattering of the mechanical properties even for the same cell type⁴.

The present study employs the electrodeformation and relaxation technique, and its aim is to highlight the unique capabilities of electrodeformation.

2.1.2. Electrodeformation (ED) and Relaxation Approach

In the presence of an electric field, charges accumulate at the interface that separates two dielectrically heterogeneous medium shown in Figure 2.3a (i. e., the Maxwell-Wagner effect). This polarization generates electrical stresses resulting in the deformation of the elastic membrane. Figure 2.3b shows the deformation oil drop under a DC electric field with both surrounding and internal fluid flow patterns (Taylor's classical work)⁵⁰. The key electrical properties involved are conductivities (σ_i, σ_e , internal and external conductivity respectively), relative permittivities (ϵ_i, ϵ_e , internal and external permittivity respectively), and fluidic property viscosities (μ_i, μ_e , internal and external viscosity respectively), and the electrical stresses and responsive fluid motion are estimated using these properties. This phenomenon is a well-defined problem for droplets under electric field and transient analytical solution is available⁵¹. Considering bilipid membrane as an interface introduces new forces arising from the elastic properties of the lipid membrane. Fortunately, the solution is also available in literature⁵² and reveals the mechanical properties of the membrane. There are quantitative experimental studies that have used giant vesicles (cell-mimic) that are in-line with this theory⁵³⁻⁵⁶. On the other hand, applying an electric field to suspended cells has been debatable due to the complexity of the cell cytoplasm and diverse protein content of the membrane. The first study that used the ED method for cells was performed by Engelhardt *et al.* and used erythrocytes (red blood cells)⁵⁷, but in the three decades since, the ED technique has still not

become a preferable method for cell mechanics studies⁵⁸. A brief history of the ED technique is included in (§2.1.4.). In the following section, the experimental challenges and limitations of the ED method are discussed.

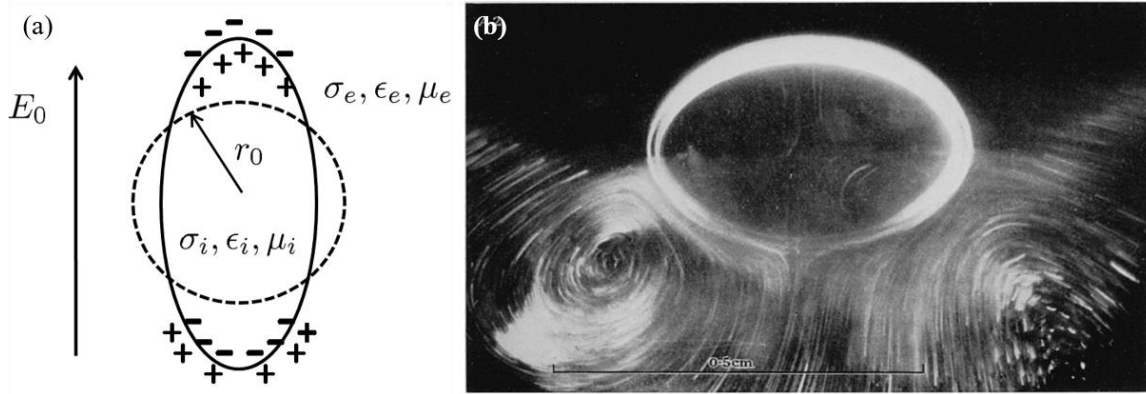


Figure 2.3 (a) A schematic presentation of electrodeformation (ED) in the presence of a DC electric field E_0 ; the dashed circle is the original shape, the solid line is the elongated shape, and, depending on the dielectric properties, it deforms into a prolate or oblate shape⁵⁷. A silicon oil drop, exposed to an external DC electric field, shows the ED and flow pattern both inside and outside of the drop (Taylor's classic study was published in 1966⁵⁹).

First, a major drawback to using the ED method is that sufficient deformation requires high electric field strengths, and, consequently, the intense field can break down the membrane, causing electroporation. This issue can be overcome by applying high-frequency AC field as described in Schwan's equation⁵⁹. Besides, the high-frequency field protects the electrodes from electrochemical degradation and minimizes the electrolysis effect⁶⁰, however, it requires equipment that can generate high voltages at a high frequency. Therefore, employing MEMS/BioMEMS (microelectrode arrays) is a compelling choice⁶¹ to lower the voltage requirements and is currently easily accessible now. Second, under an AC field, an electroosmotic flow, caused by the double layer on the surfaces of electrodes, introduces another experimental difficulty in regard to optically capturing shape deformation, which is due to cell motion⁶². To inhibit electroosmotic motion and trap the cells, ED chips are typically

designed with surface planar electrodes^{58,63–70}. In this way, the electric field strength becomes nonuniform and the gradient of the electric field strength polarizes the cell's electrode-facing side more than the other side; thus, the unbalanced dipole moment either attracts or repels the cell depending on the ratio of σ_i and σ_e . In general, σ_i is much higher than σ_e therefore the cell moves toward the electrodes. In other words, under the effect of positive-dielectrophoresis, the cell becomes trapped on the edge of the electrode. Subsequent pulsing then stretches the cell and upon removal of the pulse it relaxes back to its original shape.

Lastly, the high electric field strength generates Joule-heating that increases the temperature of the solution, and, therefore, the temperature of cell which causes inaccurate measurements. If the temperature reaches 40 °C, the proteins start to denature their structure, therefore, it is necessary to consider temperature rise during the ED. In this study, an increase in temperature was computed, which was found to be less than 2 °C even under the strongest pulse application.

Nonetheless, the ED technique has experimental limitations, and the key focus of this study is the relaxation part in which the external forcing is ceased. By this means, the system can be more simplified, and the major shape change of the cell can be driven by the elasticity of its structure and its responsive fluid motion. This approach has been widely studied particularly in the field of polymer science^{71–73}. Previously, a closed-form solution, developed by Yu *et al.*⁷⁴, for ellipsoidal relaxation, shows the feasibility of this approach.

2.1.3. Maxwell Stress Tensor

To compute the electrical stresses exerting on the cells, Maxwell stress tensor (MST) is the most rigorous way^{75,76}. MST is given as;

$$\ddot{T} = \varepsilon \left(\vec{E}\vec{E} - \frac{1}{2}E^2\vec{I} \right) + \mu_0 \left(\vec{H}\vec{H} - \frac{1}{2}H^2\vec{I} \right) \quad (2.1)$$

where \vec{E}, \vec{H} are the electric field and magnetic field vectors respectively, and \vec{I} is the unit tensor. For an electric field frequency less than in the MHz range, the corresponding wavelength is in order of meters while the electrode configuration in this study was in the order of millimeters. Therefore, the magnetic field effect can be ignored and;

$$\ddot{T} = \varepsilon \left(\vec{E}\vec{E} - \frac{1}{2}E^2\vec{I} \right). \quad (2.2)$$

For a cell assumed to be spherical, the stresses, induced by the electric field, have radial and tangential components. In a steady-state;

$$T_r = -\frac{1}{2}\varepsilon E_\theta^2 \quad (2.3)$$

$$T_\theta = \frac{1}{2}\varepsilon E_\theta^2 \quad (2.4)$$

where r and θ represent the radial and tangential components respectively. Thus, the electrical force exerted on the cells is proportional to the square of the electric field. Introducing an oscillating field, by using $E = E_0 e^{i\omega t}$ and integrating the stresses over the surface of the cell volume yield the dielectrophoretic force equation which is simply⁷⁶,

$$F_{DEP} = 2\pi r^3 \text{Re}(\varepsilon_e) \text{Re}(f_{CM}) \nabla E^2 \quad (2.5)$$

where f_{CM} is the Clausius-Mossotti factor

$$f_{CM} = \frac{\varepsilon_i - \varepsilon_e}{\varepsilon_i + 2\varepsilon_e}. \quad (2.6)$$

So, the total force exerted on the cells can be calculated using Eq. 2.5 once the electric field distribution around the cell is computed.

2.1.4. Electrodeformation in the literature

In this section, the application of the ED technique to biological cells will be chronologically summarized. Earlier works have mostly worked in proving the concept instead of using quantitative analysis. Furthermore, in general, red blood cells have been used due to their floppiness (easy to deform) and accessibility. Ensuing works improved upon this technique by adding different perspectives, different cell types with or without drug treatment, complex 2D/3D modeling, higher quality imaging, postprocessing quality, etc. This literature summary will begin with earlier works before focusing on more recent ED studies of mammalian cells.

The concept of manipulating particles using dielectrophoretic (DEP) forces was introduced by Pohl *et al.* in 1951⁷⁷ and was followed by several theoretical studies⁷⁵. Applying DEP force to the cells was first demonstrated in 1984 by Engelhardt *et al.* with erythrocytes (red blood cells), which showed the linearity and nonlinearity of the elongation of red blood cells with respect to applied electric field strength⁵⁷. It is important to note that, regardless of the deformation obtained with different electric field strengths, the relaxation behavior exhibited strong similarity for different trials. Moreover, the researchers were able to calculate the shear elastic modulus and viscosity of the red blood cells with some simplification and assumption.

Another pioneering work was performed by Zimmermann *et al.*^{78,79}. In their theoretical study, they employed a shell model to calculate the stretching forces on the cell and transmembrane potential, revealing that the deformation forces strongly depend upon frequency and cell polarization which comprises the Clausius-Mosotti factor. They also

discovered an enhancement effect of ED on the electroporabilization and electrofusion of erythrocyte cells⁷⁸.

Wong *et al.*⁶¹ studied the effect of the actin filament organization on the viscoelastic properties of *Brassica oleracea* protoplasts (cabbage cells) by treating them with Latrunculin A, and jasplakinolide. They investigated the frequency dependency of ED by keeping the electric field strength constant at 136V/cm and found a similar trend as Zimmermann *et al.*⁷⁸ in which the deformation reaches a constant value within the frequency range of 2 to 5 MHz. They also examined the relaxation behavior of the cells upon removal of the electric field. Once they normalized the deformed length with the original length, they found that the relaxation behaviors for each group collapsed down into a single curve. This trend was also reported in our recent study⁷⁴. Their study also showed that the relaxation curve exhibited an initial fast drop which was followed by slow timescales. They employed two different methods to analyze relaxation behavior; 1) fitting the relaxation data with a single exponential curve by overlooking the initial drop and 2) using a time spectra method involving a continuous spectrum of exponential functions. The single timescale behavior was correlated with a ratio of viscosity to elasticity while the two timescale behaviors remained qualitatively. They also noted that the theory was limited to a uniform electric field whereas in their experiment due to the design of the electrodes there was strong nonuniformity⁶¹.

MacQueen *et al.*^{58,80} published a series of study on ED with mammalian cells they tested Chinese hamster ovaries (CHO), human promonocytes (U937), human embryonic kidney cells (HEK293), and mouse L929 cells. They built a semi-flexible microchip that generates a fringing, nonuniform electric field to deform the cells and applied almost minute-long pulses. The researchers employed both standard linear solid (SLS) and power-law (PL) models to

estimate the mechanical properties of the cells. They investigated the cytoskeleton effect on the cell's mechanical properties, and found that the cells with thin cortical actin were more greatly deformed than those with thicker cortical actin. Young modulus values varied linearly with cortical actin thickness⁸⁰. Although their model was overly-simplified, they demonstrated the capability of the ED technique using comparative methods.

Another series of studies were published by Guido *et al.*^{60,81} and used a human leukemia cell line (HL-60) as well as healthy and cancerous breast cell lines (MCF-10A and MCF-7, respectively). They microfabricated the ED chip with two parallel planer electrodes distanced 20 μm apart. A commercial software (COMSOL) was employed to compute the total DEP force. They also stretched the cells with minute-long pulsing parameters and utilized comparative methods. In their first work, the effect of the culture medium and cell life cycle on the mechanical properties of the cell were investigated, and older cells (without splitting) seemed to be softer⁸¹. Their second work was a comparison of healthy and cancerous cells' mechanical properties, and, in contrast to general findings, they claimed that the MCF-7 (cancerous) cell line was softer than that of the MCF-10A.

Chen *et al.*⁶⁶ characterized the mechanical and electrical properties of human cervical cancerous cell lines SiHa, and ME-180. They used different frequency-pulses however, the pulse duration was still on the order of a minute. A subpixel image processing algorithm was developed and electrical forces were computed using a 3D model that integrates the Maxwell stress tensor over the cell surface. Overall, they improved the accuracy of quantifying the total force and elongation regardless of the uniformity or nonuniformity of the electric field where previous studies had generally assumed to be uniform. Their experiment results revealed good agreement with the micropipette aspiration method in terms of identifying the elastic modulus.

They also noted that the dielectric parameters of the cells play a critical role in computing total force.

Doh *et al.*⁸² and Du *et al.*⁶³ tested red blood cells from a healthy donor and from patients with spherocytosis or infected with *Plasmodium falciparum* malaria parasites, respectively. They designed microchips arrays that could simultaneously probe the deformability of a large heterogeneous population. and identified a statistically significant variation between healthy and diseased red blood cells, confirming that the ED technique can be used for diagnosis purposes.

A group led by Sun^{65,83} used leukemia NB4 cell lines, that were treated with all-trans retinoic acid (ATRA) or doxorubicin (DOX). The ED chip design was similar to that in previous work, with the gap between electrodes being 20 μm . They also applied long duration pulses for up to three minutes. Their first work with the ATRA treatment was aimed to validate the ED setup to characterize the mechanical properties of cells. Their second work employed actin cytoskeleton modeling to improve the accuracy of the measurements, however the results remained elusive in terms of quantification with the estimated modulus of the nontreated NB4 cell being 140 Pa in the first work and 36 Pa in the second work.

Leung *et al.*⁶⁴ studied platelet cells that are uniquely more sensitive to applied forces. Since platelets are smaller in size than regular cells, the DEP force exerted on platelets is proportional with their volume, meaning they could be $\sim 1,000$ times weaker therefore this team fabricated a triangular-shaped electrode with a 10 μm gap tip-to-tip. Their purpose was to measure the mechanical properties of the platelets without activating them. They assayed the activation before and after the ED test and observed no significant platelet activation.

Urbano *et al.*⁶⁸ investigated the mechanical properties of attached cells, which was unlike previous studies that studied suspended cells. They employed a novel inverted quadrupole dielectrophoretic device and were able to apply a pushing force to move the cell's centroid, thus correlating the displacement with the elastic modulus. They used healthy and cancerous breast cell lines (MCF-10A, and MCF-10A-NeuT), demonstrating that cancerous cells exhibited greater centroid displacement, which indicated smaller elastic modules in their conditions. They confirmed these results by also using atomic force microscopy.

Teng et al. from the Peking University group^{69,84} used typical breast cancer cell lines MCF-7 and MDA-MB-231. They employed a classical ED chip with a 20 μm electrode gap. In general, they applied 20-second-long pulse durations and identified the mechanical properties of the cells based on the Kelvin-Voigt viscoelastic model. In their first work, they basically established and validated the ED platform using TGF- β 1 treated and nontreated cell; in the second work, they quantified the cell cycle effect on the mechanical properties of the cells. They also developed a 3D computational model that accounts for the cell's viscoelastic properties.

Overall, significant improvements have been theoretically achieved, especially by implementing the computational method while solving electric field effect under nonuniform fields. However experimental capabilities have not been fully utilized. For instance, the effect of the pulsing duration and relaxation part upon the removal of the electric field have been overlooked. Unlike other methods, the ED technique has the capability to exert strong enough forces to rapidly deform cells. Additionally, the ED technique suffers from a lack of standardization, and, therefore it is still not considered a preferable assay by cell mechanics researchers⁵⁸.

2.1.5. Statement of Objectives

The ED technique promisingly demonstrated the unique capabilities compared to other methods. Foremost, it is easy to implement, as it does not require a high-cost equipment setup, and it is easy to operate, with no need for skilled technicians. Plus, emerging MEMS technology provides cost-effective and accessible solutions for microchip developing. Secondly, it is a high-throughput technique that can simultaneously and rapidly characterize thousands of cells. Particularly in biological studies, it is essential to collect statistically significant data. The latest AFM technology can detect 1 to 20 cells per hour, however loading and unloading specimens can take more than an hour^{5,29–31}. Optical stretching can analyze around 60 to 300 cells per hour, which gives it a moderate-throughput⁸⁵. Moreover, a throughput as high as 2,000 cells per hour can be achieved with microfluidic assays and the ED technique⁸². Another important advantage is its being contact-free and label-free. Moreover, the amplitude and frequency domain of the deforming force has a wide ranging from pico-newton to nano-newton, and from milliseconds to minutes level. Thus, this method is not restricted to soft materials ($G \ll 100$ Pa).

In this work, a wide range of pulse application is studied to understand the effect of pulsing duration on cellular mechanical properties. Specifically, the pulsing durations used in this study varied from milliseconds to minutes, and it was found that the mechanical properties of the cells displayed different characteristics depending on pulse duration.

The results of this study revealed two distinctive regimes through relaxation for which relaxation timescales were proportional with pulsing duration or independent of pulsing duration. In light of these findings, it can be hypothesized that the cellular structure is a dynamic system, therefore, its intrinsic mechanical properties can be extracted in a regime

independent of the pulsing duration. By this means, the inconsistency of the mechanical properties, reported in the literature up to 1,000-fold, can be ameliorated and a standard for extracting mechanical properties can be established.

2.2. Materials and Methods

2.2.1. Cell Culturing

MDA-MB-231, MCF-7, and MCF-10A cells were obtained from the American Type Culture Collection (ATCC, Manassas, VA). Glioblastoma multiforme (GBM) cells were kindly provided by Ramsey A. Foty, New Jersey Robert Wood Johnson Medical School, New Brunswick, NJ. Cells were maintained in a cell culture incubator (5% CO₂, 95% humidity, 37 °C) in Dulbecco's Modified Eagle's Medium (Sigma-Aldrich, St. Louis, MO) supplemented with 10% fetal bovine serum, 1% Penicillin-Streptomycin, and 1% L-Glutamine (Sigma-Aldrich). Cells were trypsinized in the incubator for five minutes using 0.5% trypsin/EDTA (Sigma-Aldrich), which was followed by centrifugation (Allegra X-21, Beckman Coulter, Brea, CA) in culture media for two minutes at 2000 rpm and then twice in ED isotonic buffer containing 250 mM sucrose. The osmolarity and electrical conductivity were measured with an osmometer (3D3 Osmometer, Advanced Instruments, Norwood, MA) and a conductivity meter (CON 6, Oakton Instruments, Vernon Hills, IL), which were adjusted to 310mOsm/kg and 10 μ S/cm, respectively. To ensure cell viability and membrane integrity during the experiment 1% (v/v) 40 μ g/ml Propidium Iodide (Molecular Probes, Inc., Eugene, OR) was added to the ED buffer.

2.2.2. Electrodeformation & Relaxation Experiment Setup

ED pulses were generated with a function generator (Tektronix AFG3022C, Melrose, MA) and amplified by a high-frequency, high-voltage amplifier (Trek Model PZD 350, Lockport, New York, NY). The ED chip was placed on an inverted microscope (Olympus IX71, Center Valley, PA) with a 40x objective. Electrical connection to the microelectrode

chips was supplied by adhesive copper tapes. The ED-relaxation (ED-R) process was recorded with a synchronized high speed-camera (pco.edge sCMOS, PCO AG, Kelheim, Germany), with most of the experiments recorded at 1,000 fps. The schematic of the experiment setup, an actual ED chip on the microscope and an exemplary cell image are presented in Figure 2.4.

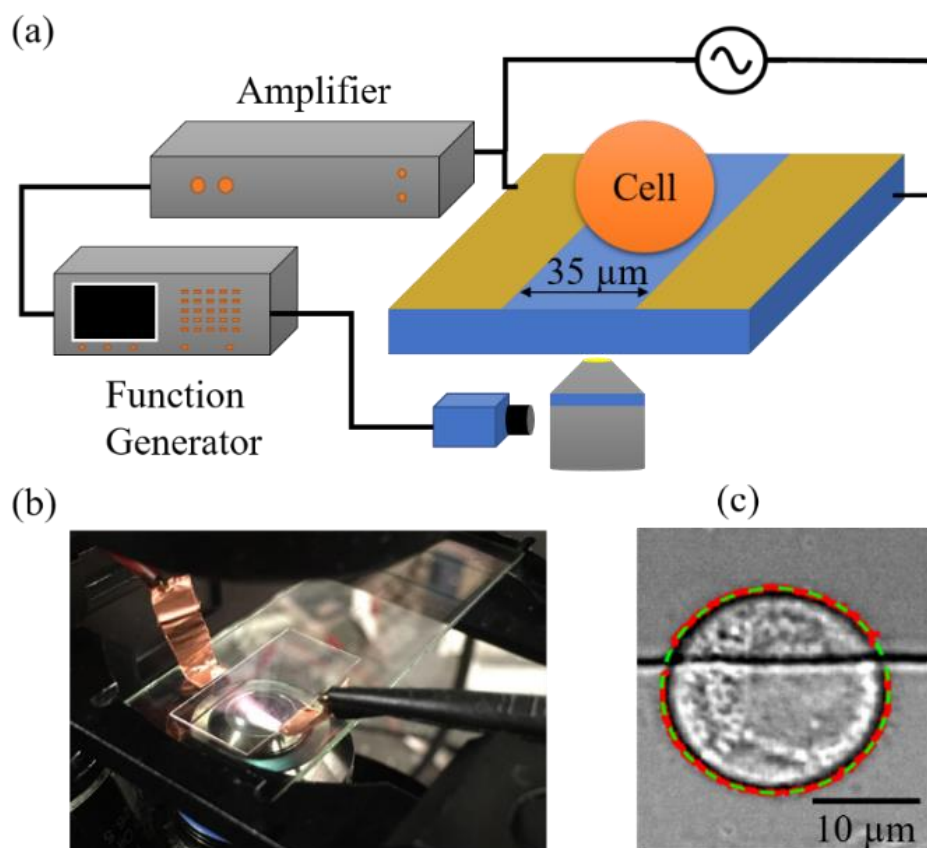


Figure 2.4 (a) Schematic of ED-relaxation (ED-R) experiment setup. High frequency and amplitude electric pulses were applied to the cell suspension. Cell deformation and relaxation were recorded with a synchronized high-speed camera. (b) A photograph of actual ED-R chip. (c) An exemplary image of a trapped cell on the ED-R chip the horizontal black line is the edge of the ITO electrodes and the red and green lines around the cell are the edge detection points of the cell and the ellipsoidal fitting, respectively.

2.2.3. Cell Trapping and Stretching Protocol

Approximately 40 μl of the cell solution (200 cells/μl) was dropped on the ED-R chip. A coverslip was gently placed on top of the solution to avoid cell motion due to flow. Prior to the ED, cells were trapped on the edge of the ITO electrodes, as shown in Figure 2.4c. Owing

to the design of the ED-R chip, applied electric pulses between parallel electrodes generate a non-uniform electric field, and dielectrophoretic (DEP) forces are exerted on the cells and cause them to sag on the edge of the ITO electrode. The trapping electric field is usually one-twentieth or one-tenth of the ED field strength and was applied until the cells were steadily placed on the edge of the ITO electrode. Subsequently, the cells were exposed to high frequency and amplitude electric pulses. High-frequency AC, ranging 1 to 10 MHz electric field, was used to avoid electrolysis and electroporation effects. The pulsing protocol, listed in Table 2-1, ensures the occurrence of ED. Upon pulse cessation, the deformed cell shape relaxes to its original shape (or, at time, close to its original shape). Generally, two different pulsing procedures are employed to deform cells; repeatedly applying the same pulsing parameters (e.g., frequency, amplitude, and duration) on the same cell and the increasing the amplitude of the pulse for each pulsation. The interval between pulses ensures that the deformed cell's shape relaxes to steady-state. The ED-R process was captured via a synchronized high-speed camera. Before and after all ED-R process, a cell membrane integrity test was performed using Propidium Iodide (PI), a non-permeant nucleic acid marker. When cells lose their membrane integrity, PI enters the cell and binds with cell's DNA or RNA. Upon binding, it fluoresces with 535 nm excitation and 617 nm emission. The cells that failed the PI test were discarded from the subsequent analysis due to their impurity.

2.2.4. Image Processing and Data Analysis

A custom-made image processing code was developed in MATLAB (MathWorks, Natick, MA). The electrode region was selected manually and ignored for edge detection, and Figure 2.5a shows the intermediate steps of the image processing. First, a hollow-shaped

region of interest was selected manually then, a gradient-based Canny edge detection algorithm was used to identify the cell membrane. Using a region of interest improved the speed of detection 20-fold. Finally, detected membrane points (as shown in the middle image of Figure 2.5a) were best-fitted by an ellipse. Shape factor is defined as a ratio of the long and short axis of the ellipse ($\epsilon = a/b - 1$). The change in the shape factor with respect to time was obtained using image processing, as shown in Figure 2.5b. Moreover, the shape factor increased during pulsation and upon cessation of the pulse, it relaxed back to its original state.

Table 2-1 The ED experiment setup provides sufficient forcing to deform cells with high electric field strength while avoiding electrolysis and membrane breakdown with high-frequency pulses. Pulsing parameters are listed here.

<i>Electric Field</i>	1 – 20 [kV/cm]
<i>Frequency</i>	5 – 7 [MHz]
<i>Pulse duration</i>	0.01 – 100 [s]
<i>Recording speed</i>	30 – 1,000 [fps]

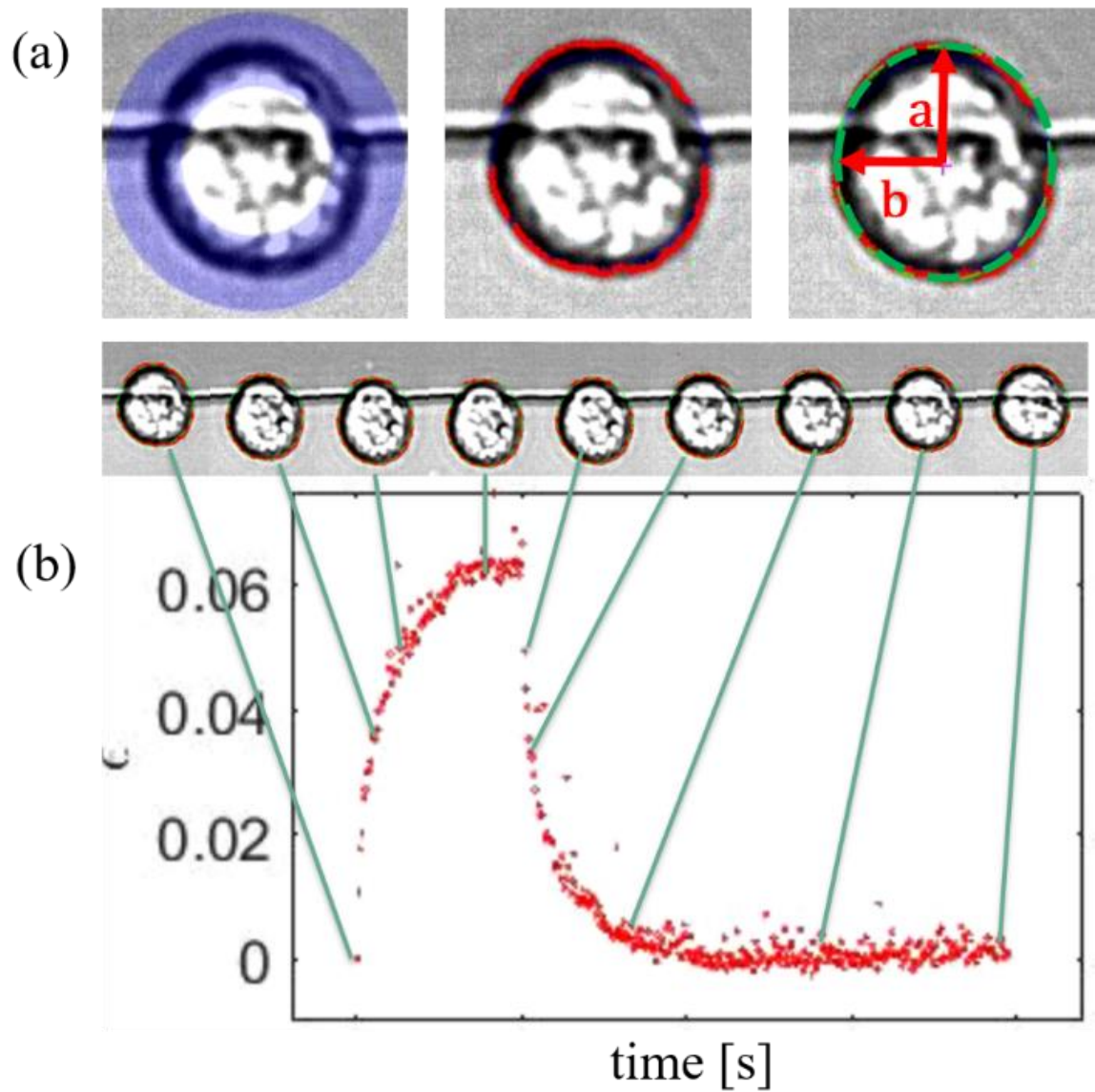


Figure 2.5 Nearly 2,000 frames for each case were analyzed using a custom-made code in MATLAB. (a) shows the intermediate steps of cell membrane detection a hollow region of interest (in the left image colored in blue) is defined to speed-up the processing then, the cell membrane is spotted using a gradient-based edge-detection method (the red points in the middle image) finally, an ellipse shape is best-fitted (dashed green line in the right image). The shape factor (ϵ) is defined as the ratio of the long and short axes. In (b), an exemplary image sequence demonstrates the electrodeformation-relaxation process, and the shape factor change is plotted with respect to time. It is noted that the movement of the cell on the electrode does not affect the image processing.

2.3. Results

2.3.1. Electric Field Strength Effect on Electrodeformation

Four cell types were tested using various ED pulses, and the amplitudes and duration of these pulses ensured the occurrence of deformation. Mostly, the cells were exposed to consecutive pulses with increasing field strength. In Figure 2.6a, the shape factor changes of the four different MDA-MB cells under 0.5 s pulsing are presented. Cells deformed toward the direction of the electric field, and, upon removal of the pulse, they relaxed back to their original shape. Although the field strengths used in this study were one order of magnitude higher than shown in Figure 1.2, the estimated transmembrane potentials, V_m , according to Eq. 1.8 are $5.46\text{e-}5$ V, $8.19\text{e-}5$ V, and $1.1\text{e-}4$ V. Therefore, the electroporation effect can be ignored. Note that the ED electrodes are surface electrodes and the electric field is nonuniform, thus, the field might not be as strong as estimated. Additionally, PI tests were performed before and after each ED-R experiment. Cells experiencing a considerable PI intensity signal change were disqualified from the analysis. It was observed that the number of disqualified cells were few (1 to 2%), and the PI signal was not correlated with the pulsation parameters. It is probable that these cells had lost their membrane integrity due to transportation or unknown biological reasons.

The relaxation process takes slightly longer than pulsation time. It should be noted that Figure 2.6a shows the first 0.5 s of the relaxation data, and the following pulses were applied when a full-recovery was reached. As expected, the highest deformations observed at the end of the pulsation increased with the strength of the field. The dielectrophoresis (DEP) force is proportional to the square power of the field strength, as given in the Eq 2.5, hence, the maximum strains were expected to be proportional with the square power of the electric

field strength⁷⁹. In Figure 2.6b, the maximum strains, reached at the end of the pulse, are plotted against the square of the applied electric field strengths. Although the maximum strains seem to correlate linearly with E^2 for each cell, there is not a universal deformation rate for all four cells. For instance, in the 6 V_{pp} case, the deformation differed more than 50% between Cell 2 and Cell 3, while this difference vanished in the 9 V_{pp} case. It seems like there were other mechanisms interfering with the deformation of the cells, such as a memory effect from the previous deformation or variation in the dielectric properties of the cells. Therefore, the relaxation approach of characterizing mechanical properties regardless of the deformation part simplified the problem by removing external forcing.

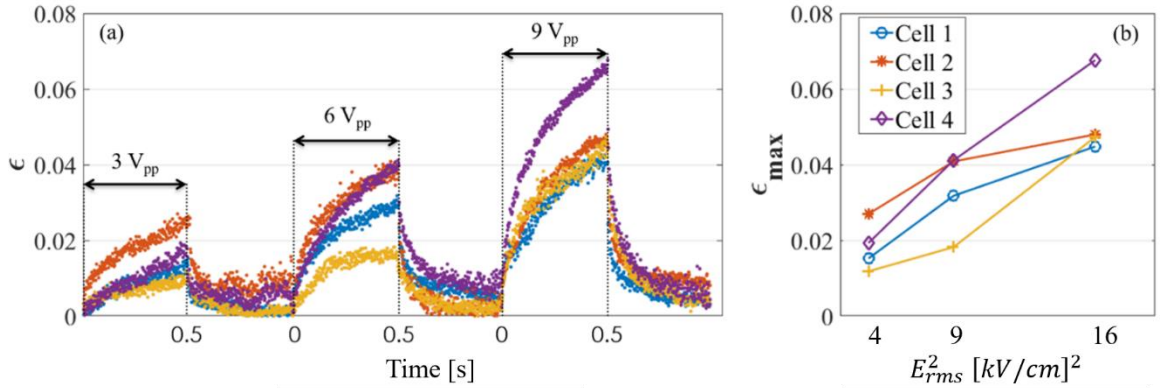


Figure 2.6 (a) Shape factor changes of four different MDA-MB cells under consecutively increasing pulsing; each pulse was 0.5 s long at 7 MHz, and the relaxation recorded was almost 1 s long, but only the first 0.5 s of the relaxation is plotted. (b) The maximum deformation achieved at the end of the pulse is plotted against the square of the applied voltage.

2.3.2. Extracting Relaxation Timescales

Upon removal of the pulse, cells (mostly) relax back to their original shape, as shown in Figure 2.6a and Figure 2.7. The former plot illustrates the shape change of the entire ED-R process whereas the latter plot shows only the relaxation part in logarithmic y-scale. Complete recovery of the shape generally takes longer than the deformation time. It can be also seen in Figure 2.7a that the relaxation parts exhibit similar behaviors regardless of

deformation level. It is clear in logarithmic scale that, relaxation consists of two regimes, 1) fast initial drop followed by 2) a slow decrease. This behavior is consistent with our previous work and many other cell relaxation studies^{61,74,84,86,87}. As shown in Figure 2.7b, a double exponential curve fitting captures the relaxation behavior with a R^2 value of 0.96, which provides two timescales. The existence of timescales was validated with time spectral analysis, as described in⁸⁸. Details on timescale extraction are provided in our previous work⁷⁴, in which it was found that the relaxation behaviors of the various types of vesicles presents similar relaxation behavior regardless of deformation^{74,86}. The mechanical properties of the vesicles such as surface tension and, bending rigidity, were extracted from a closed-form solution that relies on similarities in relaxation behavior. Following a similar strategy, this study proceeded to another stage in which various cancer cell types, like MCF-7, MDA-MB-231, and GBM and healthy breast cell MCF-10A, were used.

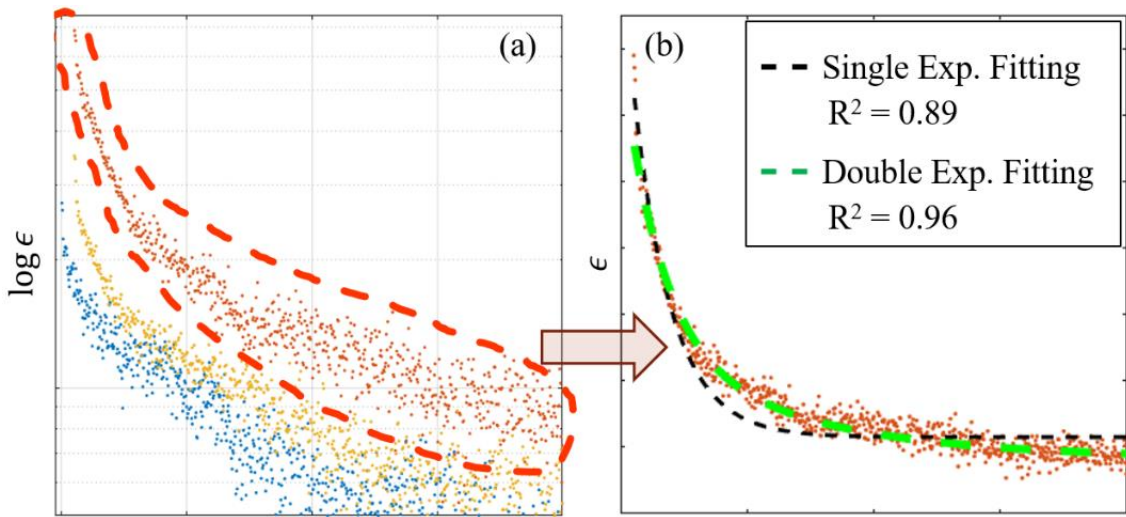


Figure 2.7 An exemplary plot that shows the procedure of extracting relaxation timescales from the data. (a) The shape factor changes in a semilog-y plot. (b) Single and double exponential best-fitting curves for the data points, double exponential fitting more accurately captures the decay.

2.3.3. Relaxation Timescales with Respect to Pulse Duration

It was found that the relaxation process takes place in the same order of magnitude as the stretching time. For example, after 0.5 s of stretching pulsation, the shape recovery time also took nearly 0.5 s, as seen in Figure 2.6. Then, we aimed to investigate the relationship between relaxation timescales and pulsing duration. Due to the experiment setup, a wide range of pulse durations, from tens of milliseconds to tens of seconds, were applied to the cells. It was found that recovery took longer with longer pulse durations; however, for the short pulse durations, a transition region was detected in which the relaxation timescales were no longer proportional with pulsing time. The timescales, obtained from double exponential fitting, can be defined as “short” (τ_{short}) and “long” (τ_{long}) timescales and they were plotted against the pulse durations. In Figure 2.8, the relaxation timescales of the MDA-MB-231 cells are presented. Two distinctive regimes were observed; 1) relatively long pulse region, with relaxation timescales proportional with pulsing duration and, 2) short pulse region, with relaxation timescales independent of pulsing duration. These two regimes separated around ~ 50 to 100 ms, a transition time (t_c) consistent with literature^{89–91}. In the second region (left hand side of t_c), both long and short timescales did not change significantly; however, due to limitations in camera speed (2,000 fps at most), time resolution was less than 2 kHz. In Table 2-2, short and long relaxation timescales for the second region are listed to show the miscorrelation between the timescales and pulsing durations. The transition point was estimated with a linear regression in which the linear fitting best-fit with the data points.

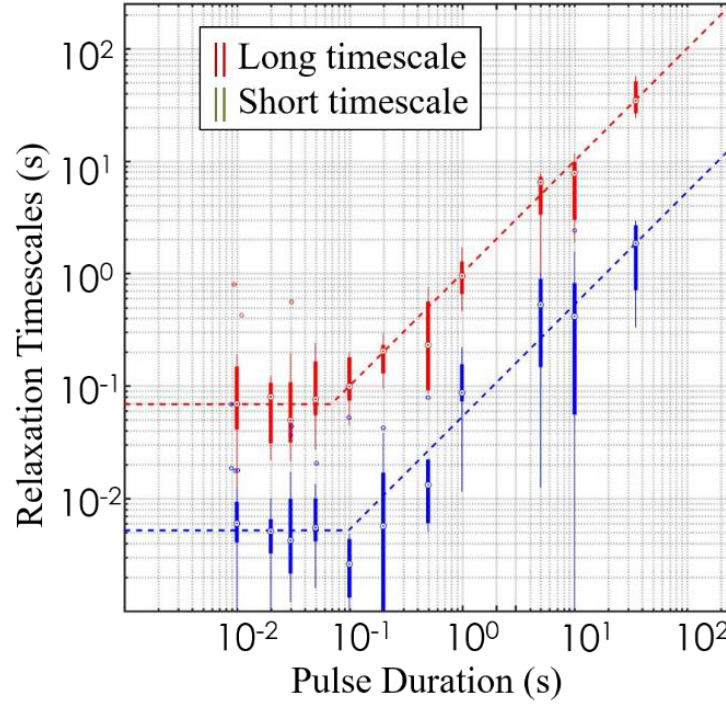


Figure 2.8 The relaxation timescales for the MDA-MB-231 cells with respect to pulsing duration are plotted. Each point is presented with a box and whisker plot, in which the box is within the 25th and 75th percentile, and the median value is marked with a circle.

Table 2-2. Listed the medians of the long and short relaxation timescales for the MDA-MB-231 cells before the transition point in which timescales were no longer proportional with pulsing duration (t_p).

t_p	10 ms	20 ms	30 ms	50 ms	100 ms
τ_{long}	69.38	80	49.6	75.96	99.14
τ_{short}	6.00	5.11	4.25	5.49	2.61

Similar trends in relaxation timescale were also found for other cell types (MCF-7, MCF-10A, and GBM), as shown in Figure 2.9. The transition times, listed in Table 2-3, were typically under 100 ms. The discrepancy in the transition points between the long and short timescales were not clear due to the lack of theoretical model; however, as mentioned, the time resolution of the experiment was limited to 2 kHz; therefore, this difference might not

be physical. In the following section, the physical interpretation of these results and hypothesis will be discussed.

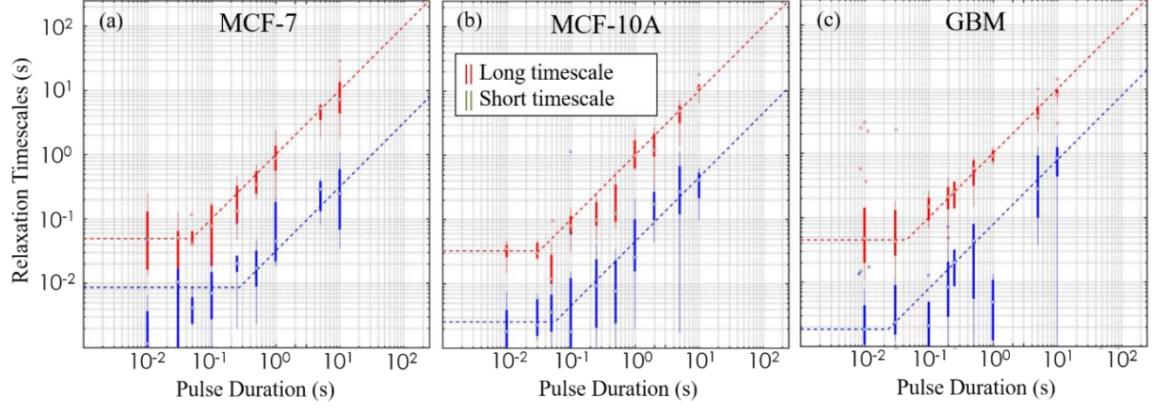


Figure 2.9 The relaxation timescales for the MCF-7, MCF-10A, and GBM cells with respect to pulsing duration are plotted. Each point is presented with a box and whisker plot, in which the box is within the 25th and 75th percentiles, and the median value is marked with a circle.

Table 2-3. Listed transition times (t_c) for long and short relaxation timescales ($t_{c,long}$ and $t_{c,short}$). Transition points for the short relaxation timescales fluctuate due to the scatteredness of the data, whereas the transition points for the long relaxation timescales are around ~ 50 ms.

t_c	MDA-MB	MCF-7	MCF-10A	GBM
$t_{c,long}$	68 ms	49 ms	32 ms	45 ms
$t_{c,short}$	93 ms	273 ms	56 ms	23 ms

2.4. Discussion

ED is a unique method that has the capability to characterize the mechanical properties of cells at both high-frequency and low-frequency domains. It is possible to generate sufficiently strong pulses to deform any kind of cell while avoiding electroporation, as explained in Ch.1, and electrolysis⁵⁹. The present work demonstrated the mechanical characterization of four different mammalian cell types (MDA-MB-231, MCF-7, MCF-10A, and GBM) using the ED-R approach at high and low-frequency domains. More accurate information about each cell's mechanical properties can be obtained from the relaxation part, since it is independent of deformation level and external forcing is absent⁷⁴. The timescale analysis of the relaxation part showed that relaxation dynamics can be best captured with a double exponential decaying curve, which yields two timescales. Furthermore, these timescales were closely related to pulsing duration. Next, a broad range of pulsing times was applied to probe cellular response at different frequency domains. A dual regime was identified in which relaxation timescales were proportional with pulsing duration as well as independent of pulsing duration, which agrees with⁸⁹⁻⁹¹. Extraction of the mechanical properties is a task that is currently undergoing; however, this study accentuates the importance of experimental parameters in improving the ED-R technique and suggests a regime for characterizing mechanical properties that is independent of a confounding biological process.

2.4.1. Electric Field Strength Effect on Electrodeformation

The electric field strength had a quadratic effect on the DEP force as given in Eq 2.5; thus, the deformation ratio was expected to increase with respect to field strength, as reported in earlier works with red blood cells (RBC)^{79,92}. RBCs are essentially a biconcave liquid capsule

enclosed by a membrane⁹³. Therefore, stretching RBCs requires relatively less force and the elongation ratio can be high (around 60 – 80%) without rupturing the cell membrane. Therefore, electric field strength is an important experiment parameter for identifying mechanical properties or pathological differences. In other words, in RBCs the shape change ratio is relatively higher than in other cell types, which provides a significant distinction between deformation levels due to pulse strength. Similarly, if there is any unusual deformability behavior in a group of cells, it can be more clearly distinguished by increasing the field strength hence, the deformability deviations can be amplified. There are many successful studies that have differentiated between healthy and abnormal RBCs^{63,82}. The effect of field strength has also been demonstrated with drugged (0.4% paraformaldehyde treated) and normal platelet⁶⁴ and with/without DOX treated NB4 cells⁶⁵. On the other hand, for regular cell lines without drug treatment, the field strength effect seems to be nebulous in the literature (i.e. with MCF-7 and MCF-10A cells⁶⁰, SiHa cells⁶⁶, and stem cells⁶⁷). This indicates that a significant modification of cellular structure occurs, thus the mechanical properties of drug-treated cells vary for each study.

The results in Figure 2.6b show that increasing field strength also increases deformation level; however, variation, even within the same cell line, was too high to be distinctive. The apparent lack of correlation can be attributed to different sources of uncertainties. For example, the size distribution of the cells was between 10 to 19 μm , which caused the nonuniformity of the DEP forces⁹⁴. As shown in Eq. 2.5, the DEP force is proportional to the cubic power of the cell radius. Another reason for this fluctuation might be the life cycle of the cells⁸⁴ or their cultivation times⁸¹, which can alter deformability. As a result, cell deformation using an electric field is a complex problem, and, therefore the present work focused on the relaxation part instead of deformation.

2.4.2. Relaxation Timescales

A different way to approach to ED process is to investigate relaxation behavior. In theory, viscoelastic materials store energy during deformation and then dissipate it through relaxation according to their properties⁹⁶. Thus, the relaxation dynamics of the soft matter reveals viscoelastic mechanical properties. Likewise, the relaxation dynamics of the deformed cells might help extract mechanical properties and bring several advantageous. First, relaxation is independent from the deformation ratio; thus, it eliminates this complication mentioned above. Second, the absence of external forcing simplifies the modeling, and, additionally, relaxation trends seem to be similar with various pulsing conditions. Relaxation behavior has a fast initial drop and slower recovery dynamics, as reported in^{80,97,98}. Therefore, it can be assumed that a double-exponential curve-fitting resulting in two timescales (τ_{short} : Short timescale, and τ_{long} : Long timescale) sufficiently captured the relaxation dynamics, as shown in Figure 2.7b. Engelhardt *et al.*⁵⁷, also proposed a double-exponential function, and these two timescales differed by an order of magnitude in seconds. Additionally, a time spectral analysis was performed to confirm the existence of the timescales. Our previous work suggests that the first initial descent (the entropic regime) is governed by bending rigidity, and the second, slower decay is a constant-tension regime in which the long relaxation timescale is correlated with the inverse of the membrane tension in the spherical state of the cell⁷⁴. The initial membrane tension is not an intrinsic property of the cell, and can be modulated by external factors such as osmolarity. The results in Figure 2.8 shows that the long timescales, τ_{long} , below the transition time are nearly equal with each other; however, the relaxation timescales are proportional to the stretching time above transition time. This phenomenon implies the occurrence of consequential modifications of the cellular structure during the deformation process. Trepats *et al.* also reported upon the similar universal behavior observed here among

various drug-treated and nontreated cell types⁸⁹. They claim that during the deformation of cells, the rate of remodeling kinetics expeditiously increased more rapidly compared to its unstretched state. In the following section, the present results support this physical interpretation.

2.4.3. Two Distinctive Regimes

The ED experiment platform was designed in a way to control stretching force and duration. As mentioned in § 2.1.2, the ED approach exhibits unique capabilities, such as being contact-free, label-free, and having a high throughput. Furthermore, by tailoring pulsing amplitude and duration, we were able to sufficiently deform the cells for optical detection and for a wide span of stretching duration. The relaxation timescales showed two similar distinctive regimes that scaled with pulsing duration and were independent of pulsing time. It is unsurprising that the relaxation timescales corresponding to the viscoelastic properties of the cells had a strong frequency dependency as previously reported by ^{89,91,99–102}. Lieleg *et al.* also studied the binding/unbinding dynamics of the actin filament network and found that at a high-frequency domain, the unbinding of the cross-linked network of actin seems to be stationary, whereas at a low-frequency domain, the contribution of actin crosslinks dominates the viscoelastic properties⁹⁹. The present results confirmed this behavior through the ED-R approach. Moreover, this behavior clearly indicates that cells are adaptive and modify their mechanical, chemical, or biological state under physical forcing⁸⁹.

The viscoelastic properties of some biological materials, like blood clots, fibrin, or collagen networks, have been well modeled and validated with crosslinked polymers. The characteristics of these biomaterials include relatively large elastic moduli and stress-stiffening

behaviors¹⁰³. However, in the case of living cells or tissues, they exhibit a high degree of heterogeneous structuring that actively undergoes biological and chemical reactions. Therefore, in the last two decades, researchers have sought a robust characterization technique to confidently extract the mechanical properties of cells, so that it can be employed to diagnose pathologies and help develop more beneficial therapies. As mentioned in § 2.1.1, there are many experimental techniques that have been developed; nevertheless, difficulties and inconsistencies in measurements have caused a lack of rigorous feedback for theoreticians. Thus, model studies remain challenging and immature due to either their oversimplification or lack of transient framework. Up to now, there are two main streams of modeling; 1) linear or nonlinear viscoelastic models and 2) rheology, particularly, soft glass rheology (SGR). Regarding the present experimental conditions, two prominent models can be considered a strong candidate for interpreting our results⁹⁰.

The GWLC model is an extension of the worm-like chain (WLC) model, in which a semi-flexible chain is subjected to tension and thermal fluctuations. This theory was successful in explaining the mechanical properties of actin filament-based gels in which F actin is the constituting component of the cell cortex. A moduli scale with universal exponent of $3/4$ power⁹¹; however, in many cell studies and in the present study (data not shown), a much weaker power, like $1/2$ or $1/4$ was often observed. To emulate this difference, this theory is strengthened with rheology part. The “glassy” part of the model inherits principles from SGR models in which the cytoskeleton is composed of many disordered elements that connect to each other with weak bindings. Due to these weak interactions, elements can be unbound/bound to each other which then dictates fluidization or solidification. The weak powers arise from the unbinding process between actin filaments in which the viscous effects dominate. In other words, the cell cortex is not simply made of bundles of actin filaments; it

is structuralized by actin filaments that bound together in 2D or 3D networks at certain locations. So, when cells are subjected to a force, the unbinding process that takes place introduces a lower power. In summary, the WLC model accounts for the bending and torsion of the actin filament network, whereas the SGR regime includes not only the deformation of the actin filament network but the interaction of the network as well, (e.g., binding/unbinding process of the filaments). Additionally, the GWLC model might explain the two distinctive regimes identified in Figure 2.9. In conclusion, the WLC model is suitable at high-frequency domains and the SGR is suitable at low-frequency domains^{104,105}.

It is believed that the discrepancy in the mechanical properties of cells, reported in the literature, which employed various methods, including ED method, is due to overlooking the cell's adaptive properties. According to our knowledge, most of these ED studies applied relatively long pulses anywhere between ten seconds and minutes. Additionally, other techniques are also at the low-frequency domain. For example, Krieg *et al.*¹⁰⁶ employed AFM method to measure the stiffness of malign cells, which took on average, 10 seconds to obtain a measurement. Likewise, Maître *et al.*¹⁰⁷ used micropipette aspiration method and applied 7 Pa of suction pressure for 10 seconds to reach a steady-state. Therefore, it is hypothesized that, to characterize the undisturbed mechanical properties of the cell, one should consider the techniques in the WLC regime.

2.5. Conclusion

Mechanical properties of biological cells are closely linked with their physiological and pathological states. An ED-R technique was used to characterize the mechanical properties of the cells in suspension. The data were analyzed and two distinctive regimes were identified. If cells were deformed for shorter than a threshold of approximately tens of milliseconds, the relaxation timescales are independent of the pulse duration, indicating invariant mechanical properties. When they were deformed for longer than the threshold, the relaxation duration scales linearly with the pulse duration, which is typically seen in soft glassy materials. This behavior was found to be coherent across the various cell types examined, providing insights into understanding the cellular response to mechanical cues. The technique promises ease of implementation and high-throughput for large-scale cell mechanical analysis.

2.6. References

1. Unal, M. et al. Micro and Nano-Scale Technologies for Cell Mechanics, Micro and Nano-Scale Technologies for Cell Mechanics. *Nanobiomedicine* 1, 5 (2014).
2. Gurkan, U. A. & Akkus, O. The mechanical environment of bone marrow: a review. *Ann Biomed Eng* 36, 1978–1991 (2008).
3. Sun, Y. et al. Mechanics Regulates Fate Decisions of Human Embryonic Stem Cells. *PLOS ONE* 7, e37178 (2012).
4. Wu, P.-H. et al. A comparison of methods to assess cell mechanical properties. *Nature Methods* 15, 491 (2018).
5. Deng, X. et al. Application of atomic force microscopy in cancer research. *Journal of Nanobiotechnology* 16, 102 (2018).
6. An, S. S., Fabry, B., Treppe, X., Wang, N. & Fredberg, J. J. Do Biophysical Properties of the Airway Smooth Muscle in Culture Predict Airway Hyperresponsiveness? *Am J Respir Cell Mol Biol* 35, 55–64 (2006).
7. Lee, G. Y. H. & Lim, C. T. Biomechanics approaches to studying human diseases. *Trends in Biotechnology* 25, 111–118 (2007).
8. Trickey, W. R., Lee, G. M. & Guilak, F. Viscoelastic properties of chondrocytes from normal and osteoarthritic human cartilage. *Journal of Orthopaedic Research* 18, 891–898 (2000).
9. Bao, G. & Suresh, S. Cell and molecular mechanics of biological materials. *Nat Mater* 2, 715–725 (2003).
10. Moeendarbary, E. & Harris, A. R. Cell mechanics: principles, practices, and prospects. *Wiley Interdisciplinary Reviews: Systems Biology and Medicine* 6, 371–388 (2014).
11. Deguchi, S., Maeda, K., Ohashi, T. & Sato, M. Flow-induced hardening of endothelial nucleus as an intracellular stress-bearing organelle. *Journal of Biomechanics* 38, 1751–1759 (2005).
12. Guilak, F., Tedrow, J. R. & Burgkart, R. Viscoelastic Properties of the Cell Nucleus. *Biochemical and Biophysical Research Communications* 269, 781–786 (2000).
13. Cross, S. E., Jin, Y.-S., Rao, J. & Gimzewski, J. K. Nanomechanical analysis of cells from cancer patients. *Nature Nanotechnology* 2, 780–783 (2007).
14. Xu, W. et al. Cell Stiffness Is a Biomarker of the Metastatic Potential of Ovarian Cancer Cells. *PLOS ONE* 7, e46609 (2012).
15. Tse, H. T. K. et al. Quantitative Diagnosis of Malignant Pleural Effusions by Single-Cell Mechanophenotyping. *Science Translational Medicine* 5, 212ra163–212ra163 (2013).
16. Broedersz, C. P. & MacKintosh, F. C. Molecular motors stiffen non-affine semiflexible polymer networks. *arXiv:1009.3848 [cond-mat, physics:physics]* (2010).
17. Microtubules, Filaments | Learn Science at Scitable. Available at: <https://www.nature.com/scitable/topicpage/microtubules-and-filaments-14052932>. (Accessed: 5th March 2019)
18. Fletcher, D. A. & Mullins, R. D. Cell mechanics and the cytoskeleton. *Nature* (2010). doi:10.1038/nature08908
19. Tao, J., Li, Y., Vig, D. K. & Sun, S. X. Cell mechanics: a dialogue. *Rep Prog Phys* 80, 036601 (2017).
20. van Vliet, C., Thomas, E. C., Merino-Trigo, A., Teasdale, R. D. & Gleeson, P. A. Intracellular sorting and transport of proteins. *Progress in Biophysics and Molecular Biology* 83, 1–45 (2003).
21. Kollmannsberger, P. & Fabry, B. Linear and Nonlinear Rheology of Living Cells. *Annual Review of Materials Research* 41, 75–97 (2011).
22. Fung, Y. C. *Biomechanics: Mechanical Properties of Living Tissues*. (Springer-Verlag, 1993).
23. Suresh, S. Biomechanics and biophysics of cancer cells. *Acta Materialia* 55, 3989–4014 (2007).
24. Hessler, J. A. et al. Atomic Force Microscopy Study of Early Morphological Changes during Apoptosis. *Langmuir* 21, 9280–9286 (2005).
25. Li, Q. S., Lee, G. Y. H., Ong, C. N. & Lim, C. T. AFM indentation study of breast cancer cells. *Biochemical and Biophysical Research Communications* 374, 609–613 (2008).
26. Hochmuth, R. M. Micropipette aspiration of living cells. *Journal of Biomechanics* 33, 15–22 (2000).
27. Dao, M., Lim, C. T. & Suresh, S. Mechanics of the human red blood cell deformed by optical tweezers [Journal of the Mechanics and Physics of Solids, 51 (2003) 2259–2280]. *Journal of Mechanics Physics of Solids* 53, 493–494 (2005).
28. Fabry, B. et al. Selected Contribution: Time course and heterogeneity of contractile responses in cultured human airway smooth muscle cells. *Journal of Applied Physiology* 91, 986–994 (2001).

29. Müller, D. J. & Dufrène, Y. F. Atomic force microscopy as a multifunctional molecular toolbox in nanobiotechnology. *Nature Nanotechnology* 3, 261–269 (2008).
30. Rother, J., Nöding, H., Mey, I. & Janshoff, A. Atomic force microscopy-based microrheology reveals significant differences in the viscoelastic response between malignant and benign cell lines. *Open Biol* 4, (2014).
31. Krieg, M. et al. Tensile forces govern germ-layer organization in zebrafish. *Nature Cell Biology* 10, 429–436 (2008).
32. Zhang, Y. et al. Interfacing 3D magnetic twisting cytometry with confocal fluorescence microscopy to image force responses in living cells. *Nature Protocols* 12, 1437–1450 (2017).
33. Deng, L. et al. Fast and slow dynamics of the cytoskeleton. *Nat Mater* 5, 636–640 (2006).
34. Wang, N., Butler, J. P. & Ingber, D. E. Mechanotransduction across the cell surface and through the cytoskeleton. *Science* 260, 1124–1127 (1993).
35. Nieminen, T. A. et al. Optical tweezers: Theory and modelling. *Journal of Quantitative Spectroscopy and Radiative Transfer* 146, 59–80 (2014).
36. Zhang Hu & Liu Kuo-Kang. Optical tweezers for single cells. *Journal of The Royal Society Interface* 5, 671–690 (2008).
37. Berns, M. W. Optical Tweezers: Tethers, Wavelengths, and Heat. in *Methods in Cell Biology* 82, 455–466 (Academic Press, 2007).
38. Ashkin, A. & Dziedzic, J. M. Optical trapping and manipulation of viruses and bacteria. *Science* 235, 1517–1520 (1987).
39. Titushkin, I. & Cho, M. Distinct Membrane Mechanical Properties of Human Mesenchymal Stem Cells Determined Using Laser Optical Tweezers. *Biophysical Journal* 90, 2582–2591 (2006).
40. Hénon, S., Lenormand, G., Richert, A. & Gallet, F. A New Determination of the Shear Modulus of the Human Erythrocyte Membrane Using Optical Tweezers. *Biophysical Journal* 76, 1145–1151 (1999).
41. Liu, Y. et al. Evidence for localized cell heating induced by infrared optical tweezers. *Biophysical Journal* 68, 2137–2144 (1995).
42. Kollmannsberger, P. & Fabry, B. BaHigh-force magnetic tweezers with force feedback for biological applications. *Review of Scientific Instruments* 78, 114301 (2007).
43. Lee, L. M. & Liu, A. P. The Application of Micropipette Aspiration in Molecular Mechanics of Single Cells. *J Nanotechnol Eng Med* 5, 0408011–0408016 (2014).
44. Rodriguez, M. L., McGarry, P. J. & Sniadecki, N. J. Review on Cell Mechanics: Experimental and Modeling Approaches. *Appl. Mech. Rev* 65, 060801-060801–41 (2013).
45. Maître, J.-L., Niwayama, R., Turlier, H., Nédélec, F. & Hiiragi, T. Pulsatile cell-autonomous contractility drives compaction in the mouse embryo. *Nature Cell Biology* 17, 849–855 (2015).
46. Grasland-Mongrain, P. et al. Ultrafast imaging of cell elasticity with optical microelastography. *PNAS* 115, 861–866 (2018).
47. Lautscham, L. A. et al. Migration in Confined 3D Environments Is Determined by a Combination of Adhesiveness, Nuclear Volume, Contractility, and Cell Stiffness. *Biophysical Journal* 109, 900–913 (2015).
48. Charras, G. T., Yarrow, J. C., Horton, M. A., Mahadevan, L. & Mitchison, T. J. Non-equilibration of hydrostatic pressure in blebbing cells. *Nature* 435, 365–369 (2005).
49. Keren, K., Yam, P. T., Kinkhabwala, A., Mogilner, A. & Theriot, J. A. Intracellular fluid flow in rapidly moving cells. *Nature Cell Biology* 11, 1219–1224 (2009).
50. Taylor, G. I. Studies in electrohydrodynamics. I. The circulation produced in a drop by an electric field. *Proc. R. Soc. Lond. A* 291, 159–166 (1966).
51. Zhang, J., Zahn, J. D. & Lin, H. Transient solution for droplet deformation under electric fields. *Physical Review E* 87, (2013).
52. Zhang, J., Zahn, J. D., Tan, W. & Lin, H. A transient solution for vesicle electrodeformation and relaxation. *Physics of Fluids* 25, 071903 (2013).
53. Kummrow, M. & Helfrich, W. Deformation of giant lipid vesicles by electric fields. *Physical Review A* 44, 8356–8360 (1991).
54. Niggemann, G., Kummrow, M. & Helfrich, W. The Bending Rigidity of Phosphatidylcholine Bilayers: Dependences on Experimental Method, Sample Cell Sealing and Temperature. *Journal de Physique II* 5, 413–425 (1995).
55. Riske, K. A. & Dimova, R. Electric Pulses Induce Cylindrical Deformations on Giant Vesicles in Salt Solutions. *Biophysical Journal* 91, 1778–1786 (2006).
56. Peterlin, P. Frequency-dependent electrodeformation of giant phospholipid vesicles in AC electric field. *Journal of Biological Physics* 36, 339–354 (2010).

57. Engelhardt, H., Gaub, H. & Sackmann, E. Viscoelastic properties of erythrocyte membranes in high-frequency electric fields. *Nature* 307, 378–380 (1984).
58. MacQueen, L. A., Buschmann, M. D. & Wertheimer, M. R. Mechanical properties of mammalian cells in suspension measured by electro-deformation. *J. Micromech. Microeng.* 20, 065007 (2010).
59. Marszalek, P., Liu, D. S. & Tsong, T. Y. Schwan equation and transmembrane potential induced by alternating electric field. *Biophys J* 58, 1053–1058 (1990).
60. Guido, I., Jaeger, M. S. & Duschl, C. Dielectrophoretic stretching of cells allows for characterization of their mechanical properties. *European Biophysics Journal* 40, 281–288 (2011).
61. Wong, P. K., Tan, W. & Ho, C.-M. Cell relaxation after electrodeformation: effect of latrunculin A on cytoskeletal actin. *Journal of Biomechanics* 38, 529–535 (2005).
62. Liu, Y. et al. Manipulation of nanoparticles and biomolecules by electric field and surface tension. *Computer Methods in Applied Mechanics and Engineering* 197, 2156–2172 (2008).
63. Du, E., Dao, M. & Suresh, S. Quantitative Biomechanics of Healthy and Diseased Human Red Blood Cells using Dielectrophoresis in a Microfluidic System. *Extreme Mech Lett* 1, 35–41 (2014).
64. Leung, S. L., Lu, Y., Bluestein, D. & Slepian, M. J. Dielectrophoresis-Mediated Electrodeformation as a Means of Determining Individual Platelet Stiffness. *Annals of Biomedical Engineering* 44, 903–913 (2016).
65. Bai, G. et al. Characterization of biomechanical properties of cells through dielectrophoresis-based cell stretching and actin cytoskeleton modeling. *BioMedical Engineering OnLine* 16, (2017).
66. Chen, J. et al. Electrodeformation for single cell mechanical characterization. *Journal of Micromechanics and Microengineering* 21, 054012 (2011).
67. Liu, Y. et al. Electro-Deformation of Fused Cells in a Microfluidic Array Device. *Micromachines* 7, 204 (2016).
68. Urbano, R. L. & Clyne, A. M. An inverted dielectrophoretic device for analysis of attached single cell mechanics. *Lab on a Chip* 16, 561–573 (2016).
69. Teng, Y., Pang, M., Huang, J. & Xiong, C. Mechanical characterization of cancer cells during TGF- β 1-induced epithelial-mesenchymal transition using an electrodeformation-based microchip. *Sensors and Actuators B: Chemical* 240, 158–167 (2017).
70. Qiang, Y., Liu, J. & Du, E. Dielectrophoresis Testing of Nonlinear Viscoelastic Behaviors of Human Red Blood Cells. *Micromachines (Basel)* 9, (2018).
71. Gerashchenko, S. & Steinberg, V. Statistics of Tumbling of a Single Polymer Molecule in Shear Flow. *Phys. Rev. Lett.* 96, 038304 (2006).
72. Priestley, R. D., Ellison, C. J., Broadbent, L. J. & Torkelson, J. M. Structural Relaxation of Polymer Glasses at Surfaces, Interfaces, and In Between. *Science* 309, 456–459 (2005).
73. Hu, Y. T. Steady-state shear banding in entangled polymers? *Journal of Rheology* 54, 1307–1323 (2010).
74. Yu, M., Lira, R. B., Riske, K. A., Dimova, R. & Lin, H. Ellipsoidal Relaxation of Deformed Vesicles. *Phys. Rev. Lett.* 115, 128303 (2015).
75. Jones, T. B. *Electromechanics of Particles* by Thomas B. Jones. Cambridge Core (1995). doi:10.1017/CBO9780511574498
76. General expressions for dielectrophoretic force and electrorotational torque derived using the Maxwell stress tensor method - ScienceDirect. Available at: <https://www.sciencedirect.com/science/article/pii/S0304388697001265>. (Accessed: 30th May 2019)
77. Pohl, H. A., Pollock, K. & Crane, J. S. Dielectrophoretic force: A comparison of theory and experiment. *J Biol Phys* 6, 133–160 (1978).
78. Zimmermann, U. et al. Electromanipulation of mammalian cells: fundamentals and application. *IEEE Transactions on Plasma Science* 28, 72–82 (2000).
79. Sukhorukov, V. L., Mussauer, H. & Zimmermann, U. The effect of electrical deformation forces on the electroporation of erythrocyte membranes in low- and high-conductivity media. *J. Membr. Biol.* 163, 235–245 (1998).
80. MacQueen, L. A., Thibault, M., Buschmann, M. D. & Wertheimer, M. R. Electromechanical deformation of mammalian cells in suspension depends on their cortical actin thicknesses. *Journal of Biomechanics* 45, 2797–2803 (2012).
81. Guido, I., Jaeger, M. S. & Duschl, C. Influence of medium consumption on cell elasticity. *Cytotechnology* 62, 257–263 (2010).
82. Doh, I., Lee, W. C., Cho, Y.-H., Pisano, A. P. & Kuypers, F. A. Deformation measurement of individual cells in large populations using a single-cell microchamber array chip. *Appl Phys Lett* 100, 173702-173702–3 (2012).

83. Zhang, X. et al. Rapid characterization of the biomechanical properties of drug-treated cells in a microfluidic device. *Journal of Micromechanics and Microengineering* 25, 105004 (2015).
84. Teng, Y., Zhu, K., Xiong, C. & Huang, J. Electrodeformation-Based Biomechanical Chip for Quantifying Global Viscoelasticity of Cancer Cells Regulated by Cell Cycle. *Anal. Chem.* 90, 8370–8378 (2018).
85. Balland, M. et al. Power laws in microrheology experiments on living cells: Comparative analysis and modeling. *Phys. Rev. E* 74, 021911 (2006).
86. Yu, M. et al. Coherent Timescales and Mechanical Structure of Multicellular Aggregates. *Biophysical Journal* 114, 2703–2716 (2018).
87. Lenormand, G., Millet, E., Fabry, B., Butler, J. P. & Fredberg, J. J. Linearity and time-scale invariance of the creep function in living cells. *Journal of The Royal Society Interface* 1, 91–97 (2004).
88. Kontogiorgos, V. Calculation of Relaxation Spectra from Stress Relaxation Measurements. *Biopolymers* (2010). doi:10.5772/10275
89. Treppe, X. et al. Universal physical responses to stretch in the living cell. *Nature* 447, 592–595 (2007).
90. Moeendarbary, E. et al. The cytoplasm of living cells behaves as a poroelastic material. *Nature Materials* 12, 253–261 (2013).
91. Deng, L. et al. Fast and slow dynamics of the cytoskeleton. *Nat Mater* 5, 636–640 (2006).
92. Zimmermann, U. et al. Electromanipulation of mammalian cells: fundamentals and application. *IEEE Transactions on Plasma Science* 28, 72–82 (2000).
93. Dao, M., Lim, C. T. & Suresh, S. Mechanics of the human red blood cell deformed by optical tweezers. *Journal of the Mechanics and Physics of Solids* 51, 2259–2280 (2003).
94. Çetin, B., Kang, Y., Wu, Z. & Li, D. Continuous particle separation by size via AC - dielectrophoresis using a lab - on - a - chip device with 3 - D electrodes. *ELECTROPHORESIS* 30, 766–772 (2009).
95. Kumar, R. T. K., Liu, S., Minna, J. D. & Prasad, S. Monitoring drug induced apoptosis and treatment sensitivity in non-small cell lung carcinoma using dielectrophoresis. *Biochim Biophys Acta* 1860, 1877–1883 (2016).
96. Hochmuth, R. M., Worthy, P. R. & Evans, E. A. Red cell extensional recovery and the determination of membrane viscosity. *Biophys J* 26, 101–114 (1979).
97. Wong, P. K., Tan, W. & Ho, C.-M. Cell relaxation after electrodeformation: effect of latrunculin A on cytoskeletal actin. *Journal of Biomechanics* 38, 529–535 (2005).
98. Sung, K. L., Dong, C., Schmid-Schönbein, G. W., Chien, S. & Skalak, R. Leukocyte relaxation properties. *Biophys J* 54, 331–336 (1988).
99. Lieleg, O., Claessens, M. M. A. E., Luan, Y. & Bausch, A. R. Transient Binding and Dissipation in Cross-Linked Actin Networks. *Phys. Rev. Lett.* 101, 108101 (2008).
100. Janmey, P. A. & McCulloch, C. A. Cell Mechanics: Integrating Cell Responses to Mechanical Stimuli. *Annual Review of Biomedical Engineering* 9, 1–34 (2007).
101. Mulla, Y., MacKintosh, F. C. & Koenderink, G. H. Origin of slow stress relaxation in the cytoskeleton. arXiv:1810.08165 [cond-mat, physics:physics, q-bio] (2018).
102. Fabry, B. et al. Time scale and other invariants of integrative mechanical behavior in living cells. *Phys Rev E Stat Nonlin Soft Matter Phys* 68, 041914 (2003).
103. MacKintosh, F. C., Käs, J. & Janmey, P. A. Elasticity of Semiflexible Biopolymer Networks. *Phys. Rev. Lett.* 75, 4425–4428 (1995).
104. Kroy, K. & Glaser, J. The glassy wormlike chain. *New J. Phys.* 9, 416 (2007).
105. Wolff, L., Fernandez, P. & Kroy, K. Inelastic mechanics of sticky biopolymer networks. *New J. Phys.* 12, 053024 (2010).
106. Krieg, M. et al. Tensile forces govern germ-layer organization in zebrafish. *Nature Cell Biology* 10, 429–436 (2008).
107. Maître, J.-L., Niwayama, R., Turlier, H., Nédélec, F. & Hiragi, T. Pulsatile cell-autonomous contractility drives compaction in the mouse embryo. *Nature Cell Biology* 17, 849–855 (2015).
108. Nematbakhsh, Y., Pang, K. T. & Lim, C. T. Correlating the viscoelasticity of breast cancer cells with their malignancy. *Converg. Sci. Phys. Oncol.* 3, 034003 (2017).

Chapter 3

TRANSPORT AND RESEALING DYNAMICS OF TWO PULSE ELECTROPORATION MEDIATED MOLECULAR DELIVERY

3.1. Introduction

Electroporation (EP) mediated molecular delivery has shown a great enhancement in various applications such as gene transport, protein or drug delivery, among many other biochemical methods¹⁻⁹. It can be considered in two main parts; (I) electroporeabilization of the membrane and (II) electrotransportation of target molecules. The presence of suitably chosen external electric field permeabilizes the cell membrane and introduces foreign molecules into the cell cytoplasm¹⁰⁻¹⁴. However, the major disadvantage of this procedure is the death of a significant portion of the cell population due to high voltage application. To overcome this limitation, among various techniques, a two-pulse protocol is used to increase the efficiency of molecular delivery and to preserve more cells alive with suitably chosen pulsing parameters¹⁵⁻²⁹. However, the lack of fully understanding the effect of pulsing parameters still attracts interest of researchers seeking to understand the fundamental mechanisms and optimize delivery and viability. This thesis provides a distinct pulsing design in order to separate permeabilization and delivery clearly and allows to analyze each mechanism separately. The focus of this work is to study the effect of the permeabilization pulse's field strength and delay time between two pulses on molecular delivery of two different-sized Fluorescein-Dextran conjugates (10 kDa and 70 kDa).

3.1.1. Mechanisms of Electroporation Mediated Molecular Delivery

In earlier works, it has been reported that in the presence of external electric field some type of electrical breakdown occurs in the cell plasma membrane³⁰ and consequently the conductance of the membrane increases dramatically³¹. These findings showed that, when an external electric field is applied to the cell membrane, after reaching a critical threshold transmembrane potential, the cell membrane no longer behaves like an insulator, becomes more conductive and allows the extra-cellular foreign molecules to pass through into cytoplasm. E. Neumann *et al.* performed the first gene transfer into mouse lyoma cells by applying suitable electric pulses and presented a simple, easy applicable and efficient way to transport genes into the cells compared to other biochemical techniques¹.

EP mediated molecular delivery can be considered in two main aspects; (I) electroporeabilization of the membrane and (II) electrotransportation of target molecules. It is shown that, for both mechanisms the electrical parameters play important role^{32,33}. Therefore, this study and as many other studies focused on the electrical parameters to better understand the mechanism and improve the efficiency^{15,17,20,28,34–54}. Although, other physiological^{55–58} and cellular^{59–62} effects help to improve the EP procedure, those effects are not scope of this study.

3.1.1.1. Electroporeabilization of the cell membrane

An application of suitably chosen electric pulse to the cell membrane transiently increases the permeability of the membrane. It has been shown that the electrical breakdown of the membrane occurs after reaching a critical transmembrane potential^{34–37}. Also depending on the pulsing parameter, this permeable stage occurs either temporary (reversible) or permanently (irreversible). These reversible and irreversible electroporeabilization have

different application areas, for example in the applications of debacterialization or ablation of solid tumors irreversible electroporation is used^{63–66}, where in the application of drug delivery or gene therapy reversible electroporation is used^{1–9}. To understand the permeabilization mechanism, it is important to know bilayer lipid structure of the membrane. Due to nature of the lipid molecules, the cell membranes functions as a combined resistor and capacitor⁶⁷. Therefore, in the application of an external electric field, the membrane is charged as a capacitor due to accumulation of ions from the surrounding solution⁶⁸. When the applied pulse surpasses the capacitance of the membrane, electroporation takes place^{34–37}. Maintaining the field strength over critical threshold value expands the permeabilization of the membrane. This process is explained as "induction step" and then "expansion step", where in the induction (trigger) step, the applied pulse induces a potential difference across the membrane until a critical threshold value and creates small defects on the membrane (nucleation sites), and then in the expansion step, it extends those defects until a potential equilibrium is reached⁶⁹. Experimentally, this procedure is shown by Hibino *et al.* by using voltage-sensitive dyes^{36,37}. In fact, this dynamic process of pore evolution and statistical distribution is well captured by Smoluchowski equation (SE) as a function of transmembrane potential. In many EP modeling study, this equation is solved to stimulate the pore evolution^{70–72}. As a result, those extensive researches have established a mature understanding for electroporation stage.

Many previous studies have shown that, adjusting pulsing parameters, including field strength^{28,40–46}, pulse duration^{38,41,44,47}, number of pulses^{15,48,49}, and pulse shape^{50–54} have changed the degree of permeabilization. Understanding the effect of these parameters provided an optimization path, particularly for reversible EP protocol where a high viability ratio was required. The major drawback of the EP is the death of a significant portion of the cell

population due to high voltage application. To overcome this limitation, among various techniques, a combination of a short-duration high-field strength pulse with a longer-duration lower-field strength pulse can increase the EP efficiency and preserve more cells alive^{15–29}. This method will be discussed in more detail in a separate section.

3.1.1.2. Electrotransportation of the target molecules

Electrotransportation is another important aspect of EP phenomenon. Many experimental works provided a variety of knowledge about molecular uptake. However due to its complexity, a comprehensive understanding of transport mechanism is still under investigation. It has been shown that molecular delivery strongly depends on the type or size of the target molecule^{19,73,74}. Besides, this mechanism not only depends on the electrophoresis, but also involves different mechanisms depending on the target molecule. For instance, the transport of small molecules ($MW < 4$ kDa) involves both dynamic diffusion and electrophoresis⁷⁵. This process can be modeled by the Nernst-Planck (NP) equation³⁹. On the other hand, the transport of large molecules ($MW > 4$ kDa) such as DNA involves endocytosis, DNA-membrane interaction, electrophoresis, and maybe more unknown mechanisms^{76,77}. Thus, transport of large molecules requires more work to have a full understanding. Based on the current knowledge, it has been recognized that the main molecular uptake of moderate and large molecules occurs through electrophoresis^{15,20,28,38,39}. Therefore, prolonging the applied pulse duration, increases the delivery amount significantly^{78,79}. In fact, our previous colleague found a linear relation between the delivery amount and the duration of the pulse¹⁹. However, longer pulse durations decreases the viability ratio, and causes unfixable damages on the cell membrane. We believe that many of the cell death happens due to over-poration of the membrane, which subsequently causes rupturing of the membrane or losing the integrity of the cell. To overcome this limitation,

permeabilization and delivery should be separated, and different pulsing parameters should be applied. For example, a high degree of permeabilization can be achieved by a strong pulse in very short time, while delivery can be persisted by a weaker and longer-duration pulse. Indeed, this procedure (two-pulse EP) has been used by many researchers. However, the effect of pulsing parameters has not understood completely due to ambiguity of presented works.

3.1.2. Two-pulse Electroporation protocol

As stated before, the EP phenomenon consists of two main parts (permeabilization and molecular-transport), and they are determined by the electrical parameters of applied field although different physical mechanisms are involved for both. Indeed, permeabilization and delivery require different kinds of pulse parameters, for example, to permeabilize the membrane the critical transmembrane potential threshold must be exceeded, where in some cases (particularly for larger molecules), this threshold might be higher. On the other hand, for delivery, longer pulse duration is required instead of a stronger pulse^{78,79}. To resolve this contradiction, EP pulse is split into two different pulses which are a short-duration high-field strength pulse for permeabilization and a longer-duration lower-field strength pulse for delivery (denoted by 'HV' and 'LV', respectively)¹⁵⁻²⁹. In this two-pulse procedure, permeabilization and delivery are considered to be separate task, with the first HV pulse inducing a high level of permeabilization, followed by a second LV pulse that increases the delivery amount due to electrophoresis. Many researchers have studied the pulsing parameters such as first pulse's (FP) field strength^{18,20,28}, the second pulse's (SP) field strength and duration^{15,16,18,19,21}, and delay between pulses^{15-18,29,79}, in order to better understand the fundamentals of two-pulse EP and optimize transfection efficiency.

Those studies showed that the efficiency of the multi-pulse EP delivery is strongly depended on the pulsing parameters. For instance, tuning the FP field strength and duration varied the EP efficiency drastically. As expectedly, increasing the field strength and duration of the FP increased the molecular delivery efficiency until a critical point, where too high field strength or too long duration of the FP decreased the EP efficiency due to low viability ratio^{18,20,28}. In order to maintain high viability, Cukjati *et al.* developed an algorithm that monitors the current-voltage responses in real-time and adjusts the field strength of the FP, however this algorithm does not provide a desired level of permeabilization for delivering different sized-molecules since the size of electro-pore cannot be measured²⁸. In addition to the FP, the effect of the SP field strength and duration have also been studied^{15,16,18,19,21}. In particular, a recent study has examined the scaling behavior of two-pulse delivery and viability by varying the field strength and duration of the SP ($E_2 = 0.1 - 1$ kV/cm, $t_2 = 10 - 100$ ms)¹⁹. That study found a linear relation between the delivery and the duration of the SP and an inverse linear correlation between viability and electrical energy, allowed simultaneous optimization of delivery and viability. However, that work focused on the SP parameters, and did not study other pulsing parameters such as the delay between pulses. Lastly, another parameter, the delay time between two pulses has been also studied in order to understand DNA-membrane interaction mechanisms^{16-18,29} or resealing mechanism^{15,16,79}. In most of those works, delay time effect on molecular delivery has not been studied quantitatively, few works have performed a systematic study that delay time ranges from milliseconds to hundreds of seconds. However, the effect of the delay time has not been understood fully due to controversial results. For example, an earlier work by Sukharev *et al.* showed that the transfection efficiency was decreased when the delay between pulses was increased¹⁵, while Satkauskas *et al.* showed that an optimum transfection has been reached at between 0.3 to 100s

delay time¹⁶. Additionally, most of those works have studied on electrotransfection of genes which involves gene-membrane complex formation, thus the amount of the delivery was not solely depended on electrophoresis and hard to quantify accurately. Furthermore, most of those studies on multi-pulse EP have focused on direct-current (DC) fields only, thus permeabilization and delivery have not studied separately due to electrophoretic drift of the DC pulses. As shown in many studies^{15,17,19,20,22,27}, the HV pulse alone can transport a considerable amount of the target molecule, confounding permeabilization and delivery. To overcome this limitation, we use an alternating current (AC) electric field for the FP coupled with a DC SP to achieve a clear separation of permeabilization and delivery.

3.1.3. Statement of Objectives

This thesis investigates the effect of the FP field strength and delay time between two pulses on EP mediated molecular delivery. Additionally, the effect of molecular size in the transport mechanism is also studied by using different-sized Fluorescein-Dextran (FD) conjugates (a non-binding chain polymer), with molecular weights of around 10 kDa and 70 kDa. Due to its non-binding nature and similar size range, dextrans can be more correlated with RNA or peptides in terms of electrophoretic transport and total permeabilized area on the membrane³⁸. It is also shown that the transport of mid-sized molecules is directly correlated with the state of permeabilization¹⁹ which avoids the complexity induced by the dynamic diffusive process associated with smaller molecules. The specific objectives of this work are to:

- Separate permeabilization and delivery clearly by employing a high-frequency AC FP with a DC SP.

- Demonstrate the effect of the degree of permeabilization on molecular transport by varying the field strength of the FP.
- Compare the electro-pore sizes obtained by different field strength by delivering different-sized target molecules.
- Study the effect of the delay times between pulses systematically by ranging delay times from milliseconds to hundred seconds.

Distinctly, we employed an AC field FP to achieve a clear separation of permeabilization and delivery, thus that allows to analyze each mechanism separately. Additionally, taking advantage of non-binding mid-sized FD we can directly correlate the delivery with the degree of permeabilization and on top of that different-sized molecules allows us to investigate the size of electro-pores. Finally, our pulse design provides us to probe the resealing dynamics of the cell membrane systemically.

3.2. Materials and Methods

A series of two-pulse EP experiments were performed on 3T3 mouse fibroblast cells, with an alternating-current first pulse to permeabilize the cell, followed by a direct-current second pulse to electrophoretically deliver the target molecule into the cell.

3.2.1. Cell Culture

NIH 3T3 mouse fibroblast cells were used throughout the experiments and cultured in Dulbecco's Modified Eagle Medium (DMEM) supplemented with 10% Fetal Bovine Serum (FBS), 1% Penicillin-Streptomycin, and 1% L-Glutamine (Sigma-Aldrich, St. Louis, MO) and incubated at 37°C and 5% CO₂. The reason for choosing this 3T3 cell line is because they are easy to culture and well suited for transfection studies⁸⁰. Approximately 3×10^6 cells were trypsinized at 70-80% confluency with 0.5% trypsin/EDTA (Sigma-Aldrich) followed by centrifugation for 2 minutes at 2000 rpm (Allegra X-21, Beckman Coulter, Brea, CA) in culture media, and then twice in electroporation buffer containing 0.4 mM MgCl₂, 250 mM sucrose, and 10 mM HEPES (Sigma-Aldrich) (pH 7.4). It is noted that, the optimum confluency of the cell population is usually reached after three days of the cell passage. The osmolarity and electrical conductivity are measured with osmometer (3D3 Osmometer, Advanced Instruments, Norwood, MA) and conductivity meter (CON 6, Oakton Instruments, Vernon Hills, IL), and adjusted to 310 mOsm/kg and 100 μ S/cm, respectively. The osmolarity is kept almost the same with the intra-cellular osmolarity in order to avoid swelling after EP. It is also shown that lower extra-cellular electrical conductivities increased the delivery. This physiological effect which called FASS is well explained in the Sadik *et al.*⁵⁸.

3.2.2. Electroporation Setup

The cell suspension was subjected to electric pulses in an EP cuvette with a 1-mm electrodes gap (VWR, Radnor, PA) at room temperature (20°C) under a sterile hood. Electric pulses were generated by a function generator (Tektronix AFG3022C, Melrose, MA) and amplified by a high-frequency, high-voltage amplifier (Trek Model PZD 350, Lockport, New York, NY) (Figure 3.1a). Applied pulses were measured by oscilloscope (PicoScope 5203, Cambridgeshire, UK). It is experienced that, attaching the oscilloscope directly to cuvette-electroporator with an 10X attenuated probe provides more accurate measurements instead of monitoring from the amplifier outlet. Figure 3.1a shows connection order of the electronic devices schematically. In Figure 3.1b, an example of generated AC + Delay time + DC pulse shape is shown.

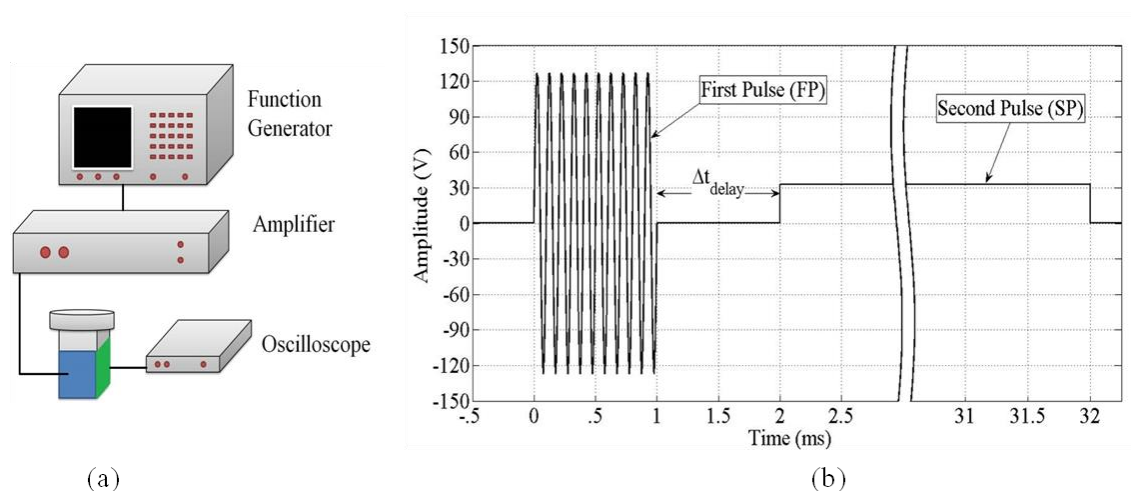


Figure 3.1 Schematic of (a) the experimental setup and (b) AC first (FP) and DC second (SP) pulses applied to the cells with a specified delay.

3.2.3. Electroporation Procedure

The cells were suspended in the EP buffer including 100 μM of Fluorescein-Dextran (FD) (Life Technologies, Grand Island, NY) and kept in the ice for 5 to 15 minutes before

applying pulses. Two different FD conjugates with a molecular weight of around 10 kDa and 70 kDa were utilized to measure delivery. In most of the experiments, two consecutive different pulse were applied to the cells; an AC first pulse (FP) for cell permeabilization and a DC second pulse (SP) with some delay for FD delivery (Figure 3.1b). The pulse parameters (shape, strength and duration) are given in Table 3-1. For each experiment, control cases were also studied in which cells were treated to every step of experiment, but without exposure to the electroporation pulses. The delay times (Δt_{delay}) between two pulses were arranged by the function generator's Trigger Delay option between two channels and precise delays ranging from no delay to milliseconds to seconds were obtained. Delay times longer than 80 seconds (such as 100 s and 300 s delays) were timed with a stopwatch and applied manually. Immediately after pulsation, culture media was added to the cell suspension and incubated for 30 minutes to allow for resealing. Then, the cell suspension was transferred to phosphate buffer saline without Mg^{2+} and Ca^{2+} (PBS) (Sigma-Aldrich) containing 2 μM of 7-Aminoactinomycin D (7-AAD) (MW = 1270.43 Da) (Life Technologies) solution in order to determine viability (53) and waited for 15-20 minutes. 7-AAD, which is used for staining nucleic acids, is a cell-membrane-impermeant dye. However, the cells that were not able to recover and reseal after pulsation do uptake 7-AAD which fluoresces upon binding to nucleic acids. Thus, cells which allowed 7-AAD entry after 30 minutes were considered to be dead cells. The cell suspension was washed twice with PBS in order to remove free FD and unbounded 7-AAD before fluorescence imaging. All experiments were repeated at least 3 times for consistency, and for each experimental condition at least 100 cells were analyzed.

Table 3-1 Applied pulse parameters for the first and second pulse

	First Pulse (FP)	Second Pulse (SP)
Shape	AC Sinusoidal ($f = 1 - 500$ kHz)	DC
E. Field Strength	$E_1 = 0.60 - 0.90$ kV/cm	$E_2 = 0.33$ kV/cm
Duration	$t_1 = 1$ ms	$t_2 = 30$ ms
Delay between FP and SP	0 - 300 s	

3.2.4. Fluorescence Imaging Microscopy

Both FD and 7-AAD fluorescence signals were acquired using fluorescence-imaging microscopy. The cell images were taken by a high-sensitivity camera (pco.edge sCMOS, PCO AG, Kelheim, Germany) attached to an inverted microscope (Olympus IX71, Center Valley, PA) with a 20x objective. Approximately 20 μ L of cell solution was dropped between two cover slip was placed on top of motorized stage. The cell solution was sandwiched between two cover slip solution in order to obtain standard thickness (approximate cell diameter: 15 μ m) and avoid cell motion due to flow. A high intensity discharged mercury vapor lamp is used as an illumination source for imaging. That UV light is filtered by a triple-band excitation filter (DAPI - FITC - TRITC) and exposed to the cell solution. Then using the appropriate emission filter, the signal of the fluorophore is captured by camera. The cell images were taken with two different fluorescent channels (for FD ex: 494nm, em: 521nm, for 7-AAD ex: 488nm, em: 647nm). Additionally, one bright field image was also taken to detect the cell diameter and center coordinates for image processing. The cell solution was controlled by a motorized stage and programmed to take a series a patterned image. The fluorescence light's shutter was

controlled manually and elaborated to avoid photo-bleaching. Figure 3.2 shows the working principles of the fluorescence imaging technique schematically.

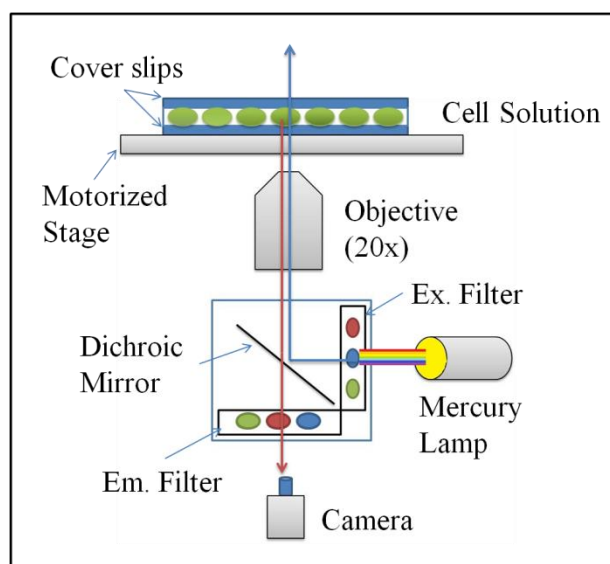


Figure 3.2 A schematic of working principle of fluorescence imaging. A high-intensity UV light which is provided by a mercury lamp, is filtered by triple band pass (DAPI - FITC - TRITC) filter and images are acquired by a high-sensitivity camera.

3.2.5. Image Processing and Data Analyzing

Figure 3.3a shows an exemplary set of images which were taken in the bright-field, FD-fluorescence, and 7-AAD-fluorescence channels, from the top to bottom rows respectively. All images and data were analyzed with MATLAB (The MathWorks, Natick, MA). The code is given in Appendix A. The bright-field images (Figure 3.3a) were used to compute a disk-shaped profile for each cell and detect the cell's center coordinates and diameter. Fluorescence intensity per volume for each cell is calculated by integrating the signal within the disk shape area and normalized by the cell volume. Then the background noise that calculated from a control (no-pulse) case was subtracted from the other cases. This was done for both the FD channel and 7-AAD channel to determine the fluorescence intensities for each individual cell.

The scatter plot shown in Figure 3.3b has FD intensity per volume (corresponding to the degree of delivery) as its abscissa, and 7-AAD intensity per volume (related to the viability of the cell) as its ordinate. As previously mentioned, 7-AAD was used to detect dead cells, and the cells that were above the viability line were presumed to be non-viable. The level of the viability line was determined by 7-AAD intensities two standard deviations above the mean fluorescence intensity. For analysis of the delivery of FD, only alive cells were considered. Throughout the experiments, viability was above 80% in many cases and always exceeded 60%.

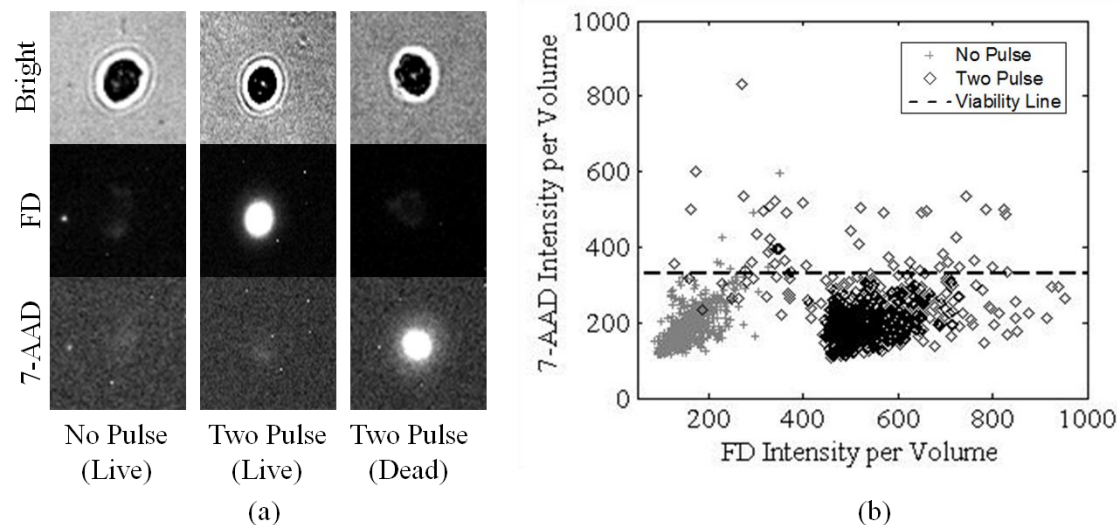


Figure 3.3 Examples of (a) cell images taken for image processing (the contrast of these images has been adjusted for display purposes only), and (b) scatter plot showing FD and 7-AAD intensities per volume in a representative set of analyzed images.

3.2.6. Confirming and Calibration of the Fluorescence Imaging Method

The fluorescence-imaging method was compared to flow-cytometry data from previous work on two-pulse DC EP¹⁹. For the same conditions ($E_1 = 1$ kV/cm, $t_1 = 1$ ms and $E_2 = 0.1 - 0.8$ kV/cm, $t_2 = 30$ ms), the fluorescence-imaging results were consistent with the prior data.

A calibration experiment was performed to correlate the fluorescence intensity measured in EP-mediated molecular delivery experiments with the concentration of the delivered molecules. We designed an array of rectangular micro-chambers with 20 μm height using double-sided adhesive tape (Nitto Denko America Inc, Teaneck, NJ) as a spacer between two cover slips (VWR). Serial dilutions of FD in electroporation buffer ranging between 0.312 - 50.0 μM were imaged at room temperature to generate calibration curves of FD intensity versus concentration for both 10 kDa and 70 kDa FD conjugates. All the measurements have been performed 3-4 times for each case to obtain consistent results.

Figure 3.4 shows the fluorescence intensity per volume for both 10 kDa and 70 kDa FD concentration. A linear correlation was observed for both 10 kDa and 70 kDa FD in the concentration range analyzed in this study. The cell fluorescence intensity per volume was then converted to the concentration using the calibration curves. Such calibration experiments have been performed by other investigators, see e.g.³⁸.

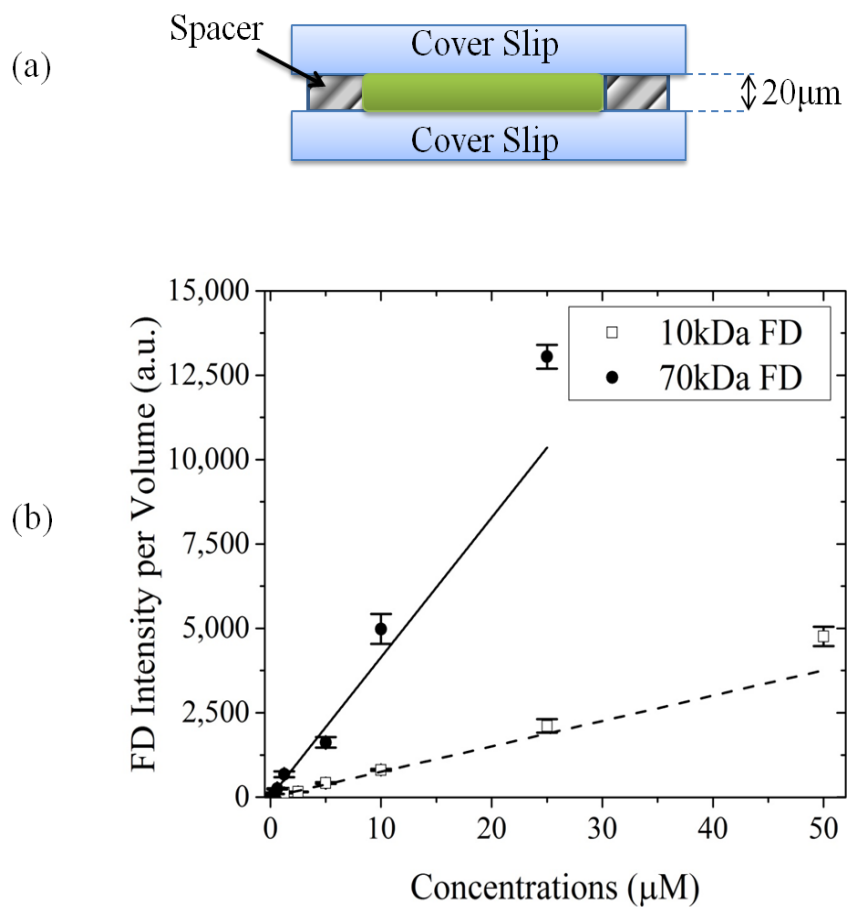


Figure 3.4 Calibration experiment, (a) the schematic of placing different-diluted FD solutions. The gap between cover slips is fixed by using double-sided adhesive tape. (b) The fluorescence intensity versus concentration for FD 10k and FD 70k conjugates.

3.3. Results

Experimental results are presented. Although, the main scope of this study is on the two-pulse EP method, two different set of single-pulse experiments are conducted to determine initial pulsing parameters. Later, two-pulse EP experimental results are presented in two main categories depending on the delay time between the two pulses: (I) no delay, and (II) various delay times ranging from 1 ms to 300 s.

3.3.1. Single AC Pulse Application

In the two-pulse EP procedure, although the FP is considered in many studies to only permeabilize the cell membrane, a considerable amount of molecular delivery can occur due to electrophoretic effects of the DC FP that is typically used^{15,17,19,20,22,27}. As seen in Figure 3.5, after a single DC pulse ($E_1=0.90$ kV/cm, $t_1=1$ ms), a significant amount of 10 kDa FD is delivered into the cell. On the other hand, an AC pulse greatly reduces 10 kDa FD delivery. The lack of delivery at the end of the AC pulse is due to non-binding nature of FD molecules, since electrophoretically-driven FD molecules may enter the cells during the pulsation, but also leave the cell due to alternating polarity of AC field. Increasing the frequency of the AC field further reduces 10 kDa FD delivery. Here, the 10 kHz AC FP was judged to have negligible (<10%) delivery compared to that of the two-pulse case with no delay. Therefore, to clearly separate permeabilization from delivery, we employed a 10 kHz AC FP with $E_1=0.90$ kV/cm and $t_1=1$ ms.

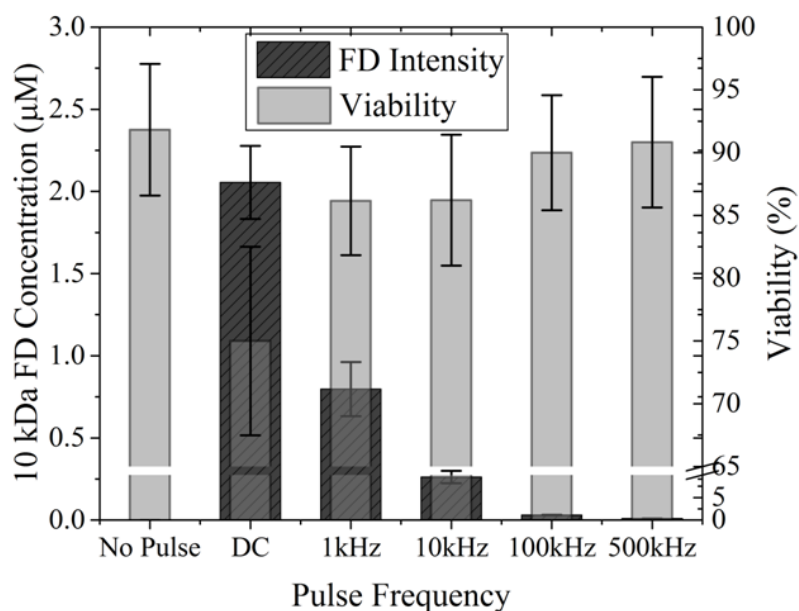


Figure 3.5 Intracellular 10 kDa concentrations and viability for different-frequency AC fields (1 ms, 0.9 kV/cm) compared to a DC field of the same strength.

3.3.2. Single DC Pulse Application

In order to determine the field strength of the SP, we first applied 30-ms-long single DC pulses with different field strengths. As seen in Figure 3.6 there is a slight 10 kDa FD uptake (around 0.25 μM) beginning at 0.40 kV/cm. This is presumably the threshold DC field strength which would begin to permeabilize the 3T3 cells for 10 kDa FD in our experiments. Since the objectives of this work were to study the effect of FP-to-SP delay time on membrane resealing and molecular delivery, we wanted the SP not to create new pores, but only to hold the electropores open and provide the electrophoretic force for delivery. Therefore, the SP's field strength was chosen to be 0.33 kV/cm, lower than threshold required for significant electroporation and delivery by a single DC pulse and both SP field strength and duration are kept fixed ($E_2=0.33$ kV/cm, $t_2= 30$ ms) for all cases. In this way, we can isolate the effect of

the FP and correlate the amount of delivery obtained after the SP with the permeabilization level of the membrane achieved by the FP.

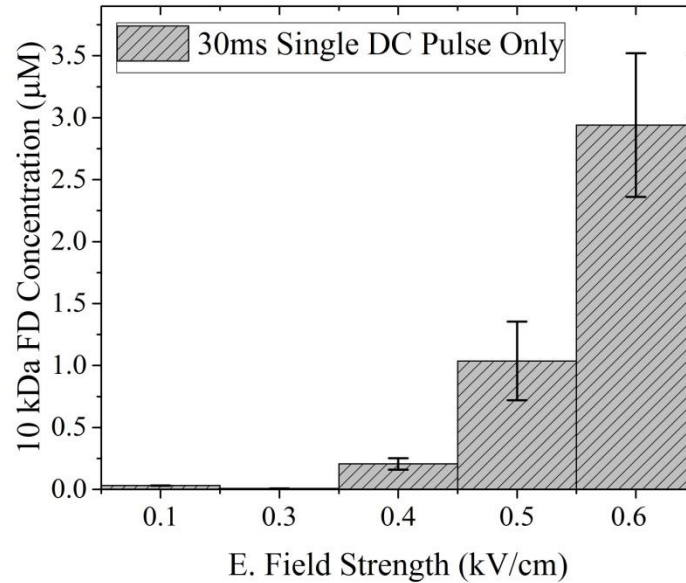


Figure 3.6 Delivered intracellular concentration for a single 30-ms-long DC pulse of different field strengths.

3.3.3. Two-Pulse Application with No Delay

We first consider a two-pulse protocol consisting of an AC FP (10 kHz, $E_1=0.9$ kV/cm, $t_1=1$ ms) immediately followed by a DC SP. The weak DC SP by itself is not of sufficient strength to cause adequate EP for 10 kDa FD. Figure 3.7 shows the delivered intracellular FD concentration for the FP-only and two-pulse cases. It can be seen that applying the FP only does not cause any significant FD delivery, and the intra-cellular concentration remains almost the same in spite of increasing FP field strength or changing molecule size. However, applying the DC SP ($E_2=0.33$ kV/cm, $t_2=30$ ms) with no-delay achieves a relatively high molecular delivery ranging from 1 μ M to 4 μ M for the 10 kDa FD (Figure 3.7). Hence a clear separation of permeabilization and delivery is obtained by using an AC FP followed by a

DC SP. Moreover, the two-pulse protocol delivers FD with viabilities exceeding 70% in the 10 kDa case.

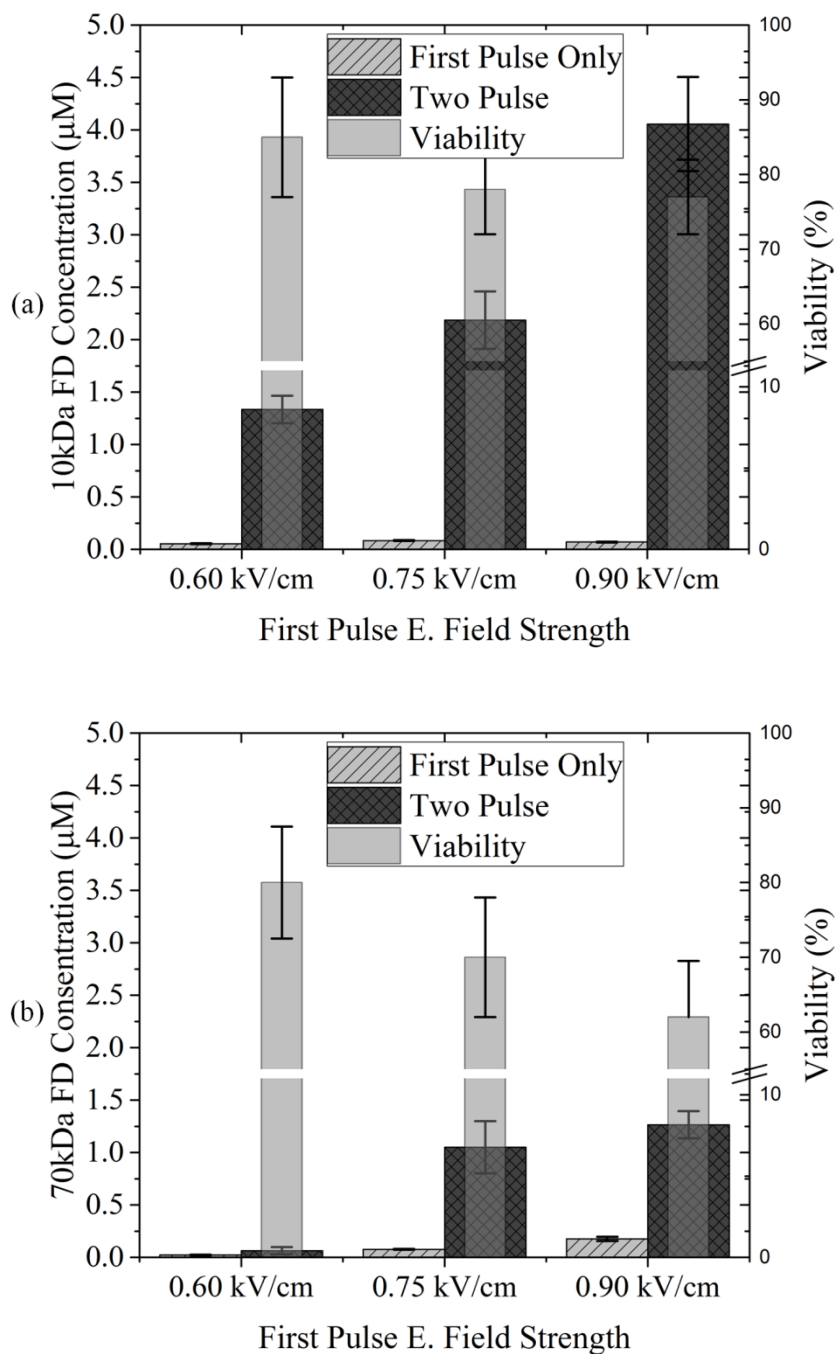


Figure 3.7 Delivered intra-cellular FD concentrations and viability for different AC FP strengths and molecule sizes: (a) 10 kDa FD and (b) 70 kDa FD.

Having achieved a clear separation of permeabilization and delivery, we next examine the degree of permeabilization by applying FPs of different field strengths ($E_1 = 0.6 - 0.9$ kV/cm, $t_1 = 1$ ms). As seen in Figure 3.7 the different columns of, different FP strengths between 0.6 kV/cm to 0.9 kV/cm result in very different FD-delivery levels when followed by the same SP. As expected, increasing the field strength of the FP increases intra-cellular FD concentration, presumably due to increased permeabilization of the cell membrane. This result shows the importance of the FP in the two-pulse EP protocol, since the final delivery amounts strongly depends on the FP field strength, even though the FP itself achieves negligible delivery.

We next investigated the effect of molecular size on the delivery achieved by two-pulse EP. Comparing Figure 3.7a with Figure 3.7b, we see that delivered intra-cellular concentrations of two different-sized FD molecule (10 kDa and 70 kDa) are very different under the same conditions. For example, with a 0.6 kV/cm FP immediately followed by a SP ($E_2 = 0.33$ kV/cm, $t_2 = 30$ ms), there is considerable delivery of 10 kDa FD (around $1.25 \mu\text{M}$). However, with the same pulsing parameters, there is negligible intra-cellular delivery of 70 kDa FD. This suggests that pores formed by the 0.6 kV/cm FP have a pore-size distribution that allows 10 kDa FD molecules to pass through, but very few 70 kDa FD molecules. We interpret this to mean that the size distribution of electroporated pores shifts to larger pores with higher FP field strength. Finally, with a 0.9 kV/cm-field-strength FP, the delivery of 10 kDa FD is almost doubled over that of the 0.75 kV/cm case, while the 70 kDa delivery increases slightly. This difference shows that increase in the formation of larger electropores is less than of smaller electropores in the jump in FP strength from 0.75 to 0.9 kV/cm. The data clearly indicate that pulsing parameters (in particular the FP strength) need to be adjusted for target-molecule size.

Summarizing briefly, our results without delay between the pulses indicate that the FP is instrumental in creating adequate permeabilization to facilitate the transport of the molecules via the SP, although the FP by itself effects negligible delivery by design.

3.3.4. Two-Pulse Application with Variable Delay

In reversible EP, electropores eventually disappear and the cell membrane reseals to return to its preshock state post-pulsation. In other words, the cell membrane becomes impermeable for foreign molecules long enough post-pulsation. This resealing stage of reversible EP typically takes longer than permeabilization, e.g. electroporeabilization can occur in micro or nano-seconds with suitable pulsation, while the disappearance of the electropores has been reported to take seconds or minutes^{81,82}. If long resealing times hold, post-pulsation delivery can be of significance for transfection efficiency, particularly for small molecules of high diffusivity. We took advantage of the separation between permeabilization and delivery offered by our AC+DC two-pulse protocol design to study transport dynamics by delaying the SP by times ranging from 1 ms to 300 s. The total delivery of the two sizes of FD could be measured to infer the permeability of the membrane to the target molecules after various delay times of the SP. Figure 3.8 shows the measured intra-cellular FD concentrations shown versus the delay times between pulses for 10 kDa and 70 kDa FD. It can be seen that there is a nearly 50% drop in the FD concentration with 100 ms delay between first and second pulses due to resealing for most of the cases. However, (reduced) delivery persists even when the SP is delayed by up to hundreds of seconds. (Recall that the SP by itself is too weak to permeabilize and deliver.) Furthermore, comparing the data in Figure 3.8a, for different intensity FPs, we see that the rate of delivery decrease with delay times actually depends on

the field strength of the FP. For the 0.6 kV/cm FP, negligible 10 kDa FD delivery is obtained after around 100 s of delay between the pulses, but for the 0.75 and 0.9 kV/cm FPs, complete cessation of delivery by the SP only occurs after delays of thousands seconds. Additionally, the slopes of fitted line are also different for different permeabilization degrees (particularly for 10 kDa cases). The change in delivered intracellular concentration (and by inference the resealing rate) is higher in the highly permeabilized cases. This suggests that the resealing dynamics are directly related with the permeabilization degree, and that although a complete resealing takes minutes, a significant portion of resealing happens in very short time post-pulsation.

In Figure 3.8, it can be clearly seen that the delivery of both 10 kDa and 70 kDa FD decreases nearly linearly with the logarithm of the delay time regardless of the molecule size. Although, comparing Figure 3.8a and b, for instance, at 0.75 kV/cm FP case, very little 70 kDa FD is delivered after SP delays of 100 s or 300 s, the smaller 10 kDa molecule continues to be delivered after similar delay times. This suggests that even at the same permeabilization level, the exclusion times where the electropores are impermeable for the target molecule may vary depending on the molecule size. According to our experimental conditions, in general, this exclusion time for the 70 kDa FD is around 100-300 s, and for the smaller 10 kDa FD the exclusion time is predicted to be more than thousand seconds depending on the FP strength. It can be also interpreted as that the electropores allowing entry of 10 kDa FD (but not 70 kDa FD) persist for time gaps on the order of 100 s between the FP and SP. In addition to that, the intra-cellular concentration decrease-rates (inferred to resealing-rates) vary strongly with FP strength for 10 kDa FD but not for 70 kDa FD, as seen in Figure 3.8b. The 10 kDa case (Figure 3.8a) shows that the variation of intracellular concentration with the delay time has different slopes depending on the strength of the FP. However, for the 70 kDa FD case,

the 0.75 and 0.9 kV/cm FP lines have almost the same slope. This shows that the EP-mediated molecular transport for the different-sized target molecules has different dynamic depending on the current permeabilization state.

Briefly, our results with various delay times between the pulses indicate that, the resealing time of the membrane strongly depends on the permeabilization degree, and a significant drop in the delivery occurs within very short time due to resealing process. Additionally, the transport dynamic of different-sized molecules varies, however the decrease of the intra-cellular concentration with respect to delay times has a linear logarithmic behavior regardless of the target molecule size.

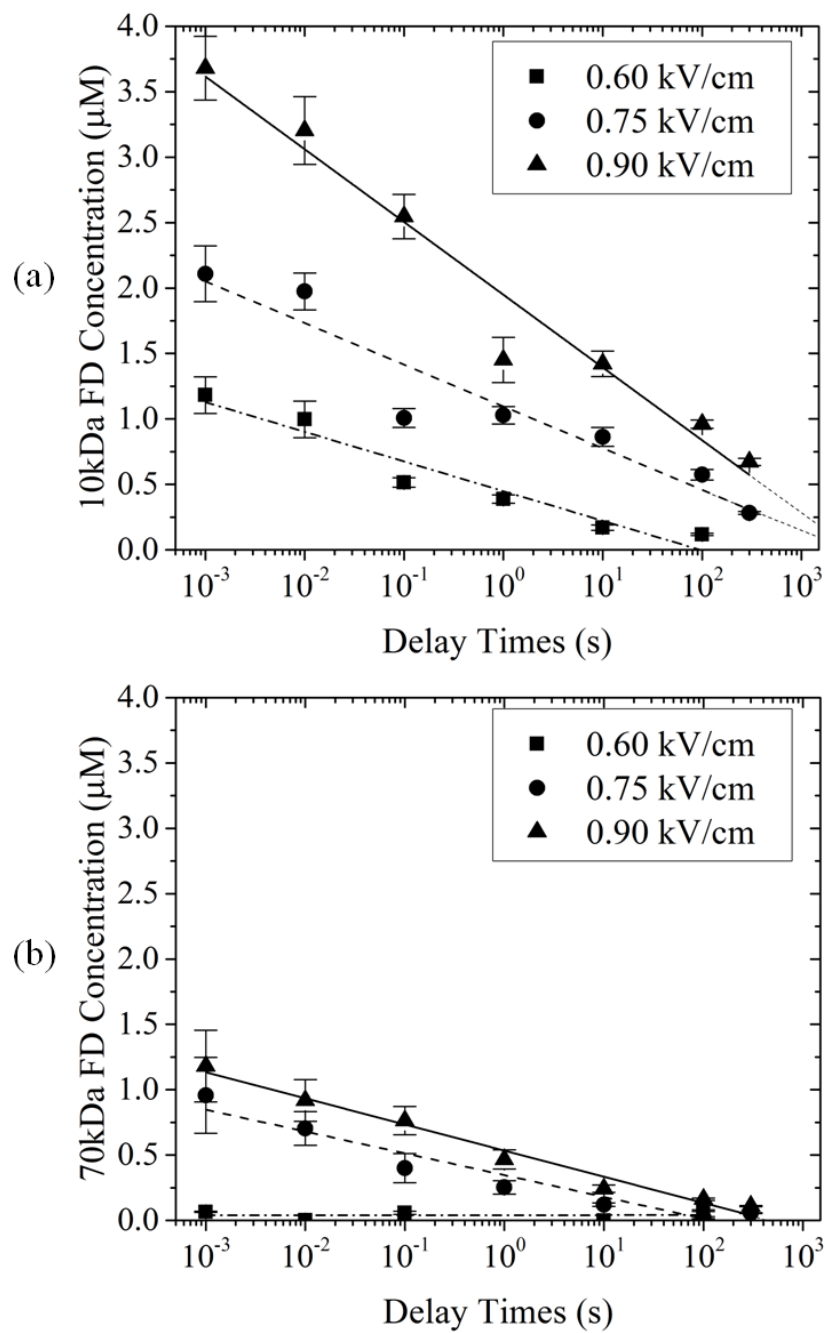


Figure 3.8 Delivered intra-cellular FD concentrations with different delay times ranging from 1 ms to 300 s for different AC FP strengths and molecule sizes: (a) 10 kDa FD and (b) 70 kDa FD.

3.4. Discussion

Experimentally, two techniques have been commonly used to determine the degree of cell-membrane permeabilization by electric pulses: (I) measuring the conductance or current change across the cell^{28,47,83–86}, and (II) measuring the transport of marked molecules. For quantifying the size of pores, the second method is more attractive because different-sized molecules can be used³⁸. However, this method is somewhat restricted in that it must deliver a sufficient amount of target molecule in order to acquire signal, *i.e.*, it is actually sensitive to delivery and not permeabilization^{43,45,87}. Therefore, membrane permeabilization is traditionally considered in tandem with molecular delivery, although the two phenomena are distinct and involve different physical mechanisms. In this work, we performed two-pulse EP using a 10 kHz AC-field FP, which was shown to permeabilize the membrane with minimal net electrophoretic delivery of FD and a 0.33 kV/cm field strength of DC SP, which was also shown not to permeabilize the membrane itself but to provide electrophoretic force for the delivery. By this means, we were able to probe the degree of permeabilization according to delivery amount after the SP.

It is shown that in two-pulse EP protocol, the FP affects the delivery amount obtained after the SP crucially. Our results, which showed that increasing the AC FP field strength increases the degree of permeabilization, are in agreement with previous studies^{18,20,23,26,28}. In those studies, EP efficiency increased with the FP strength until a critical point where the efficiency started to decrease due to low viability. Knowing that fact, in our study, further high field strengths have not been applied for the FP, since the viability ratios were aimed to maintain above 60% throughout the experiments. Distinctively, we have used two different-sized FD molecules (10 kDa and 70 kDa) which had provided us to infer the distribution of electropore size and number for different degree of permeabilization. By using different-sized

molecules, Saulis *et al.* was performed a study in order to investigate the size of electropores that created by different pulsing parameters⁴⁵. However, those target molecules were small molecules (MW < 4 kDa), thus, besides electrophoresis, the dynamic diffusive effect was also involved in transport mechanism. Therefore we have used a mid-sized FD molecules weighted 10 kDa and 70 kDa in order to avoid diffusive process and to have a similar size range with RNA or peptides and more accurate quantification of delivery which directly correlated with the permeabilization level were obtained^{19,38}. Additionally, by taking advantage of non-binding nature of the FD molecules, a clear separation of permeabilization and delivery was achieved and the complexities in transport mechanism such as DNA-membrane interactions were avoided.

In this work, it is seen that the transport of large molecules (70 kDa) requires stronger FP field strength in order to obtain a significant delivery. One of the few studies that focused on the formation and distribution of electropores as a model study by Krassowska and Filev *et al.* explained the theoretical background of this behavior⁷². In their model, increasing the field strength extended the pore size and increased the number of pores, but the formation rate of large pores was slower than the formation of the small pores. Therefore, when comparing a highly and a moderately permeabilized cells, it is possible that the number of large pores would be nearly equal, while the number of small pores would be much higher in the highly permeabilized cell. Our results are consistent with the predicted evolution of size distribution of the electropores with field strength, showing delivery of 70 kDa FD at a FP strength of 0.75 kV/cm, while no delivery was observed for 0.60 kV/cm. That shows the size of electropores is extended with increasing the field strength. Furthermore, when the FP strength is further increased from 0.75 kV/cm to 0.90 kV/cm, the delivery increment for 10 kDa FD was higher than for the 70 kDa molecule. In light of these findings, we can speculate

that delivery of large molecules, such as transport of gene or big-sized drugs or proteins, requires stronger pulse strength while a slightly above the critical permeabilization threshold pulse strength may have a better efficiency than a higher electric field strength, since almost the same amount of delivery will be achieved with higher viability ratio. However, the optimum electric-field strength is likely to be cell and molecule dependent.

Another important stage for reversible electroporation is the resealing or disappearance of the electropores^{11,14,81,88}. Incomplete resealing is an indicator of cell mortality since dead cells cannot recover from their leaky state. Numerous researchers have measured membrane resealing times using various methods, with results ranging from milliseconds to minutes. Membrane-resealing times inferred from measuring the membrane conductance^{36,47,86,89} tend to be shorter (short-term resealing) than the times suggested by uptake of small^{13,44,45,90–92} or larger molecules^{93,94} after pulsation (long-term resealing). For instance, Hibino *et al.* showed one of the first sub-second methods using voltage-sensitive membrane dye³⁶, and later on H. He *et al.* and Khine *et al.* developed two sub-second methods to measure resealing times. All concluded that membrane resealing occurred on timescales on the order of milliseconds^{47,86}. In other studies, a test molecule was added to the cell solution at different time post-pulsation, and the exclusion times of the target molecule was correlated with resealing. This method provides an actual resealing time, but, due to the difficulty in precisely controlling the addition of the test molecule for very short times, measurement of the resealing dynamics at the sub-second level is impossible. Our current work takes advantage of a two-pulse protocol with an AC permeabilization FP followed by a DC delivery pulse to probe membrane resealing over a wide range of timescales. A similar delayed SP method was used by Sukharev *et al.* earlier to probe the interaction of DNA with electropores¹⁵. It was observed that the transfection efficiency decreased with increasing of the delay time which is

consistent with our results. However, distinct from that work, our studies utilize an AC FP, and varied the strength of FP¹⁵. This variation of the FP strength, in other words, variation of the degree of permeabilization, yielded us information that resealing rates depend on the FP. As shown in Figure 3.8a, with 0.9 kV/cm FP case resealing-rate is faster than the others. As stated above, highly permeabilized cells have higher number of small pores, and as expectedly small pores reseals faster while the large pores may cause some defects on the membrane. Thus, we can hypothesize that, electropores shrink rather quickly, but nano-sized pores or defects tend to remain for a much longer time. This also agrees with Krassowska and Filev *et al.*⁷² in their model, all pores shrunk to minimum-energy level pore size (around 0.8 nm) immediately after pulsation while they persisted until a complete resealing. These nano-sized pores or defects act as nucleation sites when the SP pulse is applied. Therefore, taking advantage of low energy barrier of nucleation sites for poration, the SP extends the pore sizes, although the SP itself is not enough for permeabilization. However, with the same FP and SP, but with different delay times the delivery amounts vary strongly. That means, although the SP extends the nano-sized pores, it cannot reoperate the resealed pores. Therefore, the decrease in the delivery with increasing delay time can be correlated with resealing dynamics of the electropores. The different exclusion times for 10 kDa and 70 kDa FD indicates the pore shrinking time, since between 100-300 s delay time pores shrink to exclude 70 kDa and then more than thousands seconds to exclude 10 kDa FD molecules depending on the FP strength.

In the previous studies, Andre *et al.*¹⁸ indicated that a delay time between pulses is necessary. They stated that with a HV FP cell membrane reaches a highly permeabilized state and then with a no-delay SP cell membrane overporates, and consequently lowers the viability and transfection efficiency. They claim that a delay time between pulses allow the cell membrane to recover from a highly permeabilized state, but electro-transfection can continue

due to slow resealing process. Therefore, taking advantage of the slow resealing process, a SP provides an electrophoretic force for delivery and increase the efficiency. Firstly, in that work, DNA electro-transfection was studied which involves DNA-membrane interaction mechanism besides electrophoresis, thus the effect of the delay time is not clear. Although for high field strength FP, a delay time between pulses might be helpful for the viability, but the total pore area shrinks significantly in short time period post-pulsation. Thus, the advantageous of the high permeabilization degree is forfeited. Additionally, it is also shown in our work that for delivering large-sized-molecules (like DNA, RNA, proteins, etc.), increasing the strength of the FP slightly increased the delivery efficiency, therefore a high strength FP is not necessary. In another work by Satkauskas *et al.*¹⁶ the effect of delay time between pulses is investigated ranging from 5 ms to 10,000 s and showed that an optimal efficiency reached between 0.3 - 100 s delay times. They claim that, even though a high permeabilization degree is achieved after the FP, the DNA solution needs more time for a better redistribution within the tissue. However, longer delay times (more than 300 s) decreases the transfection of DNA. Additionally, they emphasize the importance of a SP in order to increase transfection efficiency. Our results also agree with that work, since a great portion of delivery achieved after the SP and a long delay time decreased the transfection drastically. Contrary, we observed almost 50%-drop of the delivery within 100 ms delay. The reason behind this conflict might be due to the complexity of the DNA electro-transfection which involves DNA-membrane interaction or redistribution of the DNA solution within the tissue (as indicated in that work). In our study, by using non-binding FD, we have avoided these complexities and directly correlated the decrease of delivery with resealing process.

As previously seen in Figure 3.8, the total delivered intracellular concentration depends on the logarithm of the delay time regardless of the molecule size. In the many literature, the

delivery amounts decreased with long enough delay times^{15,16,79}, however, according to our knowledge, a logarithmic behavior have not been observed. We speculate this to mean that around 50% of resealing happened in the first 100 ms while complete resealing took hundreds of seconds. Although the physical mechanisms behind this behavior are not understood yet, these results suggesting resealing is both a short-term and long-term process may explain the enormous differences in the literature for membrane resealing times.

3.5. Conclusion

In this work, we have conducted a series of two-pulse electroporation experiments, focusing on delivery efficiency of two different-sized molecules using different pulsing parameters. Distinct work, we have employed an AC field FP to achieve a clear separation of permeabilization and delivery, and we have also varied the delay times between the AC FP and DC SP systematically. When the SP was kept at a fixed strength (chosen to be below the critical permeabilization threshold) and the FP field strength was varied, the delivery of 10 kDa and 70 kDa varied strongly. At lower field strengths of 0.6 kV/cm, membrane pores generated by the AC FP were sufficiently large to allow transport of 10 kDa FD, but not 70 kDa FD. Increasing AC FP field strength increases the size and number of electropores on the membrane, allowing delivery of the larger molecule. We further systematically studied the effect of delay times between pulses on the delivery efficiency. Using the AC FP to porate the membrane, and a DC SP for transport, we are able to probe resealing dynamics over timescales ranging from milliseconds to minutes. We find for these cells and pulsing parameters that the EP-mediated delivery scales with the logarithm of the delay time regardless of the molecule size and 50% of resealing happens in the first 100 ms after pulsation, however complete resealing takes hundreds of seconds. This result may harmonize the inconsistent membrane resealing times reported in the literature for different experiments.

First of all, this study demonstrated that molecular delivery of two-pulse EP decreases logarithmically with the delay time between pulses regardless of molecular size, where the physical foundation behind have not understood yet. Therefore, a more detailed study on this finding can be considered as a future work by delivering more different-sized target molecule and using different types of cells. In addition to that, this logarithmic behavior can be validated with another fluorescence analyzing method such as flow-cytometry. Furthermore, a clear

evidence for the fast shrinking after the pulsation could not be presented with our current experiment design. A new experimental procedure can be designed to probe the transport mechanism in shorter time scales.

3.6. References

1. Neumann, E., Schaefer-Ridder, M., Wang, Y. & Hofschneider, P. H. Gene transfer into mouse lyoma cells by electroporation in high electric fields. *EMBO J* **1**, 841–845 (1982).
2. Teissie, J. *et al.* Recent biotechnological developments of electropulsation. A prospective review. *Bioelectrochemistry* **55**, 107–112 (2002).
3. Heller, R., Shirley, S., Guo, S., Donate, A. & Heller, L. Electroporation based gene therapy—From the bench to the bedside. in *Engineering in Medicine and Biology Society, EMBC, 2011 Annual International Conference of the IEEE* 736–738 (IEEE, 2011).
4. Teissie, J. *et al.* Drug delivery by electropulsation: Recent developments in oncology. *International journal of pharmaceutics* **423**, 3–6 (2012).
5. Golzio, M., Rols, M. P. & Teissie, J. In vitro and in vivo electric field-mediated permeabilization, gene transfer, and expression. *Methods* **33**, 126–135 (2004).
6. Mir, L. M. *et al.* High-efficiency gene transfer into skeletal muscle mediated by electric pulses. *Proceedings of the National Academy of Sciences* **96**, 4262–4267 (1999).
7. Costa, M. *et al.* A method for genetic modification of human embryonic stem cells using electroporation. *Nature protocols* **2**, 792–796 (2007).
8. Miklavčič, D., Šemrov, D., Mekid, H. & Mir, L. M. A validated model of in vivo electric field distribution in tissues for electrochemotherapy and for DNA electrotransfer for gene therapy. *Biochimica et Biophysica Acta (BBA)-General Subjects* **1523**, 73–83 (2000).
9. Mir, L. M., Moller, P. H., André, F. & Gehl, J. Electric Pulse-Mediated Gene Delivery to Various Animal Tissues. *Advances in genetics* **54**, 83–114 (2005).
10. Neumann, E., Sowers, A. E. & Jordan, C. A. *Electroporation and electrofusion in cell biology*. (Springer, 1989).
11. Gehl, J. Electroporation: theory and methods, perspectives for drug delivery, gene therapy and research. *Acta Physiologica Scandinavica* **177**, 437–447 (2003).
12. Weaver, J. C. Electroporation theory. in *Animal Cell Electroporation and Electrofusion Protocols* 3–28 (Springer, 1995).
13. Neumann, E., Kakorin, S. & Toensing, K. Principles of membrane electroporation and transport of macromolecules. in *Electrochemotherapy, Electrogenotherapy, and Transdermal Drug Delivery* 1–35 (Springer, 2000).
14. André, F. & Mir, L. M. DNA electrotransfer: its principles and an updated review of its therapeutic applications. *Gene therapy* **11**, S33–S42 (2004).
15. Sukharev, S. I., Klenchin, V. A., Serov, S. M., Chernomordik, L. V. & YuA, C. Electroporation and electrophoretic DNA transfer into cells. The effect of DNA interaction with electropores. *Biophysical journal* **63**, 1320–1327 (1992).
16. Satkauskas, S. *et al.* Mechanisms of in vivo DNA electrotransfer: respective contributions of cell electropermeabilization and DNA electrophoresis. *Molecular Therapy* **5**, 133–140 (2002).
17. Pavlin, M., Flisar, K. & Kanduđer, M. The role of electrophoresis in gene electrotransfer. *The Journal of membrane biology* **236**, 75–79 (2010).
18. André, F. M. *et al.* Efficiency of high- and low-voltage pulse combinations for gene electrotransfer in muscle, liver, tumor, and skin. *Human gene therapy* **19**, 1261–1272 (2008).
19. Sadik, M. M. *et al.* Scaling Relationship and Optimization of Double-Pulse Electroporation. *Biophysical journal* **106**, 801–812 (2014).
20. Bureau, M. F., Gehl, J., Deleuze, V., Mir, L. M. & Scherman, D. Importance of association between permeabilization and electrophoretic forces for intramuscular DNA electrotransfer. *Biochim. Biophys. Acta* **1474**, 353–359 (2000).
21. Satkauskas, S. *et al.* Electrophoretic component of electric pulses determines the efficacy of in vivo DNA electrotransfer. *Hum. Gene Ther.* **16**, 1194–1201 (2005).
22. Kanduđer, M., Miklavčič, D. & Pavlin, M. Mechanisms involved in gene electrotransfer using high- and low-voltage pulses—an in vitro study. *Bioelectrochemistry* **74**, 265–271 (2009).
23. Heller, L. C. *et al.* Optimization of cutaneous electrically mediated plasmid DNA delivery using novel electrode. *Gene Ther.* **14**, 275–280 (2007).
24. Haberl, S. *et al.* Effect of different parameters used for in vitro gene electrotransfer on gene expression efficiency, cell viability and visualization of plasmid DNA at the membrane level. *J Gene Med* **15**, 169–181 (2013).
25. Pavselj, N. & Pr  at, V. DNA electrotransfer into the skin using a combination of one high- and one low-voltage pulse. *J Control Release* **106**, 407–415 (2005).

26. Yockell-Lelièvre, J., Riendeau, V., Gagnon, S. N., Garenc, C. & Audette, M. Efficient transfection of endothelial cells by a double-pulse electroporation method. *DNA Cell Biol.* **28**, 561–566 (2009).
27. Stroh, T., Erben, U., Köhl, A. A., Zeitz, M. & Siegmund, B. Combined pulse electroporation—a novel strategy for highly efficient transfection of human and mouse cells. *PLoS one* **5**, e9488 (2010).
28. Cukjati, D., Batiuskaite, D., André, F., Miklavčič, D. & Mir, L. M. Real time electroporation control for accurate and safe in vivo non-viral gene therapy. *Bioelectrochemistry* **70**, 501–507 (2007).
29. Faurie, C. *et al.* Electro-mediated gene transfer and expression are controlled by the life-time of DNA/membrane complex formation. *J. Gene Med.* **12**, 117–125 (2010).
30. Stämpfli, R. Reversible electrical breakdown of the excitable membrane of a Ranvier node. *An. Acad. Bras. Cienc.* **30**, 57–63 (1958).
31. Kinosita Jr., K. & Tsong, T. Y. Voltage-induced conductance in human erythrocyte membranes. *Biochimica et Biophysica Acta (BBA) - Biomembranes* **554**, 479–497 (1979).
32. Santra, T. S., Wang, P.-C. & Tseng, F. G. Electroporation Based Drug Delivery and Its Applications. (2013).
33. Kinosita Jr, K. *et al.* Electroporation of cell membrane visualized under a pulsed-laser fluorescence microscope. *Biophysical journal* **53**, 1015–1019 (1988).
34. Vincelette, R. L. *et al.* Thresholds for phosphatidylserine externalization in chinese hamster ovarian cells following exposure to nanosecond pulsed electrical fields (nsPEF). *PLoS one* **8**, e63122 (2013).
35. Flickinger, B., Berghöfer, T., Hohenberger, P., Eing, C. & Frey, W. Transmembrane potential measurements on plant cells using the voltage-sensitive dye ANNINE-6. *Protoplasma* **247**, 3–12 (2010).
36. Hibino, M., Itoh, H. & Kinosita Jr, K. Time courses of cell electroporation as revealed by submicrosecond imaging of transmembrane potential. *Biophysical journal* **64**, 1789–1800 (1993).
37. Hibino, M., Shigemori, M., Itoh, H., Nagayama, K. & Kinosita Jr, K. Membrane conductance of an electroporated cell analyzed by submicrosecond imaging of transmembrane potential. *Biophysical journal* **59**, 209–220 (1991).
38. Zaharoff, D. A., Henshaw, J. W., Mossop, B. & Yuan, F. Mechanistic analysis of electroporation-induced cellular uptake of macromolecules. *Experimental Biology and Medicine* **233**, 94–105 (2008).
39. Pucihar, G., Kotnik, T., Miklavčič, D. & Teissié, J. Kinetics of transmembrane transport of small molecules into electroporabilized cells. *Biophysical journal* **95**, 2837–2848 (2008).
40. Canatella, P. J., Karr, J. F., Petros, J. A. & Prausnitz, M. R. Quantitative study of electroporation-mediated molecular uptake and cell viability. *Biophysical Journal* **80**, 755–764 (2001).
41. Gabriel, B. & Teissie, J. Direct observation in the millisecond time range of fluorescent molecule asymmetrical interaction with the electroporabilized cell membrane. *Biophysical journal* **73**, 2630–2637 (1997).
42. He, H., Chang, D. C. & Lee, Y.-K. Using a micro electroporation chip to determine the optimal physical parameters in the uptake of biomolecules in HeLa cells. *Bioelectrochemistry* **70**, 363–368 (2007).
43. Prausnitz, M. R. *et al.* A quantitative study of electroporation showing a plateau in net molecular transport. *Biophysical journal* **65**, 414–422 (1993).
44. Rols, M.-P. & Teissié, J. Electroporabilization of mammalian cells to macromolecules: control by pulse duration. *Biophysical journal* **75**, 1415–1423 (1998).
45. Saulis, G. & Saulė, R. Size of the pores created by an electric pulse: Microsecond vs millisecond pulses. *Biochimica et Biophysica Acta (BBA)-Biomembranes* **1818**, 3032–3039 (2012).
46. Teissie, J. & Rols, M.-P. An experimental evaluation of the critical potential difference inducing cell membrane electroporabilization. *Biophysical journal* **65**, 409–413 (1993).
47. He, H., Chang, D. C. & Lee, Y.-K. Nonlinear current response of micro electroporation and resealing dynamics for human cancer cells. *Bioelectrochemistry* **72**, 161–168 (2008).
48. Lundqvist, J. A. *et al.* Altering the biochemical state of individual cultured cells and organelles with ultramicroelectrodes. *Proceedings of the National Academy of Sciences* **95**, 10356–10360 (1998).
49. Prausnitz, M. R., Milano, C. D., Gimm, J. A., Langer, R. & Weaver, J. C. Quantitative study of molecular transport due to electroporation: uptake of bovine serum albumin by erythrocyte ghosts. *Biophysical journal* **66**, 1522–1530 (1994).
50. Kotnik, T., Pucihar, G., Reberšek, M., Miklavčič, D. & Mir, L. M. Role of pulse shape in cell membrane electroporabilization. *Biochimica et Biophysica Acta (BBA)-Biomembranes* **1614**, 193–200 (2003).
51. Pucihar, G., Mir, L. M. & Miklavčič, D. The effect of pulse repetition frequency on the uptake into electroporabilized cells in vitro with possible applications in electrochemotherapy. *Bioelectrochemistry* **57**, 167–172 (2002).
52. Neumann, E. Membrane electroporation and direct gene transfer. *Bioelectrochemistry and bioenergetics* **28**, 247–267 (1992).

53. Faurie, C. *et al.* Effect of electric field vectoriality on electrically mediated gene delivery in mammalian cells. *Biochimica et Biophysica Acta (BBA)-Biomembranes* **1665**, 92–100 (2004).
54. Miklavcic, D. & Towhidi, L. Numerical study of the electroporation pulse shape effect on molecular uptake of biological cells. *Radiology and oncology* **44**, 34–41 (2010).
55. Pucihar, G., Kotnik, T., Kandušer, M. & Miklavčič, D. The influence of medium conductivity on electroporation and survival of cells in vitro. *Bioelectrochemistry* **54**, 107–115 (2001).
56. Prasanna, G. L. & Panda, T. Electroporation: basic principles, practical considerations and applications in molecular biology. *Bioprocess engineering* **16**, 261–264 (1997).
57. Hojman, P. *et al.* Physiological effects of high-and low-voltage pulse combinations for gene electrotransfer in muscle. *Human gene therapy* **19**, 1249–1260 (2008).
58. Sadik, M. M., Li, J., Shan, J. W., Shreiber, D. I. & Lin, H. Quantification of propidium iodide delivery using millisecond electric pulses: Experiments. *Biochimica et Biophysica Acta (BBA)-Biomembranes* **1828**, 1322–1328 (2013).
59. Schoenbach, K. H., Beebe, S. J. & Buescher, E. S. Intracellular effect of ultrashort electrical pulses. *Bioelectromagnetics* **22**, 440–448 (2001).
60. Teissie, J., Eynard, N., Gabriel, B. & Rols, M. P. Electroporation of cell membranes. *Advanced drug delivery reviews* **35**, 3–19 (1999).
61. Nickoloff, J. A. *Animal cell electroporation and electrofusion protocols*. (Springer, 1995).
62. Tryfona, T. & Bustard, M. T. Enhancement of biomolecule transport by electroporation: a review of theory and practical application to transformation of *Corynebacterium glutamicum*. *Biotechnology and bioengineering* **93**, 413–423 (2006).
63. Neal, R. E. & Davalos, R. V. The feasibility of irreversible electroporation for the treatment of breast cancer and other heterogeneous systems. *Ann Biomed Eng* **37**, 2615–2625 (2009).
64. Nuccitelli, R. *et al.* Nanosecond pulsed electric fields cause melanomas to self-destruct. *Biochem Biophys Res Commun* **343**, 351–360 (2006).
65. Rubinsky, B., Onik, G. & Mikus, P. Irreversible electroporation: a new ablation modality--clinical implications. *Technol. Cancer Res. Treat.* **6**, 37–48 (2007).
66. Schoenbach, K. H., Joshi, R. P., Stark, R. H., Dobbs, F. C. & Beebe, S. J. Bacterial decontamination of liquids with pulsed electric fields. *IEEE Transactions on Dielectrics and Electrical Insulation* **7**, 637–645 (2000).
67. Kotnik, T., Kramar, P., Pucihar, G., Miklavcic, D. & Tarek, M. Cell membrane electroporation- Part 1: The phenomenon. *IEEE Electrical Insulation Magazine* **28**, 14–23 (2012).
68. Becker, S. M. & Kuznetsov, A. V. Local temperature rises influence in vivo electroporation pore development: a numerical stratum corneum lipid phase transition model. *J Biomech Eng* **129**, 712–721 (2007).
69. Teissie, J., Golzio, M. & Rols, M. P. Mechanisms of cell membrane electroporation: a minireview of our present (lack of?) knowledge. *Biochimica et Biophysica Acta (BBA)-General Subjects* **1724**, 270–280 (2005).
70. Gowrishankar, T. R., Stewart, D. A. & Weaver, J. C. Model of a confined spherical cell in uniform and heterogeneous applied electric fields. *Bioelectrochemistry* **68**, 181–190 (2006).
71. Joshi, R. P., Hu, Q. & Schoenbach, K. H. Dynamical modeling of cellular response to short-duration, high-intensity electric fields. *IEEE Transactions on Dielectrics and Electrical Insulation* **10**, 778–787 (2003).
72. Krassowska, W. & Filev, P. D. Modeling electroporation in a single cell. *Biophysical journal* **92**, 404–417 (2007).
73. Joergensen, M., Agerholm-Larsen, B., Nielsen, P. E. & Gehl, J. Efficiency of Cellular Delivery of Antisense Peptide Nucleic Acid by Electroporation Depends on Charge and Electroporation Geometry. *Oligonucleotides* **21**, 29–37 (2011).
74. Li, J., Tan, W., Yu, M. & Lin, H. The effect of extracellular conductivity on electroporation-mediated molecular delivery. *Biochimica et Biophysica Acta (BBA)-Biomembranes* **1828**, 461–470 (2013).
75. Venslauskas, M. S., Šatkauskas, S. & Rodaitė-Riševičienė, R. Efficiency of the delivery of small charged molecules into cells in vitro. *Bioelectrochemistry* **79**, 130–135 (2010).
76. Teissie, J., Escoffre, J., Rols, M. & Golzio, M. Time dependence of electric field effects on cell membranes. A review for a critical selection of pulse duration for therapeutical applications. *raon* **42**, 196–206 (2008).
77. Golzio, M., Teissie, J. & Rols, M.-P. Direct Visualization at the Single-Cell Level of Electrically Mediated Gene Delivery. *Proceedings of the National Academy of Sciences of the United States of America* **99**, 1292–1297 (2002).
78. Klenchin, V. A., Sukharev, S. I., Serov, S. M., Chernomordik, L. V. & Chizmadzhev YuA. Electrically induced DNA uptake by cells is a fast process involving DNA electrophoresis. *Biophys. J.* **60**, 804–811 (1991).
79. Wolf, H., Rols, M. P., Boldt, E., Neumann, E. & Teissie, J. Control by pulse parameters of electric field-mediated gene transfer in mammalian cells. *Biophys. J.* **66**, 524–531 (1994).
80. Little, J. B. Quantitative Studies of Radiation Transformation with the A31-11 Mouse BALB/3T3 Cell Line. *Cancer Res* **39**, 1474–1480 (1979).

81. Saulis, G. Pore disappearance in a cell after electroporation: theoretical simulation and comparison with experiments. *Biophysical journal* **73**, 1299–1309 (1997).
82. DeBruin, K. A. & Krassowska, W. Modeling electroporation in a single cell. I. Effects of field strength and rest potential. *Biophysical Journal* **77**, 1213–1224 (1999).
83. Pliquett, U. *et al.* Asymmetric changes in membrane conductance due to hyper- and depolarization: probing with current and voltage clamp. in *IFMBE Proc* **11**, 1923 (2005).
84. Krassen, H., Pliquett, U. & Neumann, E. Nonlinear current–voltage relationship of the plasma membrane of single CHO cells. *Bioelectrochemistry* **70**, 71–77 (2007).
85. Chernomordik, L. V. *et al.* The electrical breakdown of cell and lipid membranes: the similarity of phenomenologies. *Biochimica et Biophysica Acta (BBA)-Biomembranes* **902**, 360–373 (1987).
86. Khine, M., Ionescu-Zanetti, C., Blatz, A., Wang, L.-P. & Lee, L. P. Single-cell electroporation arrays with real-time monitoring and feedback control. *Lab on a Chip* **7**, 457–462 (2007).
87. Kennedy, S. M., Ji, Z., Hedstrom, J. C., Booske, J. H. & Hagness, S. C. Quantification of electroporative uptake kinetics and electric field heterogeneity effects in cells. *Biophysical journal* **94**, 5018–5027 (2008).
88. Weaver, J. C. & Chizmadzhev, Y. A. Theory of electroporation: a review. *Bioelectrochemistry and bioenergetics* **41**, 135–160 (1996).
89. Zhou, Y., Shi, J., Cui, J. & Deng, C. X. Effects of extracellular calcium on cell membrane resealing in sonoporation. *J Control Release* **126**, 34–43 (2008).
90. Tekle, E., Astumian, R. D. & Chock, P. B. Electroporation by using bipolar oscillating electric field: an improved method for DNA transfection of NIH 3T3 cells. *Proceedings of the National Academy of Sciences* **88**, 4230–4234 (1991).
91. Kandušer, M., Šentjerc, M. & Miklavčič, D. Cell membrane fluidity related to electroporation and resealing. *European Biophysics Journal* **35**, 196–204 (2006).
92. Gabriel, B. & Teissié, J. Control by electrical parameters of short- and long-term cell death resulting from electroporation of Chinese hamster ovary cells. *Biochimica et Biophysica Acta (BBA) - Molecular Cell Research* **1266**, 171–178 (1995).
93. Xie, T. D., Sun, L. & Tsong, T. Y. Study of mechanisms of electric field-induced DNA transfection. I. DNA entry by surface binding and diffusion through membrane pores. *Biophys. J.* **58**, 13–19 (1990).
94. Yumura, S., Matsuzaki, R. & Kitanishi-Yumura, T. Introduction of macromolecules into living Dictyostelium cells by electroporation. *Cell Struct. Funct.* **20**, 185–190 (1995).

Chapter 4

THE DEVELOPMENT OF A CHIP FOR TARGETED TRANSDERMAL ELECTROGENTRANSFER

4.1. Introduction

4.1.1. Background of tissue electroporation

Electroporation (EP) method is a well-known technique that has been utilized for various drug/gene/proteins delivery applications over the last 40 years. Neumann *et al.* have pioneered the EP-mediated gene delivery method in 1982¹, and it was developing rapidly during the following decade thanks to its ease-of-use and promising outcomes²⁻⁹. Although a complete understanding of the mechanism of EP's action has not been reached yet, it is known that in the presence of an external electric field cell permeability increases and electrophoretic forces help to introduce exogenous molecules into the cell cytoplasm. EP can permeabilize the cells either reversibly, making cell membranes reseal, or irreversibly, leaving them "leaky" post-pulsation. Electrical pulsing parameters is the key factor for manipulating EP's reversibility. Irreversible EP is used for purposes such as debacterilization and tissue ablation¹⁰⁻¹³, while reversible EP has a vast scope of application that includes drug/gene/protein deliveries^{5,14-19}. EP has been explored extensively, aiming to achieve the tradeoff between pulse strength and viability post-pulsation. High pulse strength increases the delivery whereas decreases the viability²⁰⁻²⁷. In *in vivo* studies, low viability and tissue damage are the critical impediment factors, being the reasons why EP has been laid aside for a long time. Consequently, for the last 40 years, FDA has not approved any *in vivo* electroporation applications on the market.

The recent developments of the DNA-based vaccines^{28–34}, T-cell immunotherapy³⁵, and gene editing^{36–38} have re-highlighted the EP technique as a primary delivery method. In particular, transdermal EP has become a preferable method thanks to its significant advantages, such as accessibility³⁹, minimized enzymatic degradation⁴⁰, and a high concentration of dendritic cells for immunotherapy⁴¹. Transdermal EP can be categorized into two groups based on the type of devices' electrodes: 1) surface electrode or 2) penetrating electrode. Surface electrodes, typically in the form of conductive plates, are placed directly on the surface of the skin. The stratum corneum (SC) layer, the primary barrier, functions as an insulator, standing in EP's way to the deeper layers of the skin. Therefore, using surface electrodes requires high-intensity pulses. In the case of penetrating electrodes, the target tissue is relatively more accessible. The SC barrier can be overcome easily and, depending on the needle length, epidermis or both epidermis and dermis layer can be permeabilized (the skin layers can be seen in Figure 4.1). Pulsing parameters should be optimized to avoid tissue damage; however, long needles may cause pain and stress. The following section (§ 4.1.2. Literature survey) will provide a summary on the transdermal EP devices currently on the market.

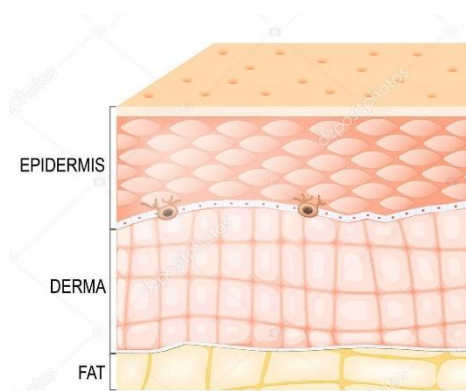
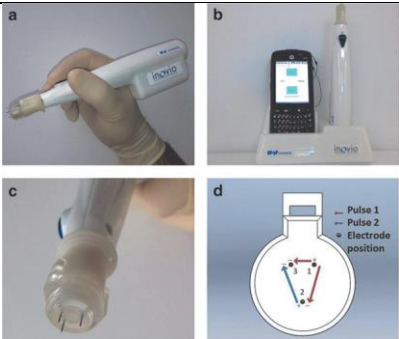
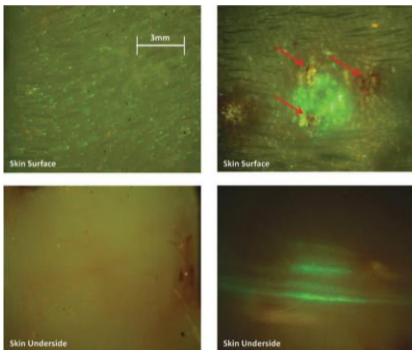
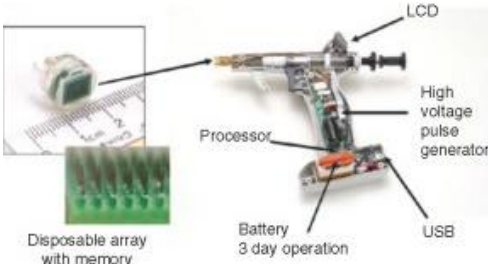
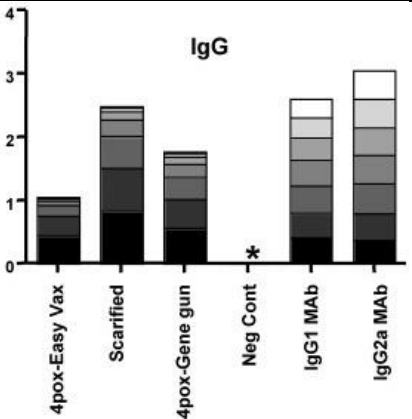



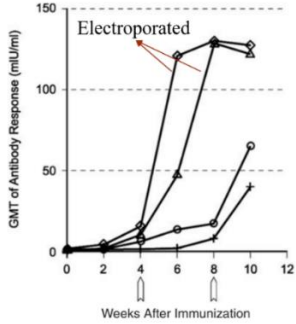
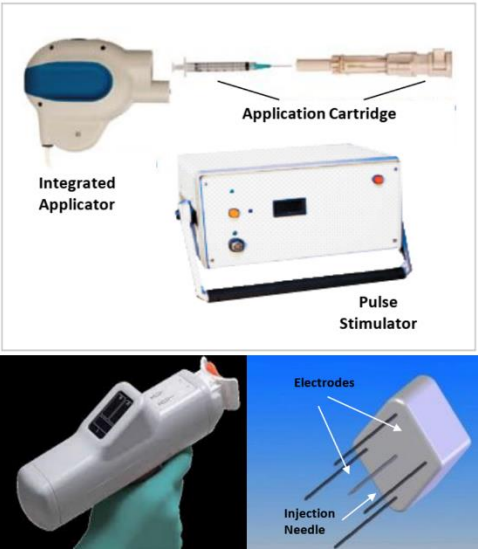
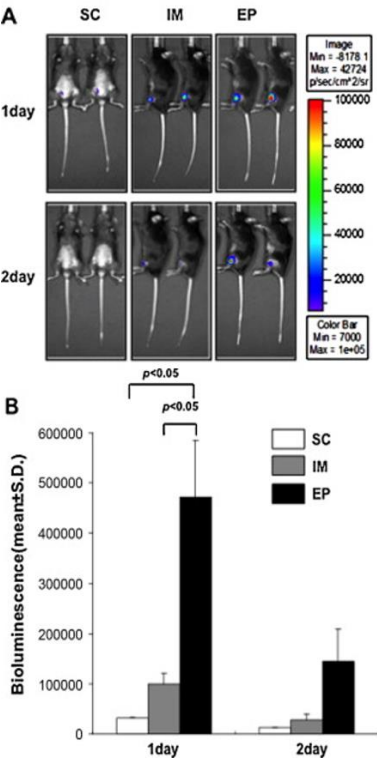
Figure 4.1 A schematic of the skin layers. The SC layer is not shown for simplicity. The epidermis layer has a higher cell density than the dermis layer.


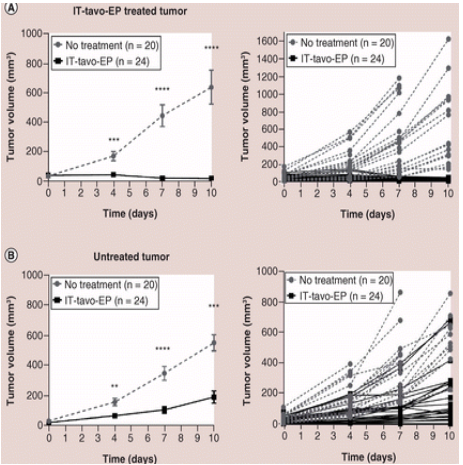
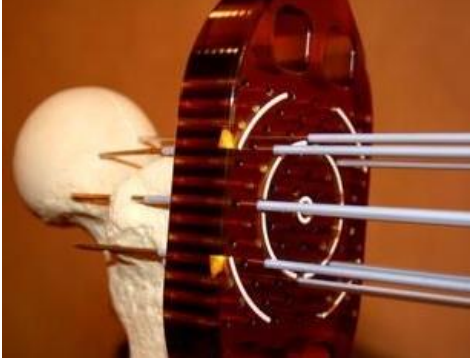
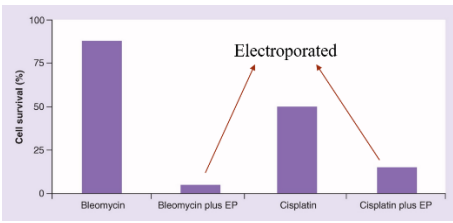
4.1.2. Literature survey

EP is the most promising delivery technique for DNA vaccines, and around 30 Phase I and II clinical trials are employing it for delivery⁴². The EP method stands out among other techniques because it does not require additional chemicals, preservatives, or adjuvants. Despite the availability of various commercial EP platforms on today's market, the focus of this study is to develop a transdermal EP treatment by using penetrating electrode arrays. Therefore, this section reviews several commercial EP platforms in development with penetrating electrodes, including CELLECTRA, Easy Vax, MedPulser, Trigrad, OncoSec, and Cliniporator. The majority of devices are undergoing Phase I and II clinical trials⁴³; however, there are currently no FDA-approved electroporation devices on the market. Table 4-1 lists EP devices that utilize penetrating electrodes for either transdermal or intramuscular application. The electrode designs (in terms of size, number, and the gap between them), pulse designs (in terms of amplitude, duration, intervals, and number of pulses), and delivery vector are listed under the device design section along with a representative picture. Exemplary results and brief conclusions are listed in the result section along with the selected figures.

Table 4-1 The list of commercially available EP devices that utilize penetrating electrodes for either transdermal or intramuscular application. Most of the devices are in the clinical trials. Electrode designs in terms of size, number, the gap between them, pulse designs in terms of amplitude, duration, intervals, and numbers, and delivery vector are listed under the device design section along with a representative picture. Exemplary results and brief conclusions are listed in the result section along with the selected figures.

Device Name	Device Design	Results	Ref.
CELLECTRA®-3P	 <ul style="list-style-type: none"> • 3 sharp electrodes in a triangular array, 3 mm long, 3-5 mm spacing. • 2 sets of 52 ms long 200 V pulse with 198 ms interval. • 50 µg of WizGFP (Aldevron) in 50 µl of 1x PBS was injected to guinea pigs. 	 <ul style="list-style-type: none"> • Results were collected 72 h posttreatment. • GFP expression observed in the needle insertion site. 	44,45
Easy Vax™	 <ul style="list-style-type: none"> • 8 x 10 penetrating electrode array, each 1 mm long and 0.6 mm apart. The average insertion depth of needles was 0.45 mm. • 100 µs long 100 V 6 pulse train with 125 ms interval. • Mice vaccinated with the 4pox DNA vaccine on four arrays, each coated with 30 µg of a separate plasmid. 	 <ul style="list-style-type: none"> • The quantity of DNA required per vaccine is lowered orders of magnitude. • The penetration of the needles does not cause pain due to shallow penetration. • This technique is broadly applicable. 	46,47

Device Name	Device Design	Results	Ref.
MedPulser	 <ul style="list-style-type: none"> • 4-6 penetrating 26-gauge gold-plated needles, 1.5 cm long and 5 mm apart. • 60 ms long 100 V pulse and 190 ms interval, applied for 5 minutes. • 10 μg DNA in 50 μl PBS solution 	 <ul style="list-style-type: none"> • EP has increased the antibody titer dramatically. • The transient inflammation caused by EP triggers a cascade of immune mechanisms that facilitate a response to the expressed antigen or antigens. 	48–50
TriGrid	 <ul style="list-style-type: none"> • 4 penetrating electrodes with 2 mm length, 1.5 mm apart, and a central injection needle. • 0.5 s of pulse train with 40 ms long 55 V pulse and 460 ms intervals. • 1-2 μg of recombinant luciferase protein (Luc) (Promega) was injected. 	 <ul style="list-style-type: none"> • EP is the most effective way to transduce protein into the muscle cells. 	51–53

Device Name	Device Design	Results	Ref.
OncoSec	 <ul style="list-style-type: none"> • 6 penetrating electrodes arranged in a circular array. • 6 pulses with a 400 – 1,500 V DC 100 μs duration with 300 ms intervals • 3-time 0.5 ml administration of 0.5 mg/ml of tavokinogene telseplasmid (0.25 mg fixed dose). 	 <ul style="list-style-type: none"> • EP provides local and systemic antitumor effects. 	54
Cliniporator™	 <ul style="list-style-type: none"> • The needle length, number, and gap between them are adjustable; however, the minimum gap is a centimeter wide. • 100 μs long, up to 3,000 V pulses are applied to electroporate tissue irreversibly. 	 <ul style="list-style-type: none"> • EP is an effective treatment of neoplastic lesions. 	55,56

4.1.3. Statement of objectives

The purpose of this work is to develop a safe and efficient transdermal EP device for targeted gene delivery to benefit human health and welfare. The current research and technology are subjected to limitations. By addressing those limitations, this study states its objectives as:

- Employing penetrating microneedle-electrodes to overcome the insulating SC barrier.
- Utilizing an electric field to permeabilize the cell membranes for gene transfection.
- Designing a PCB-based electroporation chip that has the smallest feature size as possible to lower the voltage requirements for electropermeabilization.
- Targeting the epidermis layer due to its high concentration of keratinocytes and dendritic cells that play a critical role in vaccinations.
- Monitoring the tissue impedance before and after the pulsation to correlate the degree of electropermeabilization with the pulse strength and to estimate the pulsing parameters for *in vivo* applications.
- Co-localizing both DNA delivery and electric pulses to reach a better understanding of electroporation's mechanism of action in the tissue and to improve its efficiency.

Building on our significant previous experience in cell EP on both experimental^{26,57,58} and computational⁵⁹⁻⁶² fronts, the scientific objective of this study is to understand the biophysical aspects of skin EP.

4.2. Materials and Methods

4.2.1. Design of the 1st and 2nd Generation Chips

Owing to their readiness and availability in the market, EP chips were developed based on the printed circuit board (PCB) technology. The 1st generation shown in Figure 4.2 has 100 needle holders, 4 units of 25-pin connectors, and is 10 x 10 cm in size. The purpose of the 1st gen. device was to understand the applicability of the PCB technology in the EP field and the feasibility of mass production. A 3D model designed by SolidWorks (Dassault Systèmes SolidWorks Corporation, Waltham, MA) is shown in Figure 4.2a. Due to the 25-pin connector size, the board size was limited to a minimum of 10 cm-long edge. Figure 4.2b shows the PCB layout design with traces, designed with the PCBArtist software (Advanced Circuits, Aurora, CO). The 1st gen. EP chip has a two-conductive-layer structure (Figure 4.3). The PCB board was drilled with through-holes 300 μm in diameter for needle housing, and the through-holes were plated with copper to provide an electrical connection. The center-to-center distance between the holes was designed to be 1.3 mm. The distance between electrodes was limited due to the minimum tracing gap and thickness set by the manufacturer. Also, the 1st gen. has independently controllable needles, which is a compromise between a smaller size and multi-functionality of the EP chip design. In the 2nd gen. EP chip, electrodes are grouped in 4 groups for the sake of the size. As shown in Figure 4.4, the 2nd gen. EP chip has 4 x 4 electrode holes 200 μm in diameter and spaced 0.75 mm apart, a 1-unit 4-pin connector, and is 1 x 1 cm in overall size. It has 4 conductive layers and 3 via holes that connect the bottom layers to the top layer since the 4-pin connector has a surface mount soldering. Increasing the number of layers, grouping the electrode configuration, and choosing a smaller connector has improved the size of the 2nd gen. by a hundredfold. Furthermore, the cost of board manufacturing has lowered from \$100 to \$0.5, making it feasible for mass production. Stainless steel acupuncture

needles were employed to penetrate the skin and apply the pulse. The comparison of the 1st and 2nd gen. EP chips is listed in Table 4-2.

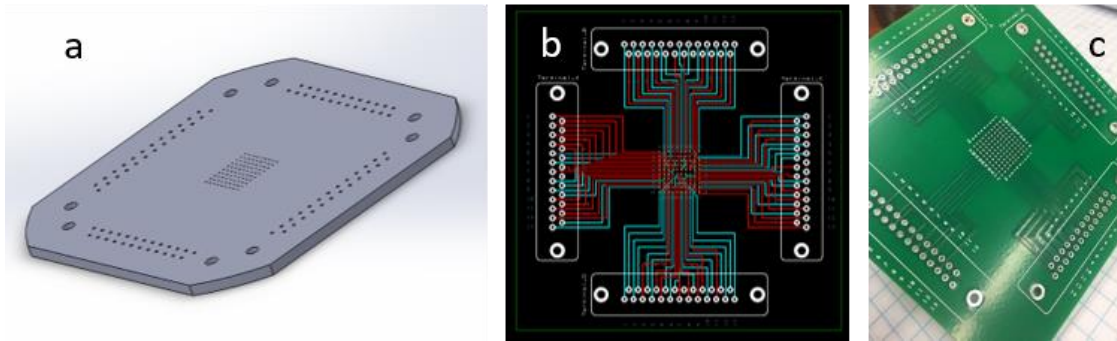


Figure 4.2 1st generation EP chip PCB design. It has 10x10 needle holders and 4 units 25-pin connector location. (a) 3D model designed in SolidWorks. (b) The PCB layout design with traces built with PCBArtist software. (c) A picture of 1st gen. EP chip fabricated by Advanced Circuits, Aurora, CO.

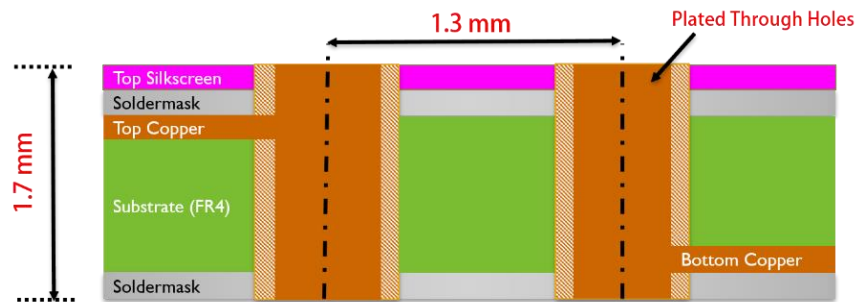


Figure 4.3 Printed circuit board (PCB) layer structure. Two-conductive-layer PCB was designed for the 1st generation EP chip (Top Copper and Bottom Copper). The PCB board was drilled with through-holes with 300 μm diameter for needle housing, and the through-holes were plated with copper to provide an electrical connection. The center-to-center distance between holes was designed to be 1.3 mm.

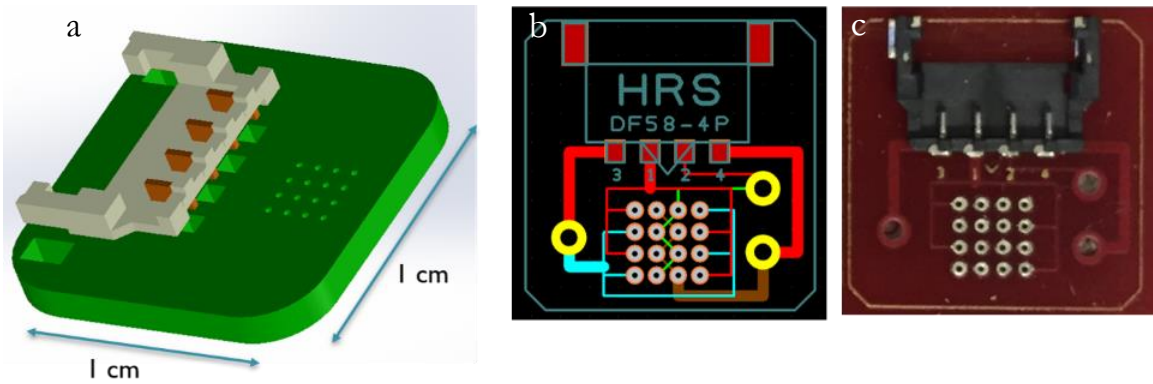


Figure 4.4 2nd generation EP chip PCB design. It has 4x4 needle holders (200 μm diameter) spaced 0.75 mm apart and 1-unit 4-pin connector (HRS, DF58-4P, 5x5 mm in size) location. (a) The 3D model designed in SolidWorks. (b) The PCB layout design with traces built with PCBArtist software. It has 4 conductive layers and 3 via holes that connect the bottom layers to the top layer of the connector. (c) A picture of 2nd gen. EP chip fabricated by Advanced Circuits, Aurora, CO.

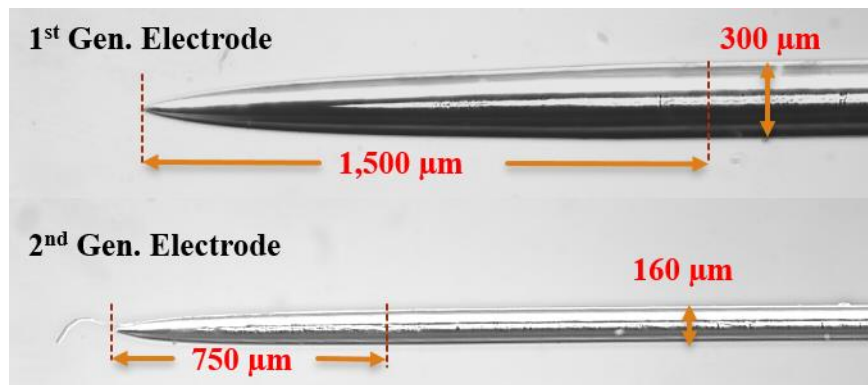


Figure 4.5 Stainless steel acupuncture needles were used for the EP chip. (top) In the 1st gen., 300 μm diameter acupuncture needle tapers to a fine point over a 1.5 mm tip length at a 5.7° taper angle, (bottom) in the 2nd gen. 160 μm diameter acupuncture needle tapers to a fine point over a 745 μm tip length at a 6.129° taper angle were attached to the EP chip.

4.2.1.1. Assembly procedure for the 1st gen. EP chip

The main requirements for the assembly are the electrical connection for delivering pulses and mechanical strength that is capable of resisting the sheer force while penetrating the skin. Originally, the method of soldering the needles with a solder-wire was considered. However, acupuncture needles were not good heat conductors, so it was not possible to reach the melting temperature of the solder. Therefore, a manual soldering procedure was chosen.

Figure 4.7 (from left to right) shows the scheme of the general assembly procedure. First, the plated-through holes were filled with solder, and, while the solder was still warm and fluid, the needles were inserted through the plated holes. The protruding length, further called “needle length” for consistency, was controlled by a spacer between the PCB and flat ground, reaching mostly 1 mm. After the solder solidified, the backs of the needles were clipped, and more solder was added for a greater electrical connection and mechanical strength. The electrical connectivity and mechanical strength tests were performed before proceeding to actual skin experiments. A 5 – 10 Ω resistance was measured from the tip of the needle to the end of the connector cable, and a single needle assembly strength was able to resist up to 10 N force. However, as seen in Figure 4.7, the sharpness of the needles was distorted during the assembly procedure, and small amounts of solder had overflowed to the application’s skin-facing side. Therefore, a better method of assembling the needles was needed.

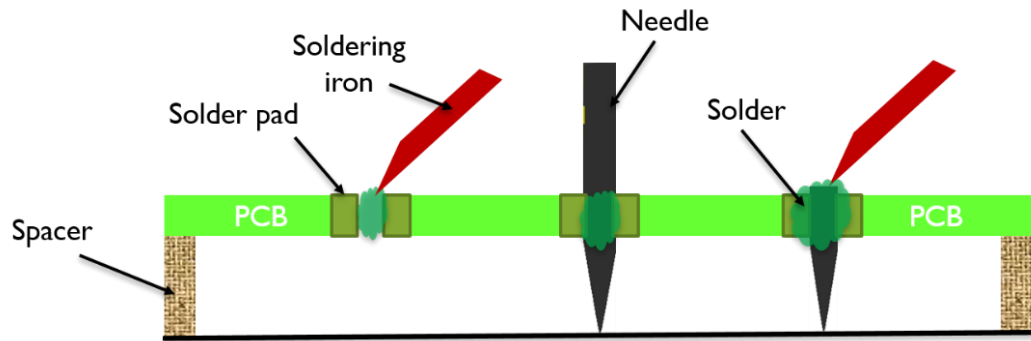


Figure 4.6 Needle assembly procedure of the 1st gen. EP chip. Electrode holders are filled with solder and, while the solder is still warm and fluid, the needles get inserted. After the solder solidifies, the back of the needle is clipped and more solder is added for a greater electrical connection and mechanical strength.

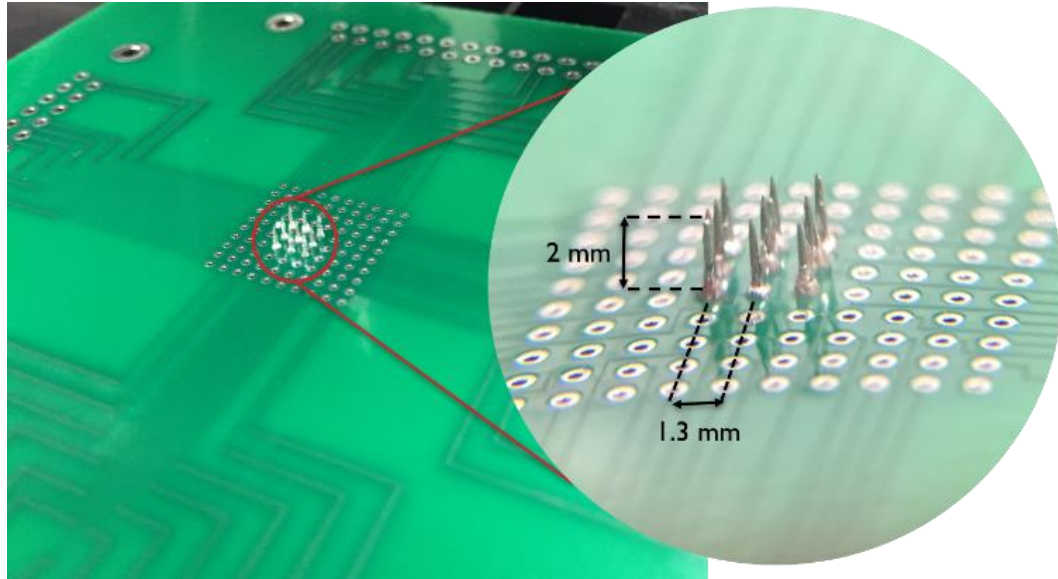


Figure 4.7 1st gen. EP Chip with needles attached by soldering. Initially, 3x3 needle array is used. The sharpness of the needles is low due to the assembly procedure, and a small amount of solder has flowed towards the application's skin-facing side.

4.2.1.2. Assembly procedure for the 2nd gen. EP chip

In the 2nd gen. EP chip, the assembly procedure was revised to eliminate the issues experienced with the 1st gen. The method was updated to preserve the sharpness of the needle tips and increase the manufacturing speed. First, the pre-cut needles were inserted through the holes and fixed with the light-curable polymer (Dymax Corporation, Torrington, CT). The needle length was controlled similarly to the previous procedure by a spacer. It was ensured that the tips of the needles from the skin-facing side were entirely covered with the curable polymer. To prevent its overflow before curing, the skin-facing side was covered with clear tape. It was tested that punching through the tape was not altering the sharpness of the needles. The polymer was cured by exposition to UV-light for 3-5 s. A solder flux that was compatible with dip-solder was used to avoid the misconnection of the needles. Then, the chip was dipped into the solder bath, as shown in Figure 4.8, for a few seconds. It should be noted that the chip surface had to be cleaned from any dirt or dust before dipping. The pictures

of an assembled 2nd gen. EP chip are presented in Figure 4.9. The EP chip is connected to a ribbon cable for electrical connection.

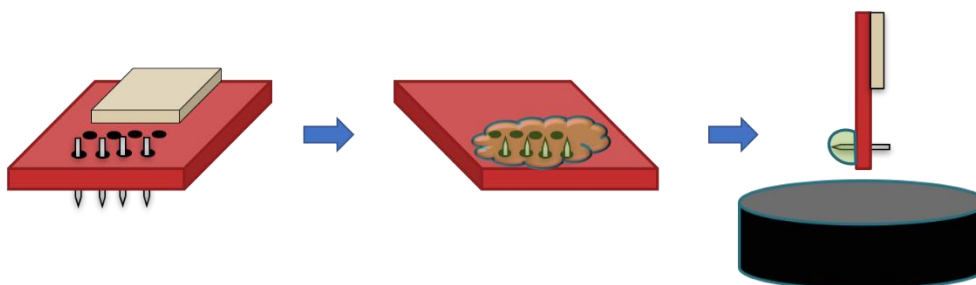


Figure 4.8 2nd gen. EP chip assembly procedure. The pre-cut needles are attached to the PCB by using a light-curable polymer. The tips of the needles are covered entirely. Then, the chip is dipped into the solder bath for a few seconds.



Figure 4.9 (left) 2nd gen. EP chip pictures with the needles attached. (right) The space between the needles and their protruding length are shown schematically.

Table 4-2 Comparison between 1st and 2nd gen. EP chip designs.

	<i>1st Design</i>	<i>2nd Design</i>
Board size	10 x 10 cm	1 x 1 cm
Electrode configuration	10 x 10 (all independent)	4 × 4 (4 groups)
Distance between electrodes	1.3 mm	0.75 mm
Needle size	Ø 300 μm	Ø 160 μm
Connector	4 units 25 pin connector	1 unit 4-point surface connector (5 × 5 mm in size)
Assembly	Soldering manually with a hot solder iron	Batch soldering with dip soldering

4.2.2. Mechanical characterization for insertion

Knowing what length of the needles allows for sufficient penetration is critical to design a device for targeted delivery. The skin consists of layers, and each layer has a different physiological structure. Therefore, a mechanical characterization study was performed first to investigate the insertion depth with porcine skin. The needles were coated with ink and then inserted into the skin, making it easy to observe the needle traces, as shown in Figure 4.10. The skin samples were sectioned by using a cryotome (Shandon AS620 Cryostat, Thermo Fisher Scientific, Waltham MA) in 50 μm thickness and imaged.

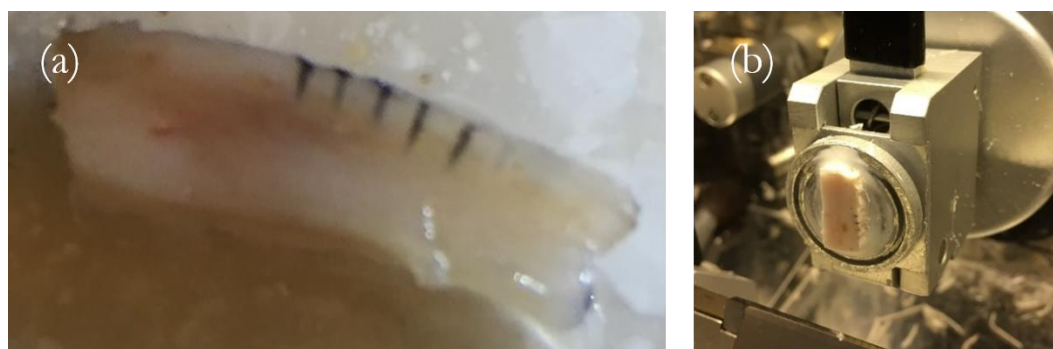


Figure 4.10 The implementation of the 1st gen. chip to mechanically determine the needle insertion to porcine skin. a) A side view of a skin sample that shows the needle traces. b) The skin samples were sectioned by using a cryotome in 50 μm thickness.

4.2.3. Electrical characterization for pulse application

Another critical aspect of successful electroporation is the correct application of the desired pulsation. Depending on the pulse strength, the biological tissue might require a strong current source. Therefore, the electronics must be tested prior to pulsation. The electric pulses were generated by a function generator (Tektronix AFG3022C, Melrose, MA) and amplified by a high-frequency, high-voltage amplifier (Trek Model PZD 350, Lockport, New York, NY). Additionally, the impedance of the skin was probed using a potentiostat Reference 600+ (GAMRY Instruments, Warminster, PA). Figure 4.11 shows a schematic diagram of the

experiment's setup. A custom-made switch was used to control the EP pulse from the amplifier and the sensing signal from the potentiostat. The electric field distribution was characterized with the 1st gen. chip shown in Figure 4.12a. The insertion depth varied between 0.5 and 2 mm. The configuration of probing and running electrodes is also shown in Figure 4.12b. Typically, the running electrodes (blue dots) that deliver the pulse were on the sides, and the probing electrodes (green dots) were in the middle. The electrical characterization was first performed with standard conductive fluid at 84 $\mu\text{S}/\text{cm}$ (\sim epidermis) later with the porcine skin sample.

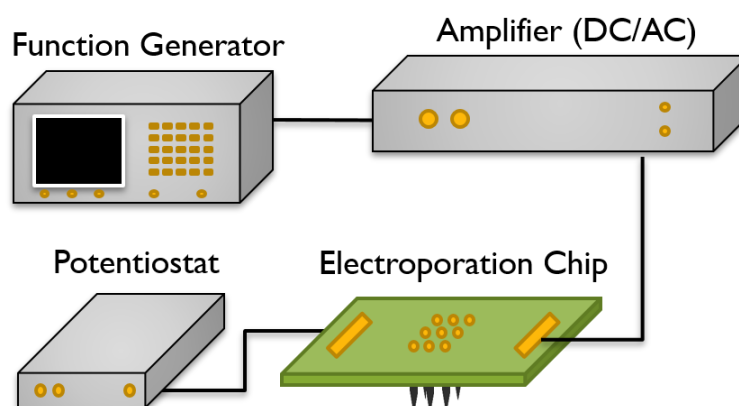


Figure 4.11 Schematic of the experiment's setup, including a function generator, amplifier, potentiostat, and an EP chip.

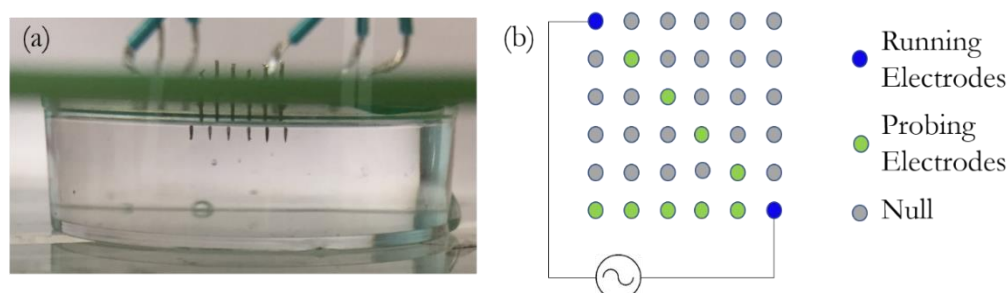


Figure 4.12 The electric field distribution was probed by using a potentiostat. (a) An exemplary picture of electrical characterization with conductive fluid. Arrays of six needles in line, equally distanced by 1.3 mm, were used. The insertion depth was between 0.5 and 2 mm. (b) The probing and running electrodes configuration is shown in a diagram. Typically, the running electrodes (blue dots) that deliver the pulse were on the outer edge, and the probing electrodes were in the middle rows, as indicated above with green dots.

4.2.4. EP assays

Once the system was assured mechanically and electrically, the next was to test EP on the skin. Three different approaches were employed to do this. (1) Propidium iodide test, (2) Impedance test, and (3) GFP expression test.

4.2.4.1. Propidium iodide (PI) test with explanted fresh porcine skin

PI is an impermeant dye (668 MW) that binds with nucleic acid and glows under the TRITC channel (Ex/Em: 535/617). The PI test was performed to assess the electric field distribution and viability of the tissue over time. All fresh porcine skin studies were performed under protocols approved by Rutgers IACUC committee (PROTO201702610 - Porcine skin harvesting). The skin was freshly harvested from euthanized 3 to 5-week-old piglets. A summary of the procedure is given schematically in Figure 4.13. The skin was carefully cleaned by 70% ethanol and then shaved and depilated. Then it was cut into small square pieces approximately 2×2 cm. The subcutaneous fat and tissue were removed carefully with a scalpel. 50 – 100 μ l of 40 μ g/ml Propidium Iodide (Molecular Probes, Inc., Eugene, OR) or 20 μ g/ml pEGFP (GeneOne Life Science, Inc., Seoul, Korea) in PBS solution was injected into the samples with MicronJet600 (Figure 4.14a) microneedles (NanoPass Technologies Ltd., Nes Ziona, Israel) before the EP treatment. The pulse parameters were varied for different experiments. After pulsation, the skin samples were immediately put into a modified Eagle's medium (MEM) at 37°C on a rocker in an incubator. After some time, the skin tissue was sectioned either along the coronal plane across the insertion track or along the transverse plane perpendicular to the insertion sites using a cryotome and imaged under an epifluorescent microscope (Olympus IX71). The side view images of the skin section were analyzed with a custom MATLAB code. The PI signal intensity averaged over the area of each layer. Epidermis, dermis, and hypodermis layers were identified with bright field images.

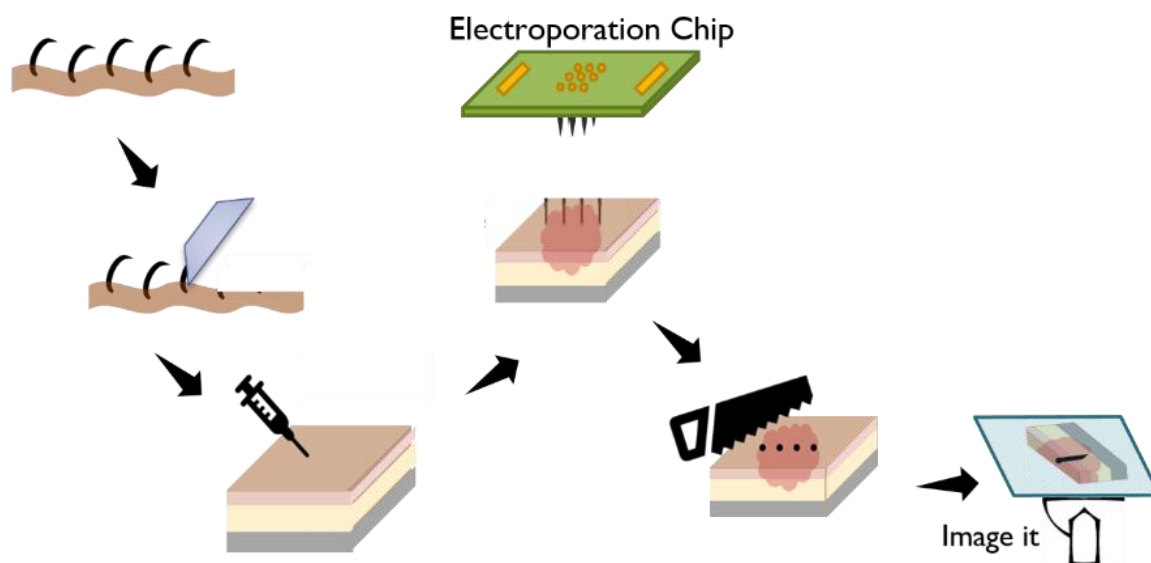


Figure 4.13 A schematic of the fresh porcine skin EP procedure. The skin tissue is depilated first, followed by injection and pulsation. The skin samples are kept in the incubator for some time, then sectioned and imaged under an epifluorescent microscope.

4.2.4.2. Impedance test *in vivo*

The impedance of the live rat skin was measured to probe and detect the electropermeabilization level of the tissue by using a high-frequency potentiostat/galvanostat device (Reference 600+, Gamry Instruments). The electrode configuration of the 2nd gen. chip includes four electrode groups so that each group can be controlled independently. Thus, a 4-point probing method was used for impedance characterization. 1×4 arrayed EP chips were employed, and the impedance was measured at the 3 kHz sensing frequency. Prior to the impedance measurement, the impedance spectrometry analysis had been performed from low frequencies to high frequencies, concluding that 1 - 10 kHz sensing frequencies provided distinguishable readings before and after EP pulsation.

All live animal studies were performed under protocols approved by Rutgers IACUC committee (PROTO201800077 - Transdermal delivery with microelectrode arrays). Rats aged 10-14 weeks old were housed in standard cages at room temperature (Taconic Farms, Inc., MD). Both male and female Sprague-Dawley rats were used. Standard laboratory food and water were given. Before each experiment, rats were anesthetized by isoflurane (GT&S Inc., PA) inhalation and were kept anesthetized during the experiment. To maintain the body temperature at the normal level, the rats were rested on a warm blanket. For each rat, the hair on one side of the abdominal area was carefully shaved, exposing a skin area of approximately 5×3 cm in size. Measurement points were randomly selected, and successive measurements were performed for the same point. The penetration of the needles was verified by impedance measurements resulting in an impedance value of $\sim 100 - 2,000 \Omega$. After the insertion, the medical tape was used to fix the chip on the insertion site. Impedance measurements were taken before and after pulsation. Different pulse strengths were applied.

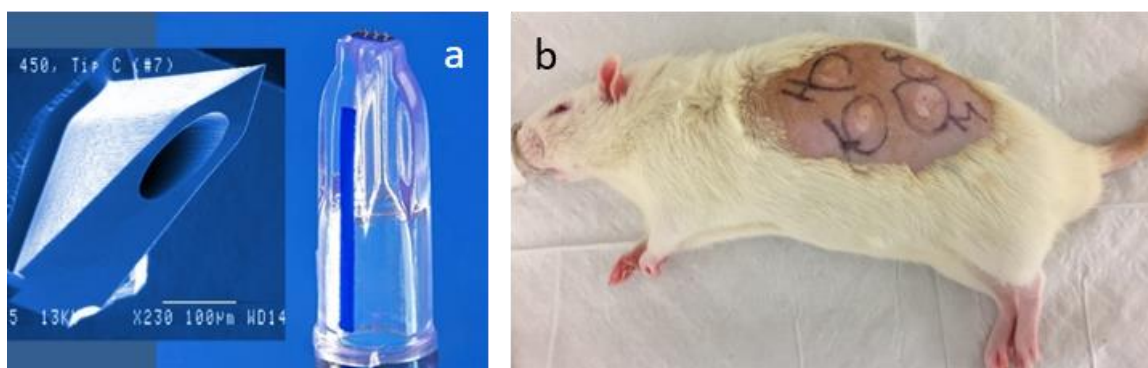


Figure 4.14 (a) A picture of a MicronJet600 microneedle, the insert is the magnified view of the injector blade made of pure silicon crystal. (b) An exemplary picture of a test-rat, four sites were injected and marked. The rat was kept anesthetized by isoflurane inhalation through the nose cap and rested on a warm blanket.

4.2.4.3. GFP expression test

Before the electroporation treatment, a volume of 25-50 μ l PBS solution, incorporating 8-25 μ g pEGFP (GeneOne Life Science, Inc., Seoul, Korea), was injected with MicronJet600 (shown in Figure 4.14a) microneedles (NanoPass Technologies Ltd., Isreal) at each injection site. Usually, four or five sites were injected per rat as shown in Figure 4.14b. Then, the electric pulses were applied. The animals were dispatched 24 hours post-pulsation for pDNA transfection. Each injection site was excised from the carcass as a separate sample, and the fat layer was carefully removed. The samples were then imaged on an inverted epifluorescent microscope (Olympus IX81).

4.3. Results

4.3.1. Mechanical characterization

The mechanical characterization study was performed to investigate the penetration depth of the needles into the skin tissue. In the epidermis layer, the volume fraction of keratinocytes can be as high as 75%⁶³. In the dermis layer, however, the volume fraction of fibroblasts is much lower, probably less than 1%, depending on the position⁶⁴. Therefore, the penetration depth of the needles plays a critical role in optimizing the pulsing parameters. For instance, if the target is the dermis layer, the electric field should be stronger to electroporate the cells due to their low number. On the other hand, in the epidermis layer, a weaker pulse might have a similar EP effect. The penetration depth of the chips from both generations was tested. The exemplary images are shown in Figure 4.15. In the 1st gen. chip, the needle length was around 2 mm, and the observed penetration depth was about 1 mm. In the 2nd gen. chip, typically, the needle lengths were 1 mm, however, the observed penetration depths were approximately 0.7 mm. This result is consistent with the previous micro needle studies that state that, typically, only about 70% of the needle length penetrate the skin due to its compressibility^{63,64}. It should be noted that the thickness of the used needles also varied as shown in Figure 4.5.

4.3.2. Electrical characterization

Mapping the electric field distribution within the tissue is an essential requirement for adjusting the pulsing parameters. Therefore, the electrical characterization study was performed. In this study, the potential distribution (voltage drop) across the electrodes was probed both in salt solution and porcine skin samples. Figure 4.16a - b show the voltage drop

in a standard salt solution (conductivity of $84 \mu\text{S}/\text{cm}$) with (a) 1x6 electrode array and (b) 3x3 electrode array. It was observed that the bigger voltage drops occurred between the running and probing electrodes due to low conductivity. The probing electrodes acted as a floating electrode; thus, they maintained the potential distribution in an almost flat region. This indicates that in the case of denser arrays the voltage drop is bigger than in more spaced arrays; therefore, employing denser arrays is more beneficial. The low conductivity solution was chosen to have a similar conductivity as in the epidermis. Pulses were applied with an amplitude of 200 mV and lower to avoid the electrolysis effects. The results were compared with the COMSOL simulation that had been computed by Dr. Miao Yu. The simulation results were validated with measurements that established a strong foundation for future simulation studies. Once the salt solution experiments were successful, we proceeded with skin experiments. Fresh porcine skin was used for electrical characterization. The results, shown in Figure 4.16c, seem to be well-consistent with the simulation results. However, there was a bit more deviation from the simulation than the salt solution, which can be expected due to the complexity of the skin structure. Nonetheless, the agreement between the simulation and the obtained data has provided some confidence in the simulation-based design.

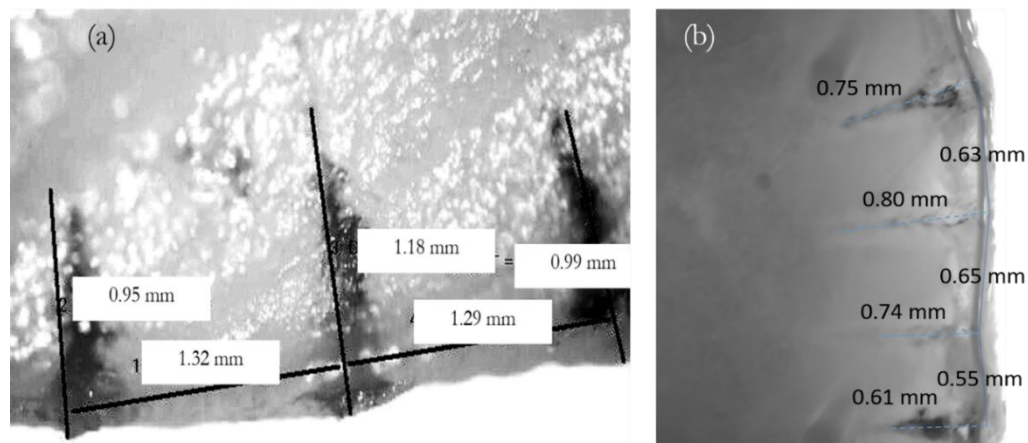


Figure 4.15 A side view of a skin sample that shows the needle traces. (a) 1st gen. chip with 2 mm needle length was implemented, with the average penetration around 1 mm. (2) 2nd gen. chip with 1mm needle length was implemented, the average penetration was approximately 0.7 mm.

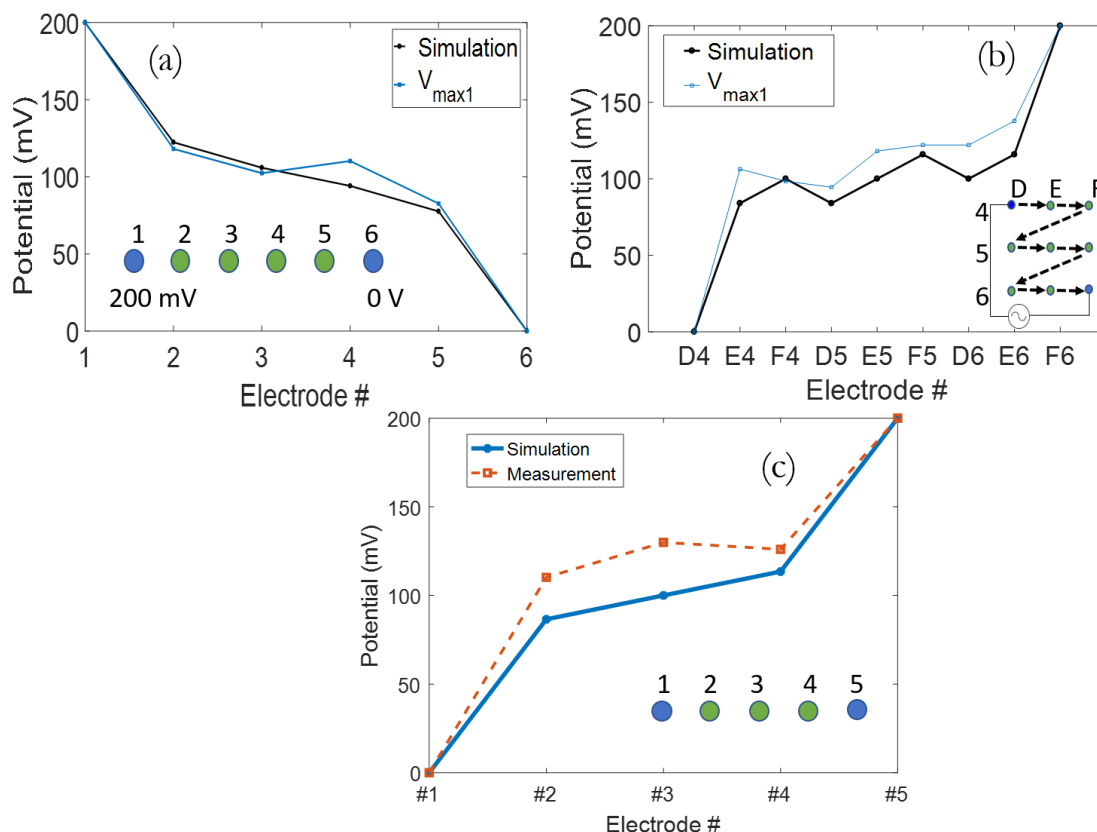


Figure 4.16 The voltage drop across the running electrodes was mapped in a standard salt solution (conductivity of $84 \mu\text{S}/\text{cm}$) with (a) 1x6 electrode array, (b) 3x3 electrode array. The black line represents a COMSOL simulation result that was prepared by Yu, the blue lines are the measurements. (c) Electrical characterization was performed with porcine skin, the penetration depth was around 1 mm, and a 1x5 needle array was used.

4.3.3. EP results

As mentioned previously in § 4.4.1, EP has two main mechanisms, (1) electroporation, and (2) delivery. The previous chapter of this dissertation (Ch. 3) has demonstrated a clear separation of these two mechanisms. Owing to that, it has been understood that electroporation is a strong function of field strength, and a short-duration high-voltage pulse can induce a rapid poration of the membrane. Hence, longer pulse duration is not necessary. On the other hand, the delivery mechanism is driven by mostly electrophoretic forces; therefore, longer pulses would enhance the delivery. To overcome this dilemma, the two-pulse procedure is generally employed, using one strong and short pulse for

permeabilization and another weaker and long pulse for delivery. However, this study aims to deliver a gene *in vivo* transdermally, which introduces some new high-order problems. To understand and solve these problems, this study started with simpler objectives. The first objective was to understand the electric field distribution within the skin layers, and the propidium iodide test was performed to map the field distribution optically. Then, to understand the permeabilization effect electrically, the impedance test was done. Finally, to demonstrate the efficiency of EP, the GFP expression study was performed.

4.3.3.1. Propidium iodide test results

PI is an impermeant dye (668 MW) that binds with nucleic acid and glows under the TRITC channel (Ex/Em: 535/617). The PI test was performed to assess the electric field distribution and viability of the tissue over time. In Figure 4.17, an exemplary side view of the sliced skin section is shown. The needles were coated with ink and then inserted into the skin, making it easy to see the needle traces in the illustration. It was observed that PI accumulated around the needle traces. An especially high concentration of PI was found around the working needles (the needles used for pulse application), indicating that the permeabilization of the cells was achieved due to the EP treatment. It can be seen clearly in Figure 4.18 that the results of the first 20 mins post-pulsation show a considerable difference between the pulsed and control samples, especially in the dermis and hypodermis layers. In fact, the PI delivery was expected to be higher in those layers since 1) the injection of the PI with MicronJet 600 microinjector was approximately 0.3 to 0.7 mm deep, and 2) the electric field was the strongest at the tip of the needle as shown in Figure 4.17. However, the PI signal intensity increased later in both the control and pulsed samples over time. This raise and the spread of the PI signal could be caused by the free diffusion of PI or the death of the cells. Additionally, the difference between the samples could be explained by their decay over time, which made them

almost identical, indicating the death of the tissue after it was explanted. Although it was kept in the complete culture medium in the incubator (37 °C and 5% CO₂), most of the cells lost their viability within 24 hours post-pulsation. It is also reported in the literature that in the excised skin tissue more than 50% of cells lose their metabolic activity within 24 hours⁶⁵. Nevertheless, it is not clear with the PI test whether the delivery of PI is a consequence of either a reversible or irreversible EP treatment. Thus, the study was continued on a live animal model and with a plasmid DNA delivery that requires the metabolic activity of the cells to express the protein.

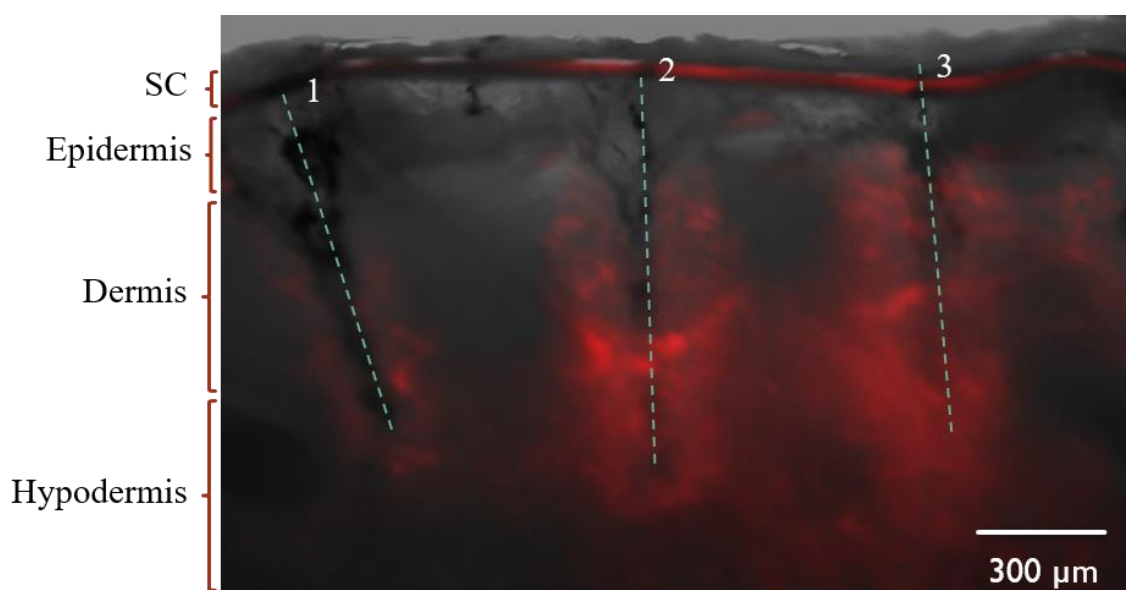


Figure 4.17 An exemplary side view of merged (both in bright field and in TRITC channel) image of the sliced skin section with PI delivery. 15 Vpp, 10 kHz, 1 ms long AC pulse applied between needle 2 and 3. The image was taken 20 mins post-pulsation. The needle length is 1 mm. The blue dash lines show the needle insertion site, the penetration depth is approximately 0.7 mm long. The red color represents the PI delivery.

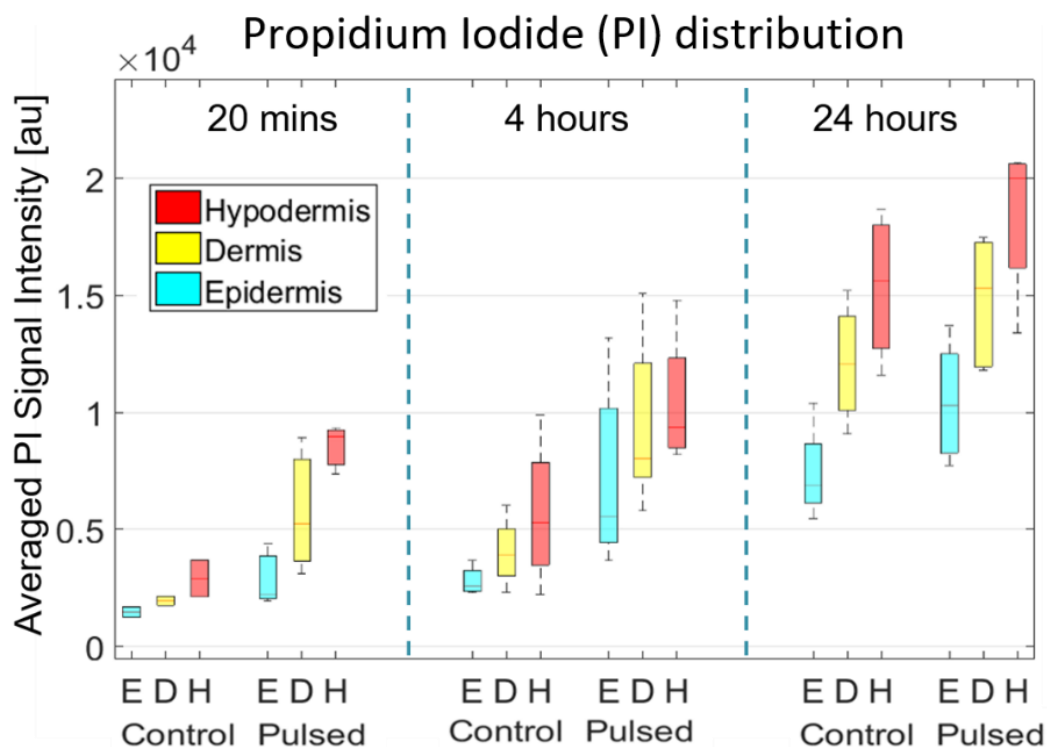


Figure 4.18 The PI delivery distribution in the skin tissue over time is presented with a box plot for each layer of the skin. The side view images of the skin section were analyzed with a custom MATLAB code. The PI signal intensity averaged over the area of each layer. Ignoring the outmost SC layer, the epidermis, dermis, and hypodermis layers were identified with a bright-field image. All samples were injected with 0.1 ml of 40 $\mu\text{g}/\text{ml}$ Propidium Iodide with MicronJet 600 microinjector, approximately 0.3 to 0.7 mm deep into the tissue. In the control samples, needles were inserted but not pulsed, in the pulsed samples 15 Vpp, 10 kHz, 1 ms long AC pulse applied.

4.3.3.2. Impedance results

The impedance of the live rat skin was measured prior and following of the EP pulse to detect electroporation and relate the impedance change with the degree of permeabilization. The potentiostat (Reference 600+) and 1×4 arrayed EP chips were employed, and the impedance was measured at 3 kHz sensing frequency by using the 4-point probe method. Before the impedance measurement, the impedance spectrometry analysis was performed from low to high frequencies, indicating that 1 - 10 kHz sensing frequencies provided distinguishable readings before and after an EP pulsation. As shown in Figure 4.19,

between measurement # 3 and 4, a 1 ms EP pulse was applied (the solid black line) with different field strengths. The percentage of the skin impedance changes before and after the EP pulses were recorded. 1 and 5 V pulses did not show any measurable change, 10 V pulses showed $\sim 1\%$ change in tissue impedance, while the 15 V, 25 V, and 50 V pulses showed a $\sim 4\%$, $\sim 4\%$, and $\sim 8\%$ drop, respectively. These impedance changes can be correlated with the degree of tissue permeabilization. It was expected that increasing the field strength would increase the level of permeabilization. The impedance changes have shown that the tissue starts electro-permeabilizing after 10 V in the present experimental conditions. These results were guided by the following design of experiments and indicated a good consistency. Further impedance measurements after pulsation did not provide any significant signs of recovery or resealing of the cells.

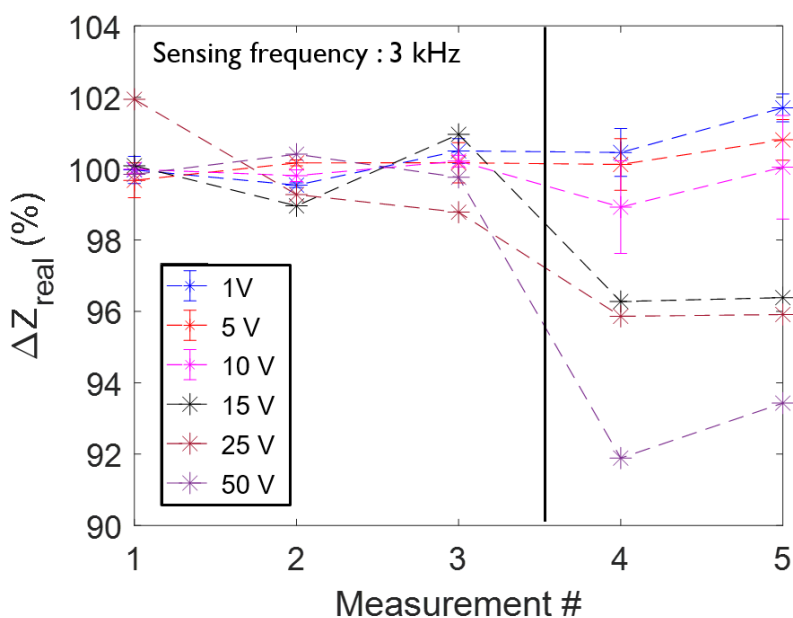


Figure 4.19 The percentage of the skin impedance changes (real part only) are shown. The potentiostat (GAMRY Reference 600+) and 1x4 arrayed EP chips were employed, and impedance was measured at 3 kHz sensing frequency by using a 4-point probe method. The measurement points were randomly selected, and successive measurements were performed for the same point. Between the measurements 3 and 4, a 1 ms EP pulse was applied (the solid black line) with different field strengths.

4.3.3.2. DNA expression results

The following demonstrates the results of the plasmid DNA electrotransfer. In Figure 4.20, the expression of the pEGFP vector is presented. Similar to the prior PI test, 25 μg pEGFP vector in 50 μl PBS solution was injected with MicronJet 600 microinjector, and then 15V, 100 μs long 4 pulses at 1 Hz were applied. 24 hours post-pulsation, the rat was dispatched with CO₂ euthanasia, and the skin was excised and imaged under epifluorescent microscopy. Figure 4.20 gives the top view of the skin sample. The tissue was imaged using FITC, TRITC and DAPI filters to assess autofluorescence, which can be seen due to the nature of the skin and hair follicles^{65,66}. Thereby, it was assured that the green signal in the merged image was due to the GFP expression. As shown in Figure 4.20a, the GFP expression was localized around the needle insertion sites at the corners of the square, corresponding with the needle placement of the EP chip dimensions (1 mm long, 750 μm apart). In Figure 4.21, the GFP expression results were presented with different pulsing conditions. Figure 4.21a shows a control sample, Figure 4.21b shows 15 V, 100 μs long 4 pulses at 1 Hz, and Figure 4.21c shows 30V, 100 μs long 4 pulses at 1 Hz. For the control sample, the needles were inserted but not pulsed. The comparison with the control samples ensures that the GFP expression was achieved due to the EP treatment. Furthermore, the 15 V sample shows distinct expression regions where the needles were located; however, the 30 V sample shows a more diffusive GFP expression.

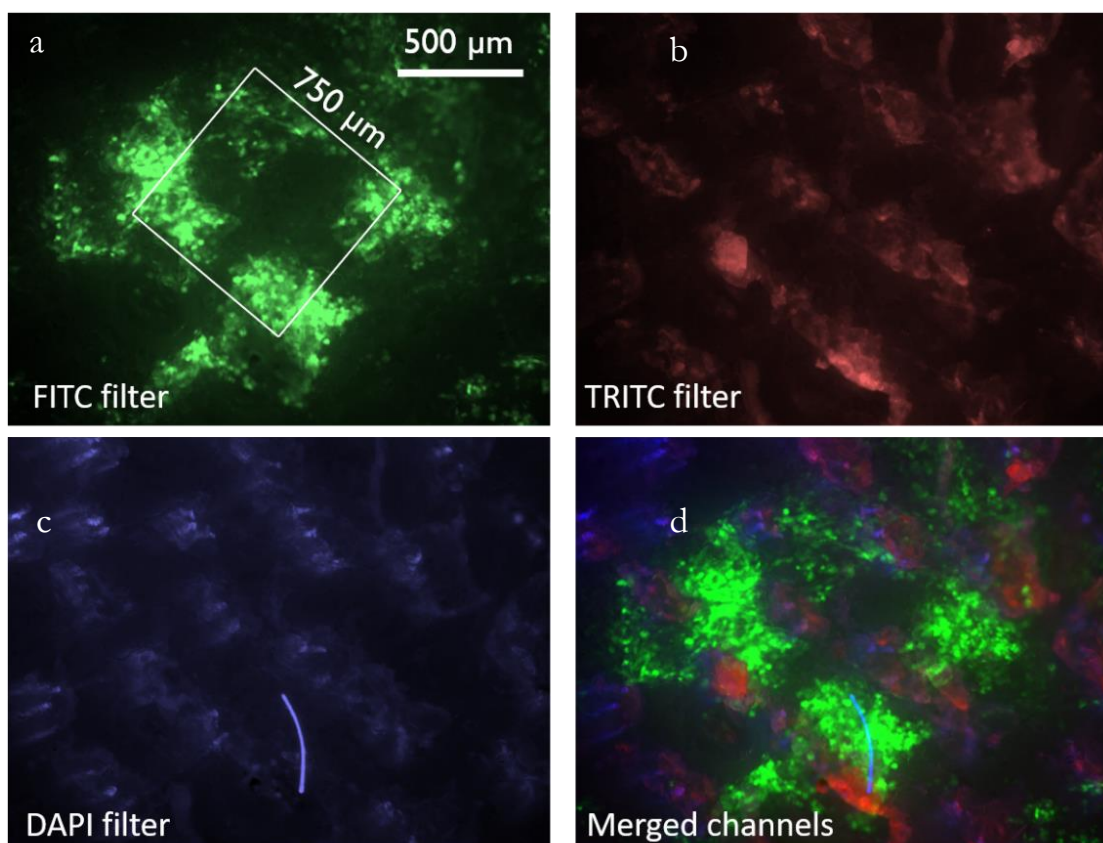


Figure 4.20 GFP expression in the rat skin is presented. 25 μg pEGFP vector in 50 μl PBS solution was injected, 15 V, 100 μs long 4 pulses at 1 Hz were applied. The tissue was imaged using (a) FITC, (b) TRITC and (c) DAPI filters to assess the autofluorescence which can be seen due to the hair follicles. A merged image is presented in (d). The GFP expression is localized around the needle insertion sites at the corners of the square in (a) corresponding to the needle placement consistent with the EP chip dimensions (1 mm long, 750 μm apart).

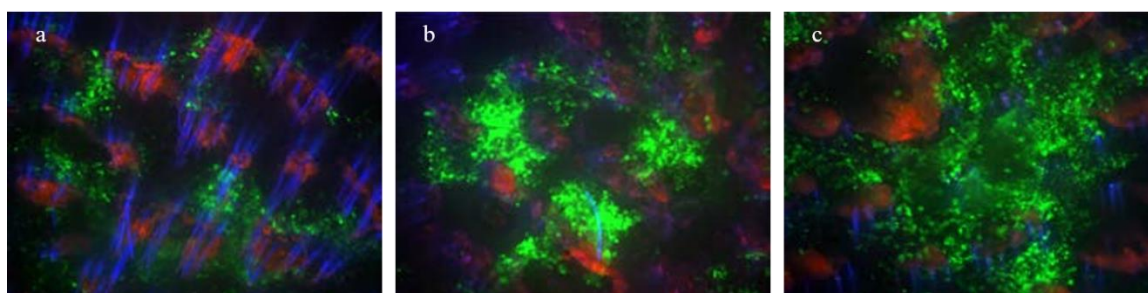


Figure 4.21 GFP expression in the rat skin concerning different pulsing conditions. All images presented merged channels of FITC (green), TRITC (red), and DAPI (blue). 25 μg pEGFP vector in 50 μl PBS solution is injected with MicronJet 600 microinjector, and (a) control sample, (b) 15 V, 100 μs long 4 pulses at 1 Hz, (c) 30 V, 100 μs long 4 pulses at 1 Hz were applied. In the control case, the needles were inserted but not pulsed.

4.4. Discussion

Electroporation is a widely known drug/gene delivery technique, and the recent emergence of immunotherapy and DNA vaccines has spotlighted it thanks to its simplicity and higher efficiency compared to other methods, although there is still a lot of room for improvement^{20,67–69}. First, the stratum corneum (SC) layer of the skin is a hindrance for the electric field penetration to deeper layers of the skin; thus, the electrodes placed on the skin surface require strong (high-voltage) pulses to electropermeabilize the epidermis or dermis layer^{70–72}. A comparison study, conducted by Yan *et al.*, shows that by applying the same pulsing parameters (200 V, 10 ms, 10 pulses) with penetrating versus surface electrode accounts for a tenfold difference in the FD-4 permeation into the deeper layers of the skin⁷³. Additionally, previous studies applied more than 1,000 V pulse with surface electrodes to obtain a significant delivery^{70,71}. A more recent work by Fisher *et al.* applied 200 V, 100 ms long pulses multiple times to achieve a significant GFP expression⁷⁴. However, severe tissue damage is inevitable in case of high-intensity pulse applications. Second, microneedle arrays have shown a significant improvement in drug delivery⁷⁵. However, sole-insertion of microneedles is not efficient for gene transfection. Third, current transdermal skin electroporators have a considerable feature size, for instance, the distance between the electrodes has a more than a millimeter range as listed in Table 4-1. Reaching a sufficient electric field with those designs requires a high voltage application, which ablates the tissue near the electrodes. Lastly, long needle lengths can cause distressing pain for the patient. By addressing these issues, this study aimed to improve the efficiency of the transdermal gene electro-transfection technique by avoiding ablative tissue damage while obtaining a considerable gene transfection. Furthermore, a desired portion of the skin can be electropermeabilized for a targeted vector delivery.

A PCB-based EP chip was designed with penetrating acupuncture needles that were electrically connected to the PCB and independently controllable for various field applications. The 2nd gen. EP chip had a considerably smaller feature size, and the electrodes were spaced 0.75 mm apart, providing on average 0.2 to 0.1 kV/cm electric field strength with an application of 15 to 7.5 V respectively. Thanks to the design, the process quality was improved due to the lower invasiveness achieved by lowering the voltage requirements from 30 – 100 V to 5 – 15 V.

As shown in Figure 4.17, tissue permeabilization was achieved with 15 V_{pp}, 10 kHz, 1 ms long AC pulse. Generally, PI is used for viability assay; therefore, it is not clear with the PI test if the delivery of PI is a consequence of either reversible or irreversible EP treatment. Nonetheless, the PI test helped to understand the electric field distribution during the pulsation. Interpreting the PI distribution within the skin layers in Figure 4.18 provided a valuable insight into the effect of the skin structure. In fact, the PI delivery is expected to be higher in the dermis and hypodermis layers since (1) the injection of the PI with MicronJet 600 microinjector was approximately 0.3 to 0.7 mm deep, and (2) the electric field was the strongest at the tip of the needle as shown in Figure 4.17. Subsequently, the PI signal intensity increased both in control and pulsed samples over time. This raise and spread of the PI signal could be caused by the free diffusion of PI or the death of the cells. Therefore, switching from *ex-vivo* to *in-vivo* studies was necessary.

Another way to characterize the level of electroporabilization was to probe the resistance change within the tissue. The complexity and dielectrics of the tissue introduce capacitive effects e.g. cell membrane acts as a capacitor under applied fields; theoretically, once it reaches enough charge it breaks through, in other words, electroporates. Therefore, the

impedance of the skin was measured to monitor the permeabilization. The impedance spectrometry test was performed to determine the frequency range that clearly distinguished between the permeabilized and non-permeabilized tissue. The results showed that between 1 to 10 kHz sensing frequency range was the most distinguishable and consistent with the previous work⁷⁶. In Figure 4.19, the impedance of the skin is monitored before and after the EP pulsation. These impedance changes could be correlated with the degree of permeabilization of the tissue since the differences were increased expectedly as the pulse strengths were increased. The previous impedance measurement had demonstrated an up to twentyfold change in impedance, which indicates the breakdown of the SC layer⁷⁷. However, this study was able to detect a 3-10 % difference, meaning that the electroporation *in vivo* was achieved. This improvement is promising for future tissue EP studies that will provide better pulsing parameters. The impedance results had led to the following design of experiments.

The protein expression requires multiple stages, e.g. the DNA should be transfected into the cell cytoplasm, then into the cell nucleus without being deteriorated⁷⁸. Once the gene code arrives at the nucleus, it will proceed to the RNA production line, then, the messenger RNA will be translocated into the cytoplasm, and, finally, the ribosomes will synthesize the protein. For all these processes, the viability of the cell is the *sine qua non* of protein expression. Therefore, instead of using an explanted tissue (*ex-vivo*) model, a live rat animal (*in-vivo*) model was considered. Indeed, the rat skin is known to be different than porcine or human skin in many biological and molecular aspects. In particular, the SC and epidermis layers are thinner, and the morphology is different^{79,80}. However, the live rats were chosen due to their wide availability and easy handling compared to larger animal models. Besides, there were numerous studies for skin EP treatment with rodent models^{81,82}.

In this study, comparing with control samples ensures that the GFP expression is achieved by the EP treatment, in Figure 4.20a, the GFP expression was presented. Furthermore, 15V case shows distinct expression regions where the needles were located; however, the 30V sample shows a more diffusive GFP expression. It can be speculated that 30V pulse generated a very strong electric field near the needles; therefore, the cells close the needle were irreversibly electroporated where the field strength was lower apart from the needles' successful reversible electroporation that also occurred. The same manner also applies to the 15V sample. The field near the needles was strong enough to electroporate then reversibly but not strong enough for irreversible electroporation, thus, the GFP expression occurred near the needles, and further away from then the cells did not permeabilize. This study has shown that choosing electrical parameters correctly is a critical factor for protein expression.

4.5. Conclusion

This study aimed to develop an electroporation device using the PCB technology to improve targeted transdermal gene transfection. Two generations of EP chips were designed, prototyped, and tested both *ex-vivo* and *in-vivo* with porcine and murine models, respectively. The feasibility and mass production capability of EP chips was demonstrated by upgrading and revising the design and assembly approach where the cost of a single chip might be less than \$1.00. By decreasing the spacing between the electrodes to submillimeter, the voltage requirements were reduced from the 100 V to 10 V range. Additionally, targeted DNA delivery was achieved by adjusting the pulsing parameters. This demonstration assures the efficacy of the EP approach. The eventual objective of this work is to fulfill the promising capability of EP in practical clinical applications to benefit human health.

4.6. References

1. Neumann, E., Schaefer-Ridder, M., Wang, Y. & Hofschneider, P. H. Gene transfer into mouse lyoma cells by electroporation in high electric fields. *EMBO J* 1, 841–845 (1982).
2. McNeil, P. L., Murphy, R. F., Lanni, F. & Taylor, D. L. A Method for Incorporating Macromolecules into Adherent Cells. *The Journal of Cell Biology* 98, 1556–1564 (1984).
3. Buono, R. J. & Linser, P. J. Transient expression of RSV-CAT in transgenic zebrafish made by electroporation. *Mol Mar Biol Biotechnol* 1, 271–275 (1992).
4. Prausnitz, M. R., Bose, V. G., Langer, R. & Weaver, J. C. Electroporation of mammalian skin: a mechanism to enhance transdermal drug delivery. *PNAS* 90, 10504–10508 (1993).
5. Zhang, L., Li, L., Hoffmann, G. A. & Hoffman, R. M. Depth-Targeted Efficient Gene Delivery and Expression in the Skin by Pulsed Electric Fields: An Approach to Gene Therapy of Skin Aging and Other Diseases. *Biochemical and Biophysical Research Communications* 220, 633–636 (1996).
6. Vanbever, R. Transdermal delivery of fentanyl: rapid onset of analgesia using skin electroporation. *Journal of Controlled Release* 50, 225–235 (1998).
7. Harrison, R. L., Byrne, B. J. & Tung, L. Electroporation-mediated gene transfer in cardiac tissue. *FEBS Letters* 435, 1–5 (1998).
8. Müller, F., Lele, Z., Váradi, L., Menczel, L. & Orbán, L. Efficient transient expression system based on square pulse electroporation and in vivo luciferase assay of fertilized fish eggs. *FEBS Letters* 324, 27–32 (1993).
9. Momose, T. et al. Efficient targeting of gene expression in chick embryos by microelectroporation. *Development, Growth & Differentiation* 41, 335–344 (1999).
10. Rubinsky, B. Irreversible Electroporation in Medicine. *Technol Cancer Res Treat* 6, 255–259 (2007).
11. Scheffer, H. J. et al. Irreversible Electroporation for Nonthermal Tumor Ablation in the Clinical Setting: A Systematic Review of Safety and Efficacy. *Journal of Vascular and Interventional Radiology* 25, 997–1011 (2014).
12. Jiang, C., Davalos, R. V. & Bischof, J. C. A Review of Basic to Clinical Studies of Irreversible Electroporation Therapy. *IEEE Transactions on Biomedical Engineering* 62, 4–20 (2015).
13. Cheung, W. et al. Irreversible Electroporation for Unresectable Hepatocellular Carcinoma: Initial Experience and Review of Safety and Outcomes. *Technol Cancer Res Treat* 12, 233–241 (2013).
14. Heller, L. C., Ugen, K. & Heller, R. Electroporation for targeted gene transfer. *Expert Opinion on Drug Delivery* 2, 255–268 (2005).
15. Wolff, J. A. et al. Direct gene transfer into mouse muscle in vivo. *Science* 247, 1465–1468 (1990).
16. Tendeloo, V. F. I. V. et al. Highly efficient gene delivery by mRNA electroporation in human hematopoietic cells: superiority to lipofection and passive pulsing of mRNA and to electroporation of plasmid cDNA for tumor antigen loading of dendritic cells. *Blood* 98, 49–56 (2001).
17. Gehl, J. Electroporation: theory and methods, perspectives for drug delivery, gene therapy and research. *Acta Physiologica Scandinavica* 177, 437–447 (2003).
18. Swartz, M., Eberhart, J., Mastick, G. S. & Krull, C. E. Sparking New Frontiers: Using in Vivo Electroporation for Genetic Manipulations. *Developmental Biology* 233, 13–21 (2001).
19. Dev, S. B., Rabussay, D. P., Widera, G. & Hofmann, G. A. Medical applications of electroporation. *IEEE Transactions on Plasma Science* 28, 206–223 (2000).
20. Bernal, C. et al. A review of pulse generation topologies for clinical electroporation. in *IECON 2015 - 41st Annual Conference of the IEEE Industrial Electronics Society* 000625–000630 (2015). doi:10.1109/IECON.2015.7392169
21. Geng, T. et al. Flow-through electroporation based on constant voltage for large-volume transfection of cells. *Journal of Controlled Release* 144, 91–100 (2010).
22. Butkus, P. Development of planar electrodes for real-time electroporation. *Mokslas – Lietuvos ateitis: Elektronika ir elektros inžinerija* - 2018 1–4 (2018).
23. Mohr, J. C., dePablo, J. J. & Palecek, S. P. Electroporation of Human Embryonic Stem Cells: Small and Macromolecule Loading and DNA Transfection. *Biotechnology Progress* 22, 825–834 (2006).
24. Dean, D. A., Machado-Aranda, D., Blair-Parks, K., Yeldandi, A. V. & Young, J. L. Electroporation as a method for high-level nonviral gene transfer to the lung. *Gene Therapy* 10, 1608 (2003).
25. Molnar, M. J. et al. Factors Influencing the Efficacy, Longevity, and Safety of Electroporation-Assisted Plasmid-Based Gene Transfer into Mouse Muscles. *Molecular Therapy* 10, 447–455 (2004).
26. Sadik, M. M. et al. Scaling relationship and optimization of double-pulse electroporation. *Biophys J* 106, 801–812 (2014).

27. Yarmush, M. L., Golberg, A., Serša, G., Kotnik, T. & Miklavčič, D. Electroporation-Based Technologies for Medicine: Principles, Applications, and Challenges. *Annu. Rev. Biomed. Eng.* 16, 295–320 (2014).
28. Tang, J. et al. In vivo electroporation of a codon-optimized BERopt DNA vaccine protects mice from pathogenic *Mycobacterium tuberculosis* aerosol challenge. *Tuberculosis* 113, 65–75 (2018).
29. Hegazy-Hassan, W. et al. TcVac1 vaccine delivery by intradermal electroporation enhances vaccine induced immune protection against *Trypanosoma cruzi* infection in mice. *Vaccine* 37, 248–257 (2019).
30. Wang, R. et al. Maternal immunization with a DNA vaccine candidate elicits specific passive protection against post-natal Zika virus infection in immunocompetent BALB/c mice. *Vaccine* 36, 3522–3532 (2018).
31. Hasan, Y. et al. A phase 1/2A trial of synthetic DNA vaccine immunotherapy targeting HPV-16 and -18 after chemoradiation for cervical cancer. *JCO* 36, 5525–5525 (2018).
32. Myllymäki, H., Niskanen, M., Oksanen, K. & Rämetsä, M. Immunization of Adult Zebrafish for the Preclinical Screening of DNA-based Vaccines. *JoVE (Journal of Visualized Experiments)* e58453 (2018). doi:10.3791/58453
33. Sardesai, N. Y. & Weiner, D. B. Electroporation delivery of DNA vaccines: prospects for success. *Current Opinion in Immunology* 23, 421–429 (2011).
34. Bodles-Brakhop, A. M., Heller, R. & Draghia-Akli, R. Electroporation for the Delivery of DNA-based Vaccines and Immunotherapeutics: Current Clinical Developments. *Molecular Therapy* 17, 585–592 (2009).
35. Reprogramming human T cell function and specificity with non-viral genome targeting | *Nature*. Available at: <https://www.nature.com/articles/s41586-018-0326-5>. (Accessed: 29th January 2019)
36. Tanihara, F. et al. Generation of PDX-1 mutant porcine blastocysts by introducing CRISPR/Cas9-system into porcine zygotes via electroporation. *Animal Science Journal* 90, 55–61 (2019).
37. Qin, W. & Wang, H. Delivery of CRISPR-Cas9 into Mouse Zygotes by Electroporation. in *Microinjection: Methods and Protocols* (eds. Liu, C. & Du, Y.) 179–190 (Springer New York, 2019). doi:10.1007/978-1-4939-8831-0_10
38. Latella, M. C. et al. In vivo Editing of the Human Mutant Rhodopsin Gene by Electroporation of Plasmid-based CRISPR/Cas9 in the Mouse Retina. *Molecular Therapy - Nucleic Acids* 5, e389 (2016).
39. Trainer, A. H. & Alexander, M. Y. Gene Delivery to the Epidermis. *Hum Mol Genet* 6, 1761–1767 (1997).
40. Chen, X. Current and future technological advances in transdermal gene delivery. *Advanced Drug Delivery Reviews* 127, 85–105 (2018).
41. Haniffa, M., Gunawan, M. & Jardine, L. Human skin dendritic cells in health and disease. *J Dermatol Sci* 77, 85–92 (2015).
42. McKenna, N. Tackling Transfection Tasks. *Genetic Engineering & Biotechnology News* 33, 1, 22, 24 (2012).
43. Lambrecht, L. et al. Clinical potential of electroporation for gene therapy and DNA vaccine delivery. *Expert Opinion on Drug Delivery* 13, 295–310 (2016).
44. Diehl, M. C. et al. Tolerability of intramuscular and intradermal delivery by CELLECTRA® adaptive constant current electroporation device in healthy volunteers. *Hum Vaccin Immunother* 9, 2246–2252 (2013).
45. Amante, D. H. et al. Skin Transfection Patterns and Expression Kinetics of Electroporation-Enhanced Plasmid Delivery Using the CELLECTRA-3P, a Portable Next-Generation Dermal Electroporation Device. *Human Gene Therapy Methods* 26, 134–146 (2015).
46. Hooper, J. W., Golden, J. W., Ferro, A. M. & King, A. D. Smallpox DNA vaccine delivered by novel skin electroporation device protects mice against intranasal poxvirus challenge. *Vaccine* 25, 1814–1823 (2007).
47. El-Kamary, S. S. et al. Safety and Tolerability of the Easy Vax™ Clinical Epidermal Electroporation System in Healthy Adults. *Mol Ther* 20, 214–220 (2012).
48. Hofmann, G. A., Dev, S. B., Dimmer, S. & Nanda, G. S. Electroporation therapy: a new approach for the treatment of head and neck cancer. *IEEE Transactions on Biomedical Engineering* 46, 752–759 (1999).
49. Rabussay, D. et al. Enhancement of therapeutic drug and DNA delivery into cells by electroporation. *J. Phys. D: Appl. Phys.* 36, 348–363 (2003).
50. Wallace, M. et al. Tolerability of Two Sequential Electroporation Treatments Using MedPulser DNA Delivery System (DDS) in Healthy Adults. *Molecular Therapy* 17, 922–928 (2009).
51. Best, S. R. et al. Administration of HPV DNA vaccine via electroporation elicits the strongest CD8+ T cell immune responses compared to intramuscular injection and intradermal gene gun delivery. *Vaccine* 27, 5450–5459 (2009).
52. Kang, T. H. et al. Enhancement of protein vaccine potency by in vivo electroporation mediated intramuscular injection. *Vaccine* 29, 1082–1089 (2011).
53. van Drunen Littel-van den Hurk, S. et al. Electroporation-based DNA transfer enhances gene expression and immune responses to DNA vaccines in cattle. *Vaccine* 26, 5503–5509 (2008).

54. Canton, D. A. et al. Melanoma treatment with intratumoral electroporation of tavokinogene telseplasmid (pIL-12, tavokinogene telseplasmid). *Immunotherapy* 9, 1309–1321 (2017).
55. Miklavčič, D. et al. Electrochemotherapy: technological advancements for efficient electroporation-based treatment of internal tumors. *Med Biol Eng Comput* 50, 1213–1225 (2012).
56. Cadossi, R., Ronchetti, M. & Cadossi, M. Locally enhanced chemotherapy by electroporation: clinical experiences and perspective of use of electrochemotherapy. *Future Oncology* 10, 877–890 (2014).
57. Li, J., Tan, W., Yu, M. & Lin, H. The effect of extracellular conductivity on electroporation-mediated molecular delivery. *Biochimica et Biophysica Acta (BBA) - Biomembranes* 1828, 461–470 (2013).
58. Demiryurek, Y. et al. Transport, resealing, and re-poration dynamics of two-pulse electroporation-mediated molecular delivery. *Biochimica et Biophysica Acta (BBA) - Biomembranes* 1848, 1706–1714 (2015).
59. Yu, M. & Lin, H. Quantification of propidium iodide delivery with millisecond electric pulses: A model study. *arXiv:1401.6954 [physics]* (2014).
60. Yu, M., Tan, W. & Lin, H. A stochastic model for DNA translocation through an electropore. *Biochimica et Biophysica Acta (BBA) - Biomembranes* 1818, 2494–2501 (2012).
61. Yu, M. & Lin, H. Modeling Transport Across the Electroporated Membrane. in *Handbook of Electroporation* (ed. Miklavcic, D.) 1–22 (Springer International Publishing, 2016). doi:10.1007/978-3-319-26779-1_6-1
62. Li, J. & Lin, H. Numerical simulation of molecular uptake via electroporation. *Bioelectrochemistry* 82, 10–21 (2011).
63. Volumetric Modifications of X-Irradiated Keratinocytes - KLEIN-SZANTO - 1977 - *Journal of Cutaneous Pathology* - Wiley Online Library. Available at: <https://onlinelibrary.wiley.com/doi/abs/10.1111/j.1600-0560.1977.tb00884.x>. (Accessed: 20th August 2019)
64. Validation of a morphometric method for evaluating fibroblast numbers in normal and pathologic tissues - Miller - 2003 - *Experimental Dermatology* - Wiley Online Library. Available at: <https://onlinelibrary.wiley.com/doi/full/10.1034/j.1600-0625.2003.00023.x>. (Accessed: 20th August 2019)
65. Gothelf, A. & Gehl, J. What you always needed to know about electroporation based DNA vaccines. *Hum Vaccin Immunother* 8, 1694–1702 (2012).
66. Tam, J. M., Upadhyay, R., Pittet, M. J., Weissleder, R. & Mahmood, U. Improved in Vivo Whole-Animal Detection Limits of Green Fluorescent Protein-Expressing Tumor Lines by Spectral Fluorescence Imaging. *Mol Imaging* 6, 7290.2007.00023 (2007).
67. Chen, X. Current and future technological advances in transdermal gene delivery. *Advanced Drug Delivery Reviews* 127, 85–105 (2018).
68. Shi, J. et al. A Review on Electroporation-Based Intracellular Delivery. *Molecules* 23, (2018).
69. Ghosh, D., Saluja, N. & Singh, T. G. A CRITICAL ANALYSIS OF ELECTROPORATION IN MEDICAL TECHNOLOGY. *INTERNATIONAL JOURNAL OF PHARMACEUTICAL SCIENCES AND RESEARCH* 10, 23–28 (2019).
70. Roos, A.-K. et al. Skin Electroporation: Effects on Transgene Expression, DNA Persistence and Local Tissue Environment. *PLoS ONE* 4, e7226 (2009).
71. Dujardin, N., Van Der Smissen, P. & Pr  at, V. Topical Gene Transfer into Rat Skin Using Electroporation. *Pharm Res* 18, 61–66 (2001).
72. Prausnitz, M. R. et al. Methods for in Vivo Tissue Electroporation Using Surface Electrodes. *Drug Delivery* 1, 125–131 (1993).
73. Yan, K., Todo, H. & Sugibayashi, K. Transdermal drug delivery by in-skin electroporation using a microneedle array. *International Journal of Pharmaceutics* 397, 77–83 (2010).
74. Fisher, P. D. et al. Adipose tissue: a new target for electroporation-enhanced DNA vaccines. *Gene Ther* 24, 757–767 (2017).
75. Larra  eta, E., Lutton, R. E. M., Woolfson, A. D. & Donnelly, R. F. Microneedle arrays as transdermal and intradermal drug delivery systems: Materials science, manufacture and commercial development. *Materials Science and Engineering: R: Reports* 104, 1–32 (2016).
76. Zahn, J. D., Hsieh, Y.-C. & Yang, M. Components of an Integrated Microfluidic Device for Continuous Glucose Monitoring with Responsive Insulin Delivery. *Diabetes Technology & Therapeutics* 7, 536–545 (2005).
77. Impedance spectroscopy as an indicator for successful in vivo electric field mediated gene... - Abstract - Europe PMC. Available at: <https://europepmc.org/abstract/med/28237705>. (Accessed: 20th August 2019)
78. Young, J. L. & Dean, D. A. Electroporation-Mediated Gene Delivery. *Adv Genet* 89, 49–88 (2015).
79. Topical Drug Bioavailability, Bioequivalence, and Penetration. (Springer-Verlag, 2014).

80. Capt, A., Luzy, A. P., Esdaile, D. & Blanck, O. Comparison of the human skin grafted onto nude mouse model with in vivo and in vitro models in the prediction of percutaneous penetration of three lipophilic pesticides. *Regul Toxicol Pharmacol* 47, 274–287 (2007).
81. McCoy, J. R. et al. A multi-head intradermal electroporation device allows for tailored and increased dose DNA vaccine delivery to the skin. *Human Vaccines & Immunotherapeutics* 11, 746–754 (2015).
82. Dujardin, N., Van Der Smissen, P. & Pr  at, V. Topical gene transfer into rat skin using electroporation. *Pharm. Res.* 18, 61–66 (2001).

Chapter 5

Conclusion

The main theme of this dissertation has been to investigate the effects of electric field on biological cells and tissue. A large number of experiments were performed to better understand and quantify the results of electric field application to the cells and tissue, for their mechanical properties and biological activities for drugs/genes transport. This study is composed of three parts where the electric field parameters varied in a wide spectrum. Figure 1.2 summarized the pulsing parameters with respect to field frequency: (1) a high-frequency region ($\omega \geq 10^6$ Hz) where the V_m is nearly zero, (2) the “sweet spot” where the V_m is higher than 0.5 V and $\omega > 10^3$ Hz, and (3) the electroporation region where V_m is higher than 0.5 V and approaching DC field behavior.

Mechanical properties of biological cells are closely linked with their physiological and pathological states. In the first part of this study, electrodeformation-relaxation is utilized to bring forth new insights into the mechanical properties of biological cells. The experimental platform was established using an indium-tin-oxide (ITO) coated glass slide and parallel electrodes were lithographically defined by etching ITO. Various types of cells in suspension, including MCF-10A, MCF-7, MDA-MB-231, and GBM were exposed to high frequency and amplitude electric pulses. The pulsing protocol ensures the occurrence of deformation and the absence of electroporation. Our procedure was a clear improvement on current electrodeformation methods that have pulsing durations ranging from milliseconds to minutes. Two distinctive regimes were identified by data analysis. If cells were deformed for shorter than a threshold of approximately tens of milliseconds, the relaxation timescales are independent of the pulse duration, indicating invariant mechanical properties. When deformed

for longer than the threshold, the relaxation time scales linearly with the pulse duration, which is typically seen in soft glassy materials. The regimes are found to be present across the various cell types examined, providing insights into understanding the cellular response to mechanical cues. Quantification of the “naïve” cell mechanical properties is only possible in the first one. The technique promises ease of implementation and high-throughput for large-scale cell mechanical analysis.

In Part 2, we conducted a series of two-pulse electroporation experiments at the cellular level, focusing on the delivery efficiency of two different-sized molecules using different pulsing parameters. Using an AC first pulse to porate the membrane, and a DC second pulse for transport, we were able to probe resealing dynamics over timescales ranging from milliseconds to minutes. The first set of analyses highlighted the impact of a clear separation of permeabilization and delivery. Then, we found for these cells and pulsing parameters, electroporation-mediated delivery scaled with the logarithm of the delay time regardless of the molecule size, and 50% of resealing happened in the first 100 ms after pulsation. However, complete resealing took hundreds of seconds. This result may unify the inconsistent membrane resealing times reported in the literature for different experiments. A more detailed study on this finding can be considered in a future-work by delivering more different-sized target molecules and using different types of cells. In addition, this behavior can be validated with another analytical method such as flow-cytometry. Furthermore, clear evidence for the fast-shrinking after the pulsation could not be detected with our current experiment design due to temporal resolution limitation. A new experimental procedure needs to be designed to probe the transport mechanisms in shorter time scales.

In Part 3, at the tissue level, we engineered a miniaturized device to achieve the goal of transdermal delivery with high efficiency and viability. A printed circuit board (PCB) based, minimally-invasive transdermal gene delivery device was designed and prototyped. Our electrical characterization studies well-agreed with computational predictions that provided strong confidence to proceed to animal studies. Additionally, the experiment setup was reinforced by a high-sensitive potentiostat to probe impedance of the skin before and after EP. Previous studies demonstrated up to 20 folds change in impedance which indicated the breakdown of the SC layer. However, this study was able to detect 3-10 % difference which indicates the electroporation *in vivo*. The feasibility and mass production capability of electroporation chips have been demonstrated by upgrading and revising the design and assembly approach where the cost of a single chip may be less than \$1.00. By decreasing the spacing between electrodes to submillimeter, the voltage requirements have been reduced from the 100 V to the 10 V range. These micro-electrode-based devices were extensively tested on animals (rats) to demonstrate efficacies on gene expression. We have obtained satisfactory results demonstrating that transdermal EP can be used for gene delivery. Inevitably, there would be some discrepancies due to murine animal model. However, the eventual objective of this work is to fulfill the promising capability of EP in realistic clinical applications to benefit human health.